

Infrared Spectroscopy of Star Formation in Galactic and Extragalactic Regions

Grant NAG5-10659

Annual Performance Report No. 4

For the period 1 March 2004 through 28 February 2005

Principal Investigator:

Dr. Howard A. Smith

December 2004

Prepared for
National Aeronautics and Space Administration
Washington D.C.

Smithsonian Institution
Astrophysical Observatory
Cambridge, Massachusetts 02138-1596

The Smithsonian Astrophysical Observatory
is a member of the
Harvard-Smithsonian Center for Astrophysics

The NASA Technical Officer for this grant is Dr. Hashima Hasan, NASA Headquarters, 300 E Street
SW, Code SZ, Washington DC 20546-0001

I.	PROGRAM OBJECTIVES	1
II.	PROGRESS REPORT	1
A.	ISO DATA ANALYSIS AND MODELING.....	1
B.	OTHER SCIENCE RESULTS.....	2
C.	ADVISING STUDENTS AND POSTDOCS	2
D.	CONTRIBUTIONS TO CONFERENCES AND PROCEEDINGS.....	2
E.	E&PO ACTIVITIES	2
III.	FINAL PROGRAM PLANS	2
APPENDIX A.	PUBLICATIONS LIST	
APPENDIX B.	SPITZER OBSERVATIONS	
APPENDIX C.	PAPERS	

I. Program Objectives

In this program we proposed to perform a series of spectroscopic studies, including data analysis and modeling, of star formation regions using an ensemble of archival space-based data from the Infrared Space Observatory's Long Wavelength Spectrometer and Short Wavelength Spectrometer, from the Spitzer IRS results, and to take advantage of other spectroscopic databases. Our emphasis has been on star formation in external, bright IR galaxies, but other areas of research have included young, low or high mass pre-main sequence stars in star formation regions, and the galactic center. The OH lines in the far infrared were proposed as one key focus of this inquiry, because the Principal Investigator (H. Smith) had a full set of OH IR lines from ISO observations. It was planned that during the originally proposed timeframe of the proposal other data (including Spitzer IRS data) would become available, and we proposed using these and other such spectroscopic data sets.

The program has the following goals:

- 1) Refine the data analysis of ISO observations to obtain deeper and better SNR results on selected sources.
- 2) Model the atomic and molecular line shapes, in particular the OH lines, using revised montecarlo techniques developed by the Submillimeter Wave Astronomy Satellite (SWAS) team at the Center for Astrophysics.
- 3) Use newly acquired space-based Spitzer spectroscopic data, and contribute to these observing programs as appropriate.
- 4) Attend scientific meetings and workshops.

The program since its inception has been extremely successful: We presented or submitted over two dozen articles, sponsored a workshop, and participated in scientific conferences. The molecular line montecarlo code has undergone important revisions for infrared lines and has made significant predictions. We have participated in nineteen publications that have already appeared (not counting a few works in preparation) and made useful contributions to Spitzer Space Telescope science observations. E&PO programs have been active. Last year's funding arrived 11 months late, seriously delaying some work. Also, we have not yet been able to get calibrated Spitzer spectrometer (IRS) data for key long wavelength observations, while the montecarlo code has only just this month passed muster by a referee on a paper. We will therefore request a no-cost extension to complete the programs.

II. Progress Report

A. ISO Data Analysis and Modeling

Last year we submitted and had accepted a paper entitled "The Far-Infrared Emission Line and Continuum Spectrum of the Seyfert Galaxy NGC 1068," by Spinoglio, L., Malkan, M., Smith, H.A., González-Alfonso, E., and Fischer, J. This analysis was based on the SWAS montecarlo code modeling of the OH lines in galaxies observed by ISO (see Figures 1 and 2 from the preprint attached). Since that meeting last spring considerable effort has been put into improving the montecarlo code. A group of European astronomers, including Prof. Eduardo González-Alfonso, had been performing montecarlo modeling of other molecules seen in ISO galaxies. We used portions of this grant to bring Prof. González-Alfonso to Cambridge for an intensive working visit.

A second major paper on the ISO IR spectroscopy of galaxies, "The Far Infrared Spectrum of Arp 220," González-Alfonso, E., Smith, H., Fischer, J., and Cernicharo, J., is in press (ApJ).

B. Other Science Results

SPITZER: Spitzer science development was the major component of this past year's research. This program supported the development of five "Early Release Objects" for Spitzer observations on which Dr. Smith was Principal Investigator or Co-Investigator, and another five proposals for GO time. The early release program is designed to rapidly present to the public and the scientific community some exciting results from Spitzer in the first months of its operation. The Spitzer instrument and science teams submitted proposals for ERO objects, and a competitive selection process narrowed these down to a small group with exciting science and realistic observational parameters. This grant supported Dr. Smith's participation in the ERO process, including developing science goals, identifying key objects for observation, and developing the detailed AOR (observing formulae) to be used by the instruments for mapping, integrating, etc.). During this year Dr. Smith worked on writing up and publishing these early results.

The attached bibliography includes six of Dr. Smith's articles that appeared in the Spitzer Space Telescope special edition of ApJ Supplement.

During this past year Dr. Smith also led or helped to develop proposals for ten Spitzer GO Programs, and three others. Appendix B lists the programs involved.

C. Advising Students and Postdocs

During this year we supervised the visit of Dr. Eduardo González-Alfonso, who worked on the galaxy modeling (reprints attached). We also advised numerous scientists on their proposals for Spitzer GO time (in addition to those on which Dr. Smith is a Co-I).

D. Contributions to Conferences and Proceedings

During this year Dr. Smith gave talks on work from this program at four conferences and meetings:

- AAS General Meeting, January 2004
- Cores, Disks, Jets and Outflows Meeting, July 2004
- CfA Star-Formation Meeting, September 2004
- The Dusty and Molecular Universe, October 2004

E. E&PO Activities

During this period the PI gave several talks to elementary school groups as well as to a summer camp.

III. Final Program Plans

During the final year of this program we intend to bring to closure all the projects discussed to date, including all those which have been extended due to the delay in Spitzer spectrometer (IRS) calibrations, completion of the monte-carlo code work and associated reviews, and residual work delayed due to last year's NASA funding arriving 11 months late. Should the IRS long-high calibration remain problematic we will nevertheless complete the work as best we can and use that data in another effort. Although we anticipate a relatively expeditious completion process we are requesting a conventional one-year extension. No further extensions will be needed.

- 1) Reduction of the ISO galaxy data set on Mrk 231, NGC 253, and Arp 299 using the González algorithms;

- 2) Modeling the OH lines with the newly corrected and improved montecarlo code;
- 3) Tightening the arguments made in our earlier article -- that there are three types of active/IRB galaxies as typified by the kinds of molecular clouds that dominate their FIR emission: large diffuse clouds as in normal IRBs; smaller, more dense clouds as in Arp 220 and other mixed AGN; and very dense small cloudlets as seen in the Seyfert galaxy NGC 1068;
- 4) Spitzer activities: Publish new research on massive star formation in the DR21 complex measured by Spitzer, and on time variability of galactic nuclei as seen by Spitzer. We will continue to be active in E&PO and GO projects, including submitting an aggressive IRAC/Spitzer E&PO proposal.

IV. Reportable Patents/New Technology

There have been no reportable patents/new technology made under this grant.

Appendix A. Publications List

- "The Far Infrared Lines of OH as Molecular Cloud Diagnostics," Smith, H. A., Ashby, Matt, Fischer, Jackie, González, Eduardo, Spinoglio, Luigi, Dudley, Chris, *The Astrochemistry of External Galaxies*, 25th meeting of the IAU, Joint Discussion 21, 23 July 2003, Sydney, Australia.
- "First Extragalactic Science from IRAC, The Infrared Array Camera on SST," Willner, S., ... Smith, H., *et al.*, BAAS, 2004.
- "First Galactic Images from IRAC, SST's Infrared Array Camera," Megeath, T., ... Smith, H.A., *et al.*, BAAS, 2004.
- "DR21: A Major Star Formation Site Revealed by *Spitzer*," A.P. Marston, W.T. Reach, A. Noriega-Crespo, J. Rho, H.A. Smith, G. Melnick, G. Fazio, G. Rieke, S. Carey, L. Rebull, J. Muzerolle, E. Egami, D.M. Watson, J.L. Pipher, W.B. Latter, K. Stapelfeldt, *ApJS* **154**, 333, 2004.
- "The Off-Nuclear Starbursts in NGC 4038/4039 (The Antennae Galaxies)," Z. Wang, G.G. Fazio, M.L.N. Ashby, J.-S. Huang, M.A. Pahre, H.A. Smith, S.P. Willner, W.J. Forrest, J.L. Pipher and J.A. Surace, *ApJS* **154**, 193, 2004.
- "IRAC Observations of M81," S.P. Willner, M.L.N. Ashby, P. Barmby, G.G. Fazio, M. Pahre, H.A. Smith, Robert C. Kennicutt, Jr., Daniel A. Dale, B.T. Draine, Michael W. Regan, S. Malhotra, Michele D. Thornley, P.N. Appleton, D. Frayer, G. Helou, L. Storrie-Lombardi, S. Stolovy, *ApJS* **154**, 222, 2004.
- "The Anatomy of Star Formation in NGC 300," G. Helou, H. Roussel, P. Appleton, D. Frayer, S. Stolovy, L. Storrie-Lombardi, R. Hurt, P. Lowrance, D. Makovoz, F. Masci, J. Surace, K. D. Gordon, A. Alonso-Herrero, C. Engelbracht, K. Misselt, G. Rieke, M. Rieke, S. Willner, M. Pahre, M. Ashby, G.G. Fazio, H.A. Smith, *ApJS* **154**, 253, 2004.
- "The IRAC Shallow Survey," P.R. Eisenhardt, D. Stern, M. Brodwin, G. Fazio, G. Rieke, M. Rieke, M. Werner, E. Wright, L. Allen, R. Arendt, M. Ashby, P. Barmby, W. Forrest, J. Hora, J. Huang, J. Huchra, M. Pahre, J. Pipher, W. Reach, H.A. Smith, J. Stauffer, Z. Wang, S. Willner, M.J.I. Brown, A. Dey, B.T. Jannuzi, and G.P. Tiede, *ApJS* **154**, 48, 2004.
- "The Infrared Array Camera (IRAC) for the Spitzer Space Telescope," G.G. Fazio, J.L. Hora, L.E. Allen, M.L.N. Ashby, P. Barmby, L.K. Deutsch, J.-S. Huang, S. Kleiner, M. Marengo, S.T. Megeath, G.J. Melnick, M.A. Pahre, B.M. Patten, J. Polizotti, H.A. Smith, R.S. Taylor, Z. Wang, S.P. Willner, W.F. Hoffmann, J.L. Pipher, W.J. Forrest, C.W. McMurty, C.R. McCreight, M.E. McKelvey, R.E. McMurray, D.G. Koch, S.H. Moseley, R.G. Arendt, J.E. Mentzell, C. Trout-Marx, P. Losch, P. Mayman, W. Eichhorn, D. Krebs, M. Jhabvala, D.Y. Gezari, D. Fixen, J. Flores, K. Shakoorzadeh, R. Jungo, C. Hakun, L. Workman, G. Karpati, R. Kichak, R. Whitley, S. Mann, E.V. Tollestrup, P. Eisenhardt, D. Stern, V. Gorjian, B. Bhattacharya, S. Carey, B.O. Nelson, W. J. Glaccum, M. Lacy, P.J. Lowrance, S. Laine, W.T. Reach, J.R. Stauffer, J.A. Surace, G. Wilson, E.L. Wright, A. Hoffman, G. Domingo, and M. Cohen, *ApJS* **154**, 10, 2004.
- "DR21-IRS1: Spitzer-IRAC Four-Color Images of the Origin of the Massive Outflow and its Cluster of Embedded Stars," Smith, H.A., Allen, L.E., Fazio, G., Melnick, G., Marston, A.P., Gutermuth, R., Pipher, J., Watson, D., Carey, S., Noriega-Crespo, A., BAAS, 204, 6110, 2004.

- "The Far-IR Spectrum of Arp 220," González-Alfonso, E., Smith, H. A., Fischer, J., Cernicharo, J., BAAS, **204**, 4020, 2004.
- "Spitzer Space Telescope Observations of the Antennae Galaxies," Wang, Z., Fazio, G.G., Ashby, M. L. N., Huang, J.-S., Pahre, M.A., Smith, H.A., Willner, S.P., Forrest, W.J., Pipher, J.L., Surace, J.A., BAAS, **204**, 4017, 2004.
- "Mid-Infrared Observations of the Halo of NGC 5907," Ashby, M.L.N., Pipher, J.L., Forrest, W.J., Stauffer, J.R., Barmby, P., Willner, S.P., Fazio, G.G., Smith, H.A., Arendt, R.G., Bock, J.J., BAAS, **204**, 4004, 2004.
- "IRAC Extragalactic GTO Program: From Nearby Galaxies to the High Redshift Universe," Pahre, M.A., Ashby, M.L.N., Barmby, P., Fazio, G.G., Huang, J.-S., Smith, H.A., Wang, Z., Willner, S.P., Pipher, J.L., Forrest, W.J., BAAS, **204**, 3310, 2004.
- "Detecting Brown Dwarfs, Disks and Protostars with Spitzer: First Galactic Results from the IRAC GTO Program," Megeath, S.T., Allen, L.E., Calvet, N., Deutsch, L.K., Fazio, G.G., Hartmann, L., Hora, J.L., Melnick, G.J., Patten, B.M., Sicilia-Aguilar, A., Smith, H.A., Forrest, W.J., Gutermuth, R.A., Peterson, D.E., Pipher, J.L., Stauffer, J.R., BAAS, **204**, 3306, 2004.
- "The Far-Infrared Emission Line and Continuum Spectrum of the Seyfert Galaxy NGC 1068," Spinoglio, L., Malkan, M., Smith, H.A., González-Alfonso, E., and Fischer, J., ApJ (in press).
- "The Far Infrared Spectrum of Arp 220," González-Alfonso, E., Smith, H., Fischer, J., and Cernicharo, J., ApJ 2004 (in press).
- "The Composite UV to Far-IR Spectrum of NGC1068: Modeling the Ionic and Molecular Emission," Spinoglio, L., Malkan, M., Smith, H.A., González-Alfonso, E., and Fischer, J., in Proceedings of the conference *The Dusty and Molecular Universe*, Paris, 2005.
- "Star Formation as Seen by Spitzer-IRAC," Smith, H.A., L. Allen, T. Megeath, P. Barmby, N. Calvet, G. Fazio, L. Hartmann, P. Myers, M. Marengo, R. Gutermuth, J. Pipher, P. D'Alesio, B. Merin, B. Reach, T. Marston, J. Muzerolle, and Noriega-Crespa, A., in Proceedings of the conference *The Dusty and Molecular Universe*, Paris, 2005.

Appendix B. SPITZER Observations

Spitzer ERO Programs Approved

- 1) IRAC Images of an Infrared Bright Galaxy: M82
- 2) IRAC/IRS Early Release Observations of RCW 108
- 3) Observations of Interacting Galaxies
- 4) SPITZER Observations of the Galactic Center
- 5) Extremely Red Background Objects in the IRAC Survey

Spitzer GO Proposals Submitted

- 1) Spitzer Interacting Galaxy Study
- 2) Accretion Power in the Universe
- 3) Probing the Dynamic Causes of the Butcher-Oemler Effect
- 4) IRS Spectroscopy of a Complete Sample of AG Gradients in M33
- 5) Galactic Extinction
- 6) Low Redshift 3CRR Sources
- 7) The Galactic Center
- 8) The 53W002 Field of Galaxies
- 9) GALEX Study of Star Formation

Other Facility Observing Proposals

HAS was the PI on one proposal to the Hubble Space Telescope:
"NICMOS Imaging of Spitzer-Revealed Extremely Red Objects"

HAS was the PI on one LTSA proposal:
"Molecular Clouds in Interacting Galaxies"

HAS was the PI on one ADP proposal:
"Modeling Properties of Massive-Star Forming Molecular Clouds in Galactic and Extragalactic Regions from SWAS and ISO Spectroscopy"

Appendix C. Papers

- 1) **Star Formation as Seen by the Infrared Array Camera on Spitzer**
- 2) **The Far-Infrared Emission Line and Continuum Spectrum of the Seyfert Galaxy NGC 1068**
- 3) **The Far-Infrared Spectrum of Arp 220**

STAR FORMATION AS SEEN BY THE INFRARED ARRAY CAMERA ON *SPITZER*

Howard A. Smith⁽¹⁾, L. Allen⁽¹⁾, T. Megeath⁽¹⁾, P. Barmby⁽¹⁾, N. Calvet⁽¹⁾, G. Fazio⁽¹⁾, L. Hartmann⁽¹⁾, P. Myers⁽¹⁾, M. Marengo⁽¹⁾, R. Gutermuth⁽²⁾, J. Pipher⁽²⁾, P. D'Alessio⁽³⁾, B. Merin⁽⁴⁾, B. Reach⁽⁵⁾, A. Noriega-Crespo⁽⁵⁾, T. Marston⁽⁶⁾, and J. Muzerolle⁽⁷⁾

⁽¹⁾ *Harvard-Smithsonian Center for Astrophysics, 60 Garden St., Cambridge, MA USA 02139*

Email: hsmith@cfa.harvard.edu

⁽²⁾ *Dept. of Physics & Astronomy, U. Rochester, Rochester, NY USA 14627*

⁽³⁾ *Centro de Radioastronomía y Astrofísica, Apdo. Postal 72-3, 58089 Morelia, Michoacán, Mexico*

⁽⁴⁾ *Lab. de Astrofísica Espacial y Física Fund., Apartado de Correos 50727, 28080 Madrid, Spain*

⁽⁵⁾ *Spitzer Science Center, MC220-6, California Institute of Technology, Pasadena, CA USA 91125*

⁽⁶⁾ *Research & Scientific Support Div., ESTEC, 2201 AZ Noorwijk, Netherlands*

⁽⁷⁾ *Dept. of Astronomy, U. Arizona, 933 N. Cherry Ave., Tucson, AZ USA 85721*

ABSTRACT

The Infrared Array Camera (IRAC) onboard *Spitzer* has imaged regions of star formation (SF) in its four IR bands with spatial resolutions of $\sim 2''$ / pixel. IRAC is sensitive enough to detect very faint, embedded young stars at levels of tens of Jy, and IRAC photometry can categorize their stages of development: from young protostars with infalling envelopes (Class 0/I) to stars whose infrared excesses derive from accreting circumstellar disks (Class II) to evolved stars dominated by photospheric emission. The IRAC images also clearly reveal and help diagnose associated regions of shocked and/or PDR emission in the clouds; we find existing models provide a good start at explaining the continuum of the SF regions IRAC observes.

1. LOW MASS STAR FORMATION

IRAC [1] has the ability to address directly at least three of the key outstanding observational issues in SF: it can sample thoroughly the low-mass end of the IMF thanks to its great sensitivity (down to a few microJy – about 21^m at 3.6 μ m and 16^m at 8.0 μ m), and so can provide astronomers with an accurate census; it can obtain four-color photometry of the mid-IR SEDs of young stars in the spectral region where extinction effects start to become minimal; and it can image large fields-of-view to provide simultaneous information about the circumstellar and interstellar environments in which young stars form. During its first year of operations IRAC's four-band images of molecular clouds have yielded extensive color-color plots of the embedded point sources and the ISM – plots that have already provided a powerful new diagnostic tool for exploring the properties of the protostars developing in these regions. In this short paper we will attempt to give an overview on all three contributions, with a more detailed discussion of the high mass SF ongoing in DR21.

1.1 Point Sources in Young Stellar Clusters

Lori Allen and her colleagues [2] have extended the SED models of YSOs, disks, and accretion processes to the IRAC bands, including in their models the effects of an inner disk wall illuminated by the central star. Their com-

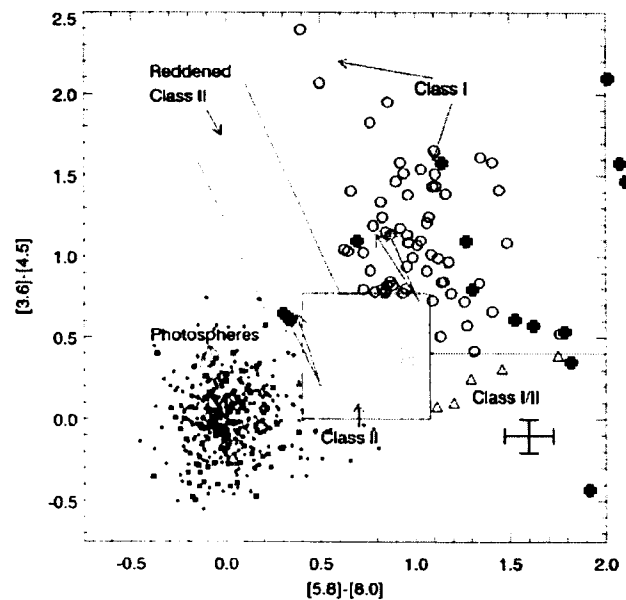


Fig. 1. An IRAC color-color plot of YSOs.

puted SEDs show that IRAC color-color plots may in many cases help to break the ambiguity in YSO class estimates that exist in traditional $[J-H]$ vs $[H-K]$ diagrams. Fig.1 labels the regions of the plot by Class as determined from the models and extinction. Allen finds as much as two magnitudes of color spread across each set of IRAC band colors in the low mass YSO diagnostic diagram. As part of the IRAC team's survey of young stellar clusters, Megeath *et al.* [3] analyzed the point sources in four young stellar clusters in clouds of comparable masses (roughly about 1000 M_{\odot} of gas in each): Cep C, S171, S140, and NGC7129. The color-

color diagram of sources for these clusters seen in Fig. 1 fills the model space more-or-less as predicted with over 200 observed YSOs. Fig. 1 also includes sources from the DR21 complex marked as filled pluses.

2. HIGH MASS STAR FORMATION

2.1 The DR21 Complex

IRAC has obtained four-color images [4] of the nebulosity and point source distribution throughout the giant cloud extending across about one degree -- from the ridge of massive SF in W75 in the north past the DR21 complex of massive stars in the south, and including the DB16 cluster in the southwest. It has been suggested [5] there is evidence for an evolutionary trend in activity across this ridge, perhaps either triggered by a cloud-cloud collision [6] or a SNR [7]; the issue is still unresolved. Fig. 2 shows a portion of the IRAC image around DR21.

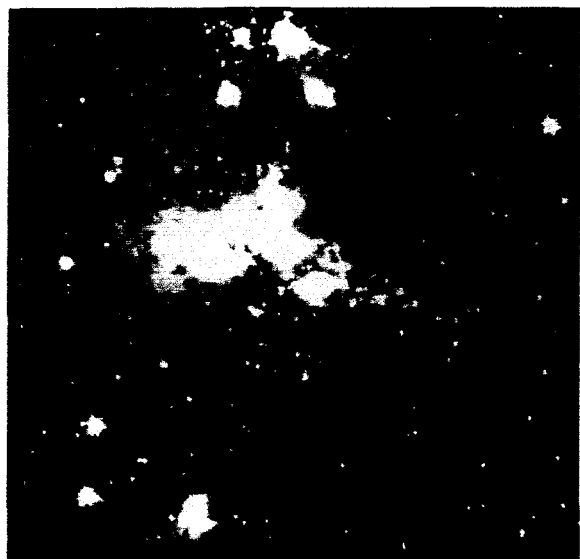


Fig. 2. The DR21 main complex as imaged by IRAC.

The DR21 cloud region is noted for having one of the most massive outflows in the galaxy with velocities of 60km/s or more and an outflow mass estimated at 3000 M_{\odot} . The force driving this flow, estimated from the shocked H_2 emission to be 5×10^{30} dynes, is larger than that in the Orion outflow [8]. The energy is in excess of 2×10^{48} ergs, and the luminosity of the H_2 flow alone is 1800 L_{\odot} . Davis and Smith [9] conclude there are both J and C-type shocks at work in the region; others [10] claim evidence for a second "highly collimated" flow perpendicular to the main one. The IRAS satellite detected a very bright source (IRAS 20372+4209, later dubbed IRS1) near the presumptive origin of the massive CO/shocked H_2 outflow, with flux densities of 62.5,

1400, 2.60×10^4 , and 2.22×10^4 Jy, respectively, in the four IRAS bands. The catalog position is 20h37m16.2s and 42d09m09s (B1950). (The radio source W75S = DR21OH is located about 3' north of IRS1; IRAC finds a weak 3.5 μ m source at this radio location.)

2.2 IRAC Photometry of DR21 Sources

IRAC has resolved hundreds of faint, red or extremely red stars in the nebulosity associated with DR21, with the dominant cluster of massive young stars lying buried in the bright western lobe near IRS1. Fifteen distinct stars are seen in this lobe by IRAC; we find several more visible in deep H-band images taken with the MMT 6.5m infrared camera. Fig. 3 plots the SEDs of these sources

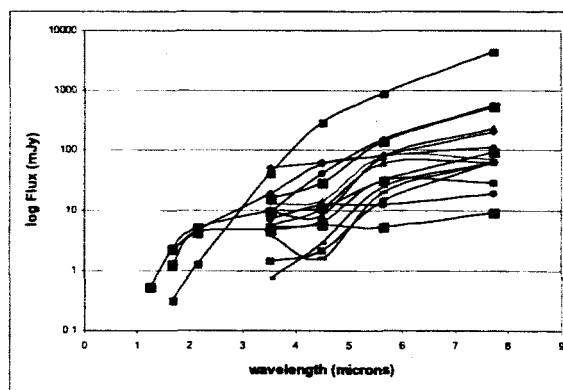


Fig. 3. SEDs of the sources in the main DR21 cloud.

from [J] (when available) through [IRAC B4]. Most sources have very steeply rising spectra, with the most extreme source being one labeled "IRAC-4." While there are 15 sources apparent in Band 1 (3.6 μ m), in Band 4 (8 μ m) there is only bright source: IRAC-4, whose flux density is ~ 2.5 Jy (it saturated the IRAC pixels). Models of YSO SEDs are able to use the spectral index α of the continuum as a measure of the stage of evolution [11]; $\alpha > 0.3$ is indicative of a Class I protostar. The SED of IRAC-4, whose $\alpha = 5.0$, suggests an even earlier stage of development like Class 0. Fig. 1 includes the DR21 YSO colors; some are so red the points fall outside the box.

2.3 The Misidentification of IRS1

IRAC, with its relatively good spatial resolution, can play a critical role in identifying unambiguously the key point sources in SF regions. Although the IRAS source IRS1 is extremely bright, the IRAS coordinates are not precise (the IRAS PSC does not include it, but it is in the IRAS Serendipitous Survey which has greater depth and sensitivity in confused areas like DR21). The position does not correspond with any other known source: it lies 6.2" ENE of a [K]= 14.5mag 2MASS source, 2MASS 20390353+4219420, and about 55"WNW of the radio

source DR21(CO). 6cm continuum observations [12] found four compact HII regions in this region with the northern-most source, “D”, at 20h39m01.25s +42d19’53.4”(J2000), attributed to an O8 ZAMS star. Recent VLA observations in the recombination lines [10] attribute the radio emission to a dual cometary HII region, with source “D” being responsible for one of them. A near-IR study of compact HII regions [13] concludes the main radio sources in DR21 have no NIR counterpart and therefore may have little to do with the SF in the region. In the FIR, Colome [14] mapped the source from the KAO at 50 m and 100 m and report flux densities of $1.58 \times 10^4 \text{Jy}$ and $3.86 \times 10^4 \text{Jy}$, respectively, consistent with IRAS values, but their absolute positions are considerably less certain than the IRAS ones [15].

The first reference to IRS1 and its position is in [16] which cites the position (K-band) as 20h37m13.4s +42d08m59s. (Earlier papers do not mention IRS1: [12] for example imaged the region in the IR and Br but did not note that source “D” is 11" away). But, according to [17]) the identification of IRS1 in [16] was simply made on the basis of it being the brightest 2 m source in the region. [9] and [18] locate IRS1 on their shocked H₂ images, but the position is based on [16] – none of these authors demonstrate that the source they label IRS1 is actually the IRAS source with 63Jy of flux at 12 m. If this IRAS flux is approximately correct we would expect to see it very clearly in IRAC Band 4; we don’t. Furthermore, we find the source located at the position of the [16] “IRS1 star” has flux densities of 19.2mJy, 58.5mJy, 81.4mJy, and 115mJy in the four IRAC bands respectively (the Band 4 flux is confused by strong diffuse emission). We conclude that IRS1 has been misidentified in previous visible and near infrared studies, and that by far the most luminous star, presumably a key player in the dynamics, is a faint field star that was previously unnoticed: IRAC-4.

2.4 The Luminous Source IRAC-4

IRAC-4, at 20h39m01.21s +42d19’54.0”(J2000), lies about 23" WNW of the nominal IRAS “IRS1” location. There is no 2MASS source found at this location near the edge of the most heavily obscured portion of the dark lane, but our MMT 6.5-m [H] images see it clearly. If the IRAS flux densities are correct and only the position is uncertain (consistent with the KAO 50 m photometry of the source [14]), then at a distance of about 3 kpc the total luminosity is equivalent to that from an O8 ZAMS star as previously suggested [12]. For an O8 ZAMS star to have these observed infrared fluxes, and in particular to be over 1000 times fainter at 2.2 m than at 8 m, the extinction to the source must be approximately $A_V \sim 175$, a number in rough agreement with estimates of the general region from Br and radio continuum observations [12].

The 14 other sources IRAC finds in the bright western lobe, at the base of the outflow, include some which are also associated with compact HII regions and probably also are O stars. Fig. 1 contains points for these sources, most of which fall outside the region associated with Class II accretion-disks but are well within the region encompassed by envelope models.

3. THE MASSIVE PROTOSTAR IN DR21

We argue that IRAC-4 = IRS1 is a high mass YSO -- a star that is old enough to have developed a compact HII region and powerful wind, but which is still surrounded by a hot, infalling envelope. High mass YSOs are observationally rare in part because they evolve quickly, are hard to identify due to the obscuration that still surrounds them, and because they form in complex clusters. Partly as a result they are less well understood than their low-mass (T-Tauri-like) counterparts. IRAC-4 is coincident with the radio continuum source “D.” An O8 ZAMS star has a luminosity of $6.5 \times 10^4 L_\odot$, but the FIR luminosity of the source [14] is about one order of magnitude larger, $5 \times 10^5 L_\odot$ (assuming $d=3\text{kpc}$). Some correction must be made for the contribution of the rest of the cluster to the IRAS and KAO fluxes, but it appears that the majority of the luminosity of IRAC-4 does not come from the stellar photosphere; we suggest it comes from accretion.

Osoorio *et al.* [19] note that most young embedded massive stars have large accretion rates ($>4 \times 10^{-4} \text{Mo/yr}$) that power a luminosity that exceeds the stars’ photospheres, but add that most have not yet had time to develop a compact HII region; they find $\sim 1.5 \times 10^5 L_\odot$ can be produced from a hot core with an infall. IRAC-4, therefore, which does appear to host a compact HII region, is presumably in the process of moving from the “hot molecular core” phase onto the main-sequence but is still surrounded by a dust envelope (and/or perhaps a disk; [2; 20]), putting its age at much less than $\sim 1\text{MY}$ and perhaps even less than 10^5 years. The SED of IRAC-4 rises steeply, in agreement with other candidate high mass YSOs [21,22] although some of its SED arises in part because of the extinction at K-band; it rises at longer wavelengths because of this warm dust from the accreting envelope [20]. IRAC-4 may not be only contributor to the outflow however. From our data we cannot determine how many of the 15 core stars have outflows, or whether the massive DR21 outflow is the result of multiple outflows, but multiple, non-aligned flows might be present. [10] argues that the HII region source “D” associated with IRAC-4 has a cometary morphology and that, together with radio source “A” (our source IRAC-10) it forms a dual, nearly perpendicular cometary flow. Smith and Fischer [23] first suggested that there were probably multiple outflows in such regions. One of the complexities in modeling high mass star formation is the powerful radiation which tends to inhibit the envelope

accretion. The IRAC-4 source, which is coincident with an HII region at 6 cm, appears to be a rare example of a massive young star which has evolved to produce a compact HII region, but which is still surrounded by an accreting dust envelope – the outflow thereby provides strong evidence that the current accretion is not symmetric.

4. THE MASSIVE OUTFLOW IN DR21

The IRAC maps distinctly reveal the massive outflow in DR21, as well as image the diffuse, extended PDR regions nearby. Comparison between the IRAC outflow images and 2 m shocked H₂ images shows a very close structural correspondence. Strong lines of $v=1-0$ CO, Br α , and PAHs features fall in the IRAC bandpasses, and these species have been proposed as being dominant contributors to the band fluxes. However there are over 70 detectable H₂ lines that also fall in the IRAC range, most of which have never before been observed. We have estimated their contribution to the IRAC images of DR21 using a range of PDR parameters [24] and C-shock parameters [25]. Fig.4 plots (as filled circles) the colors expected from H₂ line emission across a range of likely conditions for PDRs and shocks; it also plots the emission expected from diffuse PDR illuminated grains [26]. The figure also plots the range of observed ISM colors (dotted area). The outflow region's points mostly fall across the upper and central range of the dotted zone, while the diffuse ISM points (far from the outflow) have colors at

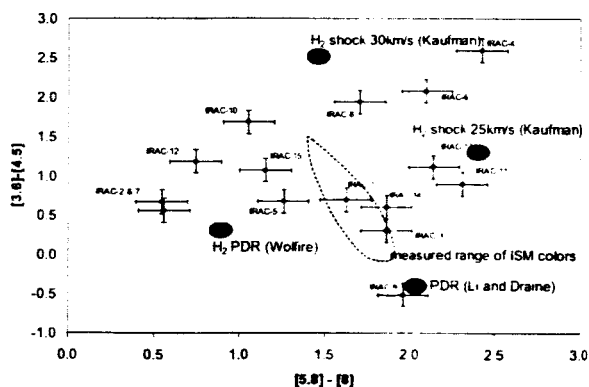


Fig. 4. Colors of the DR21 ISM, with point sources. The dotted range spans the observed ISM colors in both the outflow and the diffuse ISM: filled circles are representative theoretical predictions.

the lower right of the dotted range. Our preliminary results confirm what had previously been suspected - that the outflow is not the result of a simple, single C-shock but rather is a blend of several sets of conditions. The ISO satellite measured the H₂ 0-0 S(5) 6.91 m flux in DR21 [18]. The value implies that (depending somewhat on the details of the C-shock) the H₂ lines as a group are the dominant contributors (~30% - 60%) to the total flux

observed in IRAC Bands 2 and 3. This conclusion helps to explain the close similarities between the 2 m and IRAC images of outflow structures. The diffuse PDR models [26] are found to deviate from observed ISM colors by about 0.5mag.

5. ACKNOWLEDGMENTS

This work is based on observations with the *Spitzer* Space Telescope, with support provided by NASA contract 12256790 issued JPL/Caltech. We also gratefully acknowledge support from NASA grant NAG5-10659.

6. REFERENCES

1. Fazio *et al.* ApJS, **154**, 10, 2004.
2. Allen *et al.* ApJS, **154**, 363, 2004.
3. Megeath *et al.* ApJS, **154**, 367, 2004.
4. Marston *et al.* ApJS, **154**, 367, 2004.
5. Wilson and Mauersberger, A&A, **239**, 305, 1990.
6. Dickel, Ho and Wright, ApJ, **290**, 256, 1985.
7. Ward-Thompson *et al.*, MARAS, **248**, 670, 1991.
8. Garden *et al.*, MNRAS, **220**, 203, 1986.
9. Davis, C.J. and Smith, M.D., A&A, **310**, 961, 1991.
10. Cyganowski *et al.*, ApJ **596**, 344, 2003.
11. Green *et al.*, ApJ **434**, 618, 1994.
12. Roelfsema *et al.*, A&A, **222**, 247, 1989.
13. Hanson *et al.*, ApJS, **138**, 35, 2002.
14. Colome *et al.*, ApJ **447**, 236, 1995.
15. Paul Harvey, private communication, 2004.
16. Garden *et al.*, ApJ, **354**, 232, 1990.
17. Michael Burton, private communication, 2004.
18. Smith, *et al.*, MNRAS, **297**, 687, 1998.
19. Osorio, Lizano, and D'Alessio, ApJ **525**, 808, 1999.
20. Whitney *et al.*, ApJ **598**, 1079, 2003.
21. Sridharan *et al.*, ApJ **566**, 931, 2002.
22. Noriega-Crespo *et al.* ApJS, **154**, 402, 2004.
23. Smith and Fischer, ApJL. **398**, L99, 1992.
24. Wolfire, private communication, 2004.
25. Kaufman and Neufeld, ApJ, **456**, 611, 1996.
26. Li and Draine, ApJ, **554**, 778, 2001.

The far-infrared emission line and continuum spectrum of the Seyfert galaxy NGC 1068¹

Luigi Spinoglio

*Istituto di Fisica dello Spazio Interplanetario, CNR, via Fosso del Cavaliere 100, I-00133
Roma, Italy*

luigi@ifsi.rm.cnr.it

Matthew A. Malkan

Physics & Astronomy Dept., UCLA, Los Angeles, CA 90095, USA

malkan@astro.ucla.edu

Howard A. Smith

Harvard-Smithsonian CfA, 60 Garden St., Cambridge, MA 02138, USA

hsmith@cfa.harvard.edu

Eduardo González-Alfonso

*Universidad de Alcalá de Henares, Departamento de Física, Campus Universitario,
E-28871 Alcalá de Henares, Madrid, Spain*

eduardo.gonzalez@uah.es

Jacqueline Fischer

Naval Research Laboratory, Code 7213, Washington DC 20375, USA

Jackie.Fischer@nrl.navy.mil

ABSTRACT

We report on the analysis of the first complete far-infrared spectrum (43-197 μ m) of the Seyfert 2 galaxy NGC 1068 as observed with the *Long Wavelength Spectrometer* (LWS) onboard the *Infrared Space Observatory* (ISO). In addition to the 7 expected ionic fine structure emission lines, the OH rotational lines at 79, 119 and 163 μ m were all detected in emission, which is unique among galaxies with full LWS spectra, where the 119 μ m line, where detected, is always in

absorption. The observed line intensities were modelled together with ISO *Short Wavelength Spectrometer* (SWS) and optical and ultraviolet line intensities from the literature, considering two independent emission components: the AGN component and the starburst component in the circumnuclear ring of $\sim 3\text{kpc}$ in size. Using the UV to mid-IR emission line spectrum to constrain the nuclear ionizing continuum, we have confirmed previous results: a canonical power-law ionizing spectrum is a poorer fit than one with a deep absorption trough, while the presence of a *big blue bump* is ruled out. Based on the instantaneous starburst age of 5 Myr constrained by the Br γ equivalent width in the starburst ring, and starburst synthesis models of the mid- and far-infrared fine-structure line emission, a low ionization parameter ($U=10^{-3.5}$) and low densities ($n=100\text{ cm}^{-3}$) are derived. Combining the AGN and starburst components, we succeed in modeling the overall UV to far-IR atomic spectrum of NGC 1068, reproducing the line fluxes to within a factor 2.0 on average with a standard deviation of 1.4. The OH 119 μm emission indicates that the line is collisionally excited, and arises in a warm and dense region. The OH emission has been modeled using spherically symmetric, non-local, non-LTE radiative transfer models. The models indicate that the bulk of the emission arises from the nuclear region, although some extended contribution from the starburst is not ruled out. The OH abundance in the nuclear region is expected to be $\sim 10^{-5}$, characteristic of X-ray dominated regions.

Subject headings: galaxies: individual (NGC 1068) - galaxies: active - galaxies: nuclei - galaxies: Seyfert - galaxies: emission lines - galaxies: starburst - infrared: galaxies.

1. INTRODUCTION

NGC 1068 is known as the archetypical Seyfert type 2 galaxy. It is nearby, luminous ($L_{\text{IR}} = 2 \times 10^{11} L_{\odot}$ Bland-Hawthorn et al. 1997), and it has been extensively observed and studied in detail from X-rays to radio wavelengths. With a measured redshift of $z=0.0038$ (Huchra et al. 1999) (corresponding to a distance of $D=15.2\text{ Mpc}$ for $H_0=75\text{ km s}^{-1}\text{ Mpc}^{-1}$), it provides a scale of only $\sim 74\text{ pc}''$. A central nuclear star cluster has an extent of $\sim 0.6''$

¹ISO is an ESA project with instruments funded by ESA Member States (especially the PI countries: France, Germany, the Netherlands and the United Kingdom) and with the participation of ISAS and NASA.

(Thatte et al. 1997) and a 2.3 kpc stellar bar observed in the near-IR (Scoville et al. 1988; Thronson et al. 1989) is surrounded by a circumnuclear starburst ring. Telesco et al. (1984) found that the infrared emission in NGC 1068 was due to both the Seyfert nucleus (which dominates the $10\mu\text{m}$ emission) and to the star forming regions in the bright $\sim 3\text{kpc}$ circumnuclear ring (which emits most of the luminosity at $\lambda > 30\mu\text{m}$). A $Br\gamma$ imaging study (Davies, Sugai & Ward 1998) showed a similar morphology and indicated that a short burst of star formation occurred throughout the circumnuclear ring of $15\text{-}16''$ in radius within the last 4-40 Myr. CO interferometer observations revealed molecular gas very close to the nucleus ($\sim 0.2''$) suggesting the presence of $\sim 10^8 M_\odot$ within the central 25pc (Schinnerer et al. 2000). Recent high resolution H_2 line emission mapping indicates the presence of two main nuclear emission knots with a velocity difference of 140 km/s, which, if interpreted as quasi-keplerian, would imply a central enclosed mass of $10^8 M_\odot$ (Alloin et al. 2001).

In this article, we present the first complete far-infrared spectrum from 43 to $197\mu\text{m}$ showing both atomic and molecular emission lines (§2). We model the far-IR continuum emission using a radiative transfer code and gray body functions (§3) and model the composite UV- to far-IR atomic emission line spectrum, from our data and the literature, using photoionization models of both the active nucleus (§4.1) and the starburst components (§4.2-4.3). Moreover, two different non-local, non-LTE radiative transfer codes have been used to model the OH lines (§5). Our conclusions are then given in §6.

2. OBSERVATIONS

NGC 1068 was observed with the Long Wavelength Spectrometer (LWS) (Clegg et al. 1996) on board the Infrared Space Observatory (ISO) (Kessler et al. 1996), as part of the Guaranteed Time Programme of the LWS instrument team. The full low resolution spectrum ($43\text{-}197\mu\text{m}$) of NGC 1068 was collected during orbit 605 (July 13, 1997). Two on-source full scans (15,730 seconds of total integration time) and two off-source ($6' \text{ N}$) scans of the [CII] $158\mu\text{m}$ line (3,390 seconds of total integration time) were obtained. On- and off-source scans had the same integration time per spectral step. Because of the design of the LWS spectrometer, simultaneously with the $158\mu\text{m}$ data, a short spectral scan of equal sensitivity to the on-source spectrum was obtained at sparsely spaced wavelengths across the LWS range.

The LWS beam is roughly independent of wavelength and equal to about 80 arcsec. The spectra were calibrated using Uranus, resulting in an absolute accuracy better than

30% (Swinyard et al. 1996). The data analysis has been done with ISAP², starting from the auto-analysis results processed through the LWS Version 7-8 pipeline (July 1998). To be confident that newer versions of the pipeline and calibration files did not yield different results, we have compared our data with the results obtained using pipeline 10.1 (November 2001) and we did not find significant differences in the line fluxes or the continuum.

All the full grating scans taken on the on-source position and the two sets of data on the off-source position were separately co-added. No signal was detected in the off-source coadds. The emission line fluxes were measured with ISAP, which fits polynomials to the local continuum and Gaussian profiles to the lines. In all cases the observed line widths were consistent with the instrumental resolution of the grating, which was typically 1500 km/sec. The integrated line fluxes measured independently from data taken in the two scan directions agreed very well, to within 10%. The on source LWS spectrum that resulted from stitching the ten LWS channels together using small multiplicative corrections in order to match the overlapping regions of each channel with its neighbors is shown in Fig. 1. LWS spectra of sources that are very extended within the instrument beam or that peak off center are typically affected by channel fringing in the continuum baseline (Swinyard et al. 1998). Fortunately, these spurious ripples are hardly noticeable in our LWS spectrum, presumably because the far-IR continuum is centrally concentrated towards the center of the LWS 80" beam.

Besides the LWS observations, we also use the SWS observations presented by Lutz et al. (2000), to extend the wavelength and ionization-level coverage. Table 1 presents all the ISO line flux measurements including those from the SWS with their respective aperture sizes.

3. THERMAL CONTINUUM SPECTRUM

We have modeled the mid- and far-infrared spectral energy distribution (SED) of NGC 1068 by means of a non-local, spherically symmetric, radiative transfer code (González-Alfonso & Cernicharo 1997, 1999). We modeled the nuclear continuum emission closely following the approach by Cameron et al. (1993), and using the ISO-SWS fluxes reported by Lutz et al.

²The ISO Spectral Analysis Package (ISAP) is a joint development by the LWS and SWS Instrument Teams and Data Centers. Contributing institutes are Centre d'Etude Spatiale des Rayonnements (France), Institute d'Astrophysique Spatiale (France), Infrared Processing and Analysis Center (United States), Max-Planck-Institut für Extraterrestrische Physik (Germany), Rutherford Appleton Laboratories (United Kingdom) and the Space Research Organization, Netherlands.

(2000). A central source with luminosity $1.5 \times 10^{11} L_{\odot}$ illuminates a spherically symmetric dust envelope with inner and outer radii of 1 and 200 pc, respectively. The envelope is divided into a set of spherical shells where the dust temperature is computed assuming that heating and cooling are equal. We assumed a standard silicate/amorphous carbon mixture with optical constants given by Draine (1985) and Preibisch et al. (1993). The density profile was assumed to be $\propto r^{-\beta}$, with β and the density at the inner radius regarded as free parameters. The predicted flux densities were compared with the continuum observed in the SWS spectrum by assuming that the bulk of the continuum in the 2-45 μm range arises from the nuclear region (see below). A reasonable fit to the observed mid-infrared SED is shown in Fig. 1, where $\beta = 1$ and, assuming a gas-to-dust mass ratio of 10^2 , the averaged H_2 density at the inner radius is $\langle n_I(\text{H}_2) \rangle = 1.7 \times 10^3 \text{ cm}^{-3}$, the radial H_2 column density is $N(\text{H}_2) = 2.7 \times 10^{22} \text{ cm}^{-2}$, and the total mass is $M = 2.1 \times 10^7 M_{\odot}$. The values of $N(\text{H}_2)$ and M are in agreement with those inferred by Helfer & Blitz (1995).

The main weakness of our nuclear model is that the flux density at 30-50 μm is somewhat overestimated, a problem that could be more severe if there is a contribution to the continuum emission in the SWS aperture by the extended starburst at $\lambda > 30 \mu\text{m}$. On the other hand, the decomposition of the mid-infrared emission performed by Le Floch et al. (2001) with ISOCAM into the nuclear and extended contributions attributes to the nucleus, between 2 and 16 μm , significantly higher flux densities than those reported by Lutz et al. (2000) within the SWS aperture, suggesting that uncertainties in absolute calibration are affecting one or both data sets. Although our continuum model for the nuclear region is thus reasonable within the uncertainties, the nuclear continuum emission in the 30-50 μm range could be overestimated by a factor as high as 2. The latter is relevant for the analysis of the OH emission because, as we argue in section §5, the relative contributions of the nuclear and the extended components of the 30-50 μm continuum are important in discerning which component is responsible for the OH emission lines.

The complete far-infrared continuum emission is fitted in Fig. 1 by adding two components at 32 K and 20 K (Spinoglio, Andreani & Malkan 2002). These are gray body functions with a steep ($\beta = 2$) dust emissivity law. We identify the 32 K component with the starburst ring that is well delineated by the PAH 7.7 μm emission (Le Floch et al. 2001). Assuming a spherical shell with radius of 1.5 kpc and thickness of 0.3 kpc, the average H_2 molecular density of the 32 K component is $\approx 5 \text{ cm}^{-3}$. The total mass is $1.6 \times 10^9 M_{\odot}$ and $2 \times 10^9 M_{\odot}$ for the 32 K and 20 K components, respectively. These estimates are in good agreement with the $\sim 4 \times 10^9 M_{\odot}$ derived by Planesas et al. (1991) for the molecular ring.

4. THE FINE STRUCTURE LINES

To be able to better constrain the modeling of the line emission of NGC 1068, we have combined our far-infrared fine structure line measurements (Table 1) with ultraviolet, optical and infrared spectroscopic data from the literature (Kriss et al. 1992; Marconi et al. 1996; Thompson 1996; Lutz et al. 2000). The complete emission line spectrum of NGC 1068 from the ultraviolet to the far-IR includes several low-ionization lines that are primarily produced outside the narrow line region (NLR) of the active nucleus, as well as intermediate ionization lines that originate from both starburst and AGN emission. For this reason, we find that no single model satisfactorily explains all the observed emission lines. We identify two main components:

- an AGN component (the NLR), exciting the high ionization lines and contributing little to the low-to-intermediate ionization lines;
- a starburst component in the circumnuclear ring of the galaxy (e.g. Davies, Sugai & Ward 1998) that produces the low ionization and neutral forbidden lines and some of the emission in the intermediate ionization lines. This component should also produce emission associated with photo-dissociation regions (PDRs) (e.g. Kaufman et al. 1999), at the interface with the interstellar medium of the galaxy.

In this section, we will examine separately the two components that produce the total fine structure emission line spectrum of NGC 1068, namely the AGN and the starburst, for which we propose two different computations, and we add together these components to reproduce the overall observed spectrum from the UV to the far-IR in §4.3.

4.1. Modeling the AGN

The first photoionization model predictions of the mid to far-infrared emission line spectra of the Narrow Line Regions (NLR) of active galaxies were presented by Spinoglio & Malkan (1992), well before the ISO observations could be collected. Alexander et al. (2000) used the observed high ionization emission lines to model the obscured ionizing AGN continuum of NGC 1068 and found that the best-fit spectral energy distribution (SED) has a deep trough at 4 Rydbergs, which is consistent with an intrinsic “big blue bump” that is partially obscured by $\sim 6 \times 10^{19} \text{ cm}^{-2}$ of neutral hydrogen interior to the NLR. Following their results, we have simulated their models, although using a different photoionization code, *CLOUDY* (Version 94.00 Ferland 2000), and then we have varied the shape of the ionizing continuum

to include the ionizing continuum derived in Pier et al. (1994). Our goal was to test if the Alexander et al. (2000) results were unique and to fit the remaining emission by a starburst component, and thereby to derive a composite model of the complete emission line spectrum of NGC 1068.

Specifically, we explore three plausible AGN SEDs. Model A assumes the best fit ionizing spectrum derived by Alexander et al. (2000), i.e. with a deep trough at 4 Rydberg ($\log f = -27.4, -29.0, -27.4, -28.2$ at 2, 4, 8 and 16 Ryd, respectively). An intrinsic nuclear spectrum of NGC 1068 has also been inferred by Pier et al. (1994). Model B assumes the original ionizing spectrum derived from Pier et al. (1994). Model C assumes an SED with a *Big Blue Bump* superposed on the Pier et al. (1994) ionizing continuum ($\log f = -25.8, -25.8, -25.8, -27.4$ at 2, 4, 8 and 16 Ryd, respectively) as expected for the thermal emission of an accretion disk around a central black hole. These three AGN ionizing continua are plotted in Fig. 2. For each of models A, B, and C, we have used two component models with the same parameters as in Alexander et al. (2000): component 1 has a constant hydrogen density of 10^4 cm^{-3} , an ionization parameter $U=0.1$, a covering factor $c=0.45$, a filling factor of 6.5×10^{-3} with a radial dependence of the form r^{-2} , and extends from ~ 21 to ~ 109 pc from the center; component 2 has a density of $2 \times 10^3 \text{ cm}^{-3}$, an ionization parameter $U=0.01$, a covering factor of $c=0.29$, a filling factor of 6.5×10^{-4} without any radial dependence, and extends from ~ 153 to ~ 362 pc from the center. We have also assumed the “low oxygen” abundances adopted by Alexander et al. (2000), in order to be able to compare our results with theirs. The inner and outer radii of the emission regions of the two components, 21, 109, 153 and 362 pc. correspond to angular distances of about 0.26, 1.4, 1.9 and 4.5 ″, respectively. Table 2 reports the predicted line fluxes of the three AGN models, A, B, and C, together with the observed line fluxes: the line fluxes are given for each of the two components 1 and 2, which are treated as independent, and the total flux for each model is simply the sum of the fluxes of the two components.

We can see from Table 2 that only the AGN A and B models, and not the AGN C model, reproduce most of the observed high ionization line fluxes. The low and intermediate ionization lines, are expected to have partial or full contributions from starburst and PDR components (see §4.2). This first result rules out the presence of a “big blue bump” in the ionizing continuum of NGC 1068. To be able to compare the modeled ultraviolet and optical lines with the observations, we also listed in Table 2 and 3 their dereddened fluxes, assuming two values for the extinction: $E_{B-V} = 0.4$ mag (Malkan & Oke 1983) and $E_{B-V} = 0.2$ mag (Marconi et al. 1996). We find that the AGN B model overpredicts several of the intermediate ionization lines, such as [SIV]10.5 μm , [NeIII]15.6 μm and [SIII]18.7 μm , and this discrepancy increases when adding the starburst component because these lines are also copiously produced by that component (see next section). On the other hand, the

[NeII]12.8 μ m emission is underpredicted so much so that even with the inclusion of the starburst component it cannot be reproduced with this model. As we discuss further in §4.3, a composite AGN/starburst model using AGN model A is able reproduce the [NeII]12.8 μ m emission to within the measurement errors.

4.2. Modeling the starburst ring

NGC 1068 is known to emit strong starburst emission from the ring-like structure at a radial distance of 15 – 16" from the nucleus (total size of \sim 3kpc), traced for example by the Br γ emission (Davies, Sugai & Ward 1998). Mid-IR line imaging observations of NGC 1068 have been published by Le Floc'h et al. (2001) based on ISOCAM CVF observations. They presented an image of the 7.7 μ m PAH feature that shows constant surface brightness above the 4th contour near the nucleus. This suggests that star formation is occurring in the direction of the nucleus so that nuclear spectra will include some emission from star formation. In the case of the SWS observations that we are modeling (reported by Lutz et al. (2000)), three apertures were used at different wavelengths with the two largest also including portions of the brighter starburst ring (see Table 1). To estimate how much of the starburst emission is contained in the different apertures used in the observations, we have used a continuum subtracted image in the 6.2 μ m feature produced by C. Dudley (private communication) using the same ISOCAM CVF data set examined by Le Floc'h et al. (2001). The 6.2 μ m feature is more isolated than the 7.7 μ m feature, which is blended with the 8.7 μ m feature and the silicate absorption feature, but the image compares well with the published 7.7 μ m image though we have zeroed out the residuals in a 3×12 arcsec² region centered on the nucleus. Based on this image, the SWS 14×20 , 14×27 and 20×33 arcsec² slits contain 13, 23 and 46% of the 6.2 μ m flux contained in the LWS beam respectively, without correction for the neglected region of poor residuals (oriented at 45° to our synthetic SWS slits). Since PAH features are thought to be a good tracer of PDRs and their associated starbursts, we adopt these percentages in our model predictions of SWS line strengths in the starburst models presented in this section. Further, in fitting our starburst models to the observations, we have abandoned the requirement to obtain the absolute fluxes observed at earth, but rather normalized the emission to the intensity of the [NII]122 μ m line observed with the LWS, because it has virtually no emission from any AGN model.

We have chosen the starburst synthesis modeling program Starburst99 (Leitherer et al. 1999), to produce input ionizing spectra for the *CLOUDY* photoionization code. We compared the predictions of two different ionizing continua shown in Fig. 3. The first is based on an instantaneous star formation law, with a total mass of $M = 10^6 M_{\odot}$, while the

second is based on a continuous star formation law with a star formation rate of $1 M_{\odot} \text{ yr}^{-1}$. For both types of models we adopted an age of 5 Myr, a Salpeter IMF ($\alpha=2.35$), a lower cut-off mass of $1 M_{\odot}$, an upper cut-off mass of $100 M_{\odot}$, solar abundances ($Z=0.020$) and nebular emission included. These particular ionizing continua were selected because they are consistent with the Br γ equivalent width observed by Davies, Sugai & Ward (1998) in the starburst ring. We have estimated that the Br γ equivalent width in each of the individual regions of the map of Davies, Sugai & Ward (1998) is in the range 110-180 Å. According to the Leitherer et al. (1999) models (see their figures 89 and 90), for a value of $\log(W(\text{Br } \gamma, \text{Å})) \geq 2$ only instantaneous models with ages less than $\sim 6 \times 10^6$ yrs are allowed; similarly, only continuous models with ages less than $\sim 10^7$ yrs are permitted.

We report in Table 3 the line fluxes predicted for six different starburst models, choosing the above instantaneous star formation law model as the input ionizing continuum and using *CLOUDY* with densities of $n_H = 10, 100, 1000 \text{ cm}^{-3}$ and ionization parameters of $\text{Log } U = -2.5, -3.5$. We have also run models with the continuous star formation law presented above, but we do not list their results in Table 3, because the differences in the line flux predictions are insignificant, while line fluxes strongly depend on the choice of density and ionization parameter, as can be seen from Table 3. This result is not surprising because the two ionizing continua as derived from the starburst models are in fact quite similar in their shape and we are not computing absolute line intensities, but only their ratios to a particular observed line. We have also tried continuous starburst models with much longer ages (10, 20 and 100×10^6 years) but, because the shape of the ionizing continuum again does not change significantly, the resulting emission line spectrum was indistinguishable from that one derived from the models with an age of 5×10^6 years.

In all models the abundances were those of HII regions with grains included. The integration was allowed to run until the temperature of the gas in the cloud cooled to $T=50$ K in order to include the photodissociation regions present at the interfaces of HII regions and molecular clouds.

It is clear from Table 3 that the models with the higher ionization parameter ($\log U = -2.5$) can easily be ruled out, because their emission in many intermediate ionization lines is far too high (see e.g. $[\text{OIV}]26\mu\text{m}$, $[\text{OIII}]51,88\mu\text{m}$, $[\text{NIII}]57\mu\text{m}$). Moreover, the intermediate density of $n_H = 100 \text{ cm}^{-3}$ gives the best fit to the observed lines, taking into account that the AGN component must be added to reproduce the total flux as shown §4.3.

We estimate the average PDR parameters using the models of Kaufman et al. (1999) and the contour plots in Luhman et al. (2003), the measured $[\text{C II}]158$ and $[\text{O I}]145 \mu\text{m}$ line fluxes (but not the $[\text{O I}]63 \mu\text{m}$ line flux which may be affected by absorption and/or shocks), and the FIR flux integrated over the LWS spectrum, which we find to be 1.3×10^{-8} ergs

$\text{cm}^{-2} \text{sec}^{-1}$. Here we assume that the [C II] line emerges predominantly from PDRs due to the strong starburst, rather than the diffuse ionized medium. With this assumption, the average PDR gas density and UV radiation field are $n_{H_2} \sim 1000$ and $G_0 \sim 300$ respectively. We note that if instead we assume that the [C II] line flux is dominated by the diffuse ionized medium, using the correction factor estimated by Malhotra et al. (2001), we obtain a similar gas density $n_{H_2} \sim 1500$ but a significantly higher interstellar radiation field $G_0 \sim 1500$. For both cases, the parameters derived are in the range of those of the normal galaxies in the Malhotra et al. (2001) sample, consistent with the assumption that most of the FIR flux originates in the starburst ring.

4.3. Adding the two components

Summing the line intensities of each one of the two components, the composite spectrum of NGC 1068 can be derived and compared with the observed one. We have chosen three combinations to compute the composite models, each one with a different AGN model, while we adopted the starburst model with $n_H = 100 \text{ cm}^{-3}$ and $\text{Log } U = -3.5$: 1) the first one (that we name CM1, for Composite Model 1) with the AGN ionizing continuum as suggested by Alexander et al. (2000) (model AGN A); 2) the second (CM2) with the original Pier et al. (1994) (model AGN B); 3) the third (CM3) with the hypothetical bump (model AGN C). The results of these three composite models are given in Table 4, compared to the observed and dereddened values, assuming the two choices for the extinction (see §4.1). We also show the results of the three composite models in a graphical way in Fig. 4, where the modeled to the observed flux ratio is given for each line for the case of an extinction of $E_{B-V}=0.2$ mag.

A simple χ squared test of the three models resulted in a reduced χ square of 11.9, 24.6 and 241 for the three models CM1, CM2 and CM3, respectively. We note that for CM1 the line fluxes are reproduced to within a factor of 2.0 on average with a standard deviation of 1.4 including all of the detected lines for the model with $E_{B-V}=0.2$ mag. The infrared lines only are reproduced to within a factor of 1.6 on average with a standard deviation of 0.9.

5. THE OH LINES

5.1. General remarks

In NGC 1068, we detect three of the OH rotational lines, all in emission. As shown in the energy level diagram of Fig. 5, two of them are fundamental lines, connecting the ground state $^2\Pi_{3/2}3/2$ level with the $^2\Pi_{3/2}5/2$ (the in-ladder 119 μm line) and with the $^2\Pi_{1/2}1/2$

level (the cross ladder $79\ \mu\text{m}$ line). The third line is the lowest transition of the $^2\Pi_{1/2}$ ladder: the $163\ \mu\text{m}$ line between the $J=3/2$ and $J=1/2$ levels. The detected line fluxes are given in Table 1. The fact that these three lines are *all* in emission is in striking contrast with the OH lines observed in other bright infrared galaxies, such as Arp 220 (Fischer et al. 1999; González-Alfonso et al. 2004), Mrk 231 (Harvey et al. 1999), NGC 253 (Bradford et al. 1999), and M 82 (Colbert et al. 1999), in which the $119\ \mu\text{m}$ fundamental is in absorption. The $79\ \mu\text{m}$ line is sometimes seen in emission and sometimes in absorption; the $163\ \mu\text{m}$ line is always seen in emission. In addition to the detections, the ISO-LWS and SWS observations provide upper limits on fluxes of the other four lines that arise between the lowest six rotational levels. The LWS spectra in the vicinity of the detected lines (and of one of the upper limits), are shown in detail in Fig. 6 (histograms). In this section we discuss the physical conditions necessary to excite these lines, their probable location within NGC 1068, and detailed model fits to their fluxes. A comparison between the observed and modeled line fluxes is given in Table 5 and shown in Fig. 6.

5.2. The excitation mechanism of the OH lines

The unique OH emission line spectrum of NGC 1068 can provide a powerful way to help discriminate between the properties of the molecular clouds in NGC 1068 and the clouds in other galaxies in which OH has been observed. Before describing our detailed radiative transfer calculations, it is instructive to discuss some conclusions that are model-independent. The emission in the OH $\Pi_{3/2}\ 5/2 - 3/2$ line at $119\ \mu\text{m}$ cannot be explained by absorption of far-infrared photons followed by cascade down to the upper $\Pi_{3/2}\ 5/2$ level of the transition. Rather, we argue that collisional excitation dominates. Figure 5 shows the energy level diagram of OH. There are only two possible paths to excite the $119\ \mu\text{m}$ line via absorption of far-infrared photons: via the $35\ \mu\text{m}$ and/or the $53\ \mu\text{m}$ ground-state lines. Excitation by either of these routes has other observable consequences. In the case of simple radiative cascading, the Einstein- A coefficients of the lines involved in the corresponding cascades are such that if the $35\ \mu\text{m}$ absorption path were responsible for the observed $119\ \mu\text{m}$ line flux, then the OH $\Pi_{1/2}\ 5/2 - 3/2$ line at $98.7\ \mu\text{m}$ would be approximately 5 times stronger than the $119\ \mu\text{m}$ line, while the $98.7\ \mu\text{m}$ line is not detected. Hence this possibility is ruled out. Similarly, if absorption in the $53\ \mu\text{m}$ line were responsible for the observed $119\ \mu\text{m}$ line flux, then the $163\ \mu\text{m}$ line would be about 5 times stronger than the $119\ \mu\text{m}$ line, which it is not. We can therefore conclude from the constraints provided by the other far-infrared OH lines that the $119\ \mu\text{m}$ emission line is not the result of radiative absorption and cascading. The implication is that OH excitation through collisions is more important in NGC 1068 than in the other observed galaxies and therefore that the gas responsible for the observed

emission in the 119 μm line resides predominantly in relatively dense and warm environments in comparison with these other sources.

The other two observed emission lines, unlike the 119 μm line, need not be collisionally dominated. In the case of the $\Pi_{1/2} 3/2 - 1/2$ 163 μm line, the most likely excitation mechanism is absorption of photons emitted by dust in the 53 and 35 μm lines followed by radiative cascade. The upper level of this transition is 270 K above the ground state (Fig. 5), so that excitation through collisions is expected to be ineffective in this line. The excitation mechanism of the $\Pi_{1/2} - \Pi_{3/2} 1/2 - 3/2$ 79 μm line could be a mixture of collisional and radiative pumping. The upper level of this transition is 182 K above the ground state, so that a warm and dense region could, at least partially, excite the line through collisions. Nevertheless, the line could be also excited through the same infrared pumping mechanism that results in the observed 163 μm line emission.

In conclusion, the 119 μm line is collisionally excited, whereas absorption of photons emitted by dust in the 53 and 35 μm lines probably dominates the excitation of the 163 μm line. The 79 μm OH line may in principle be excited through both mechanisms.

5.3. Constraints on the spatial origin of the 119 μm OH line

In NGC 1068 two regions with very different physical conditions can account for the observed OH emission as discussed above: the compact nuclear region, and the ring and bar where the starburst is taking place. A warm and dense region is required to account for the observed 119 μm line emission, given that the line is collisionally excited, so the warm and dense nuclear region around the AGN should be considered a good candidate, despite its small size ($\sim 5''$; e.g. Planesas et al. 1991; Schinnerer et al. 2000), for the following reasons:

- (i) It is warm: there are $\sim 10^3 M_{\odot}$ of hot H_2 (~ 2000 K) distributed over $\sim 5''$ (Blietz et al. 1994). From the CO (4-3) to (1-0) line intensity ratio, Tacconi et al. (1994) derive ~ 80 K for the bulk of the molecular gas, with a mass of $\sim 3 \times 10^7 M_{\odot}$ enclosed in within the central $4''$ (Helfer & Blitz 1995). Lutz et al. (2000) have reported the detection of pure H_2 rotational lines within the ISO-SWS aperture, and estimated $\sim 2.5 \times 10^7 M_{\odot}$ at ~ 200 K, but these lines may also arise, at least partially, from the inner regions of the 3 kpc starburst ring.
- (ii) The molecular clouds within the nuclear region are dense, although there is some dispersion in the values derived by several authors based on HCN emission: Tacconi et al. (1994) derived an H_2 density of $\sim 10^5 \text{ cm}^{-3}$, whereas subsequent observations and

analysis by Helfer & Blitz (1995) yielded a density of $\sim 4 \times 10^6 \text{ cm}^{-3}$. An intermediate density of $\sim 5 \times 10^5 \text{ cm}^{-3}$ from HCN and CS, and lower for other tracers, has been recently derived by Usero et al. (2004).

- (iii) The OH abundance is expected to reach high values in regions exposed to strong incident UV fields (PDRs, Sternberg & Dalgarno 1995), and in particular in X-ray dominated regions (XDRs, Lepp & Dalgarno 1996). The remarkable chemistry found by Usero et al. (2004) in the circumnuclear disk of NGC 1068 is indicative of an overall XDR and suggests a high OH abundance in the nuclear region.

Given that the OH 119 μm line is collisionally excited, the possibility that the line might arise from the nuclear region can be checked by computing the amount of warm gas required to account for the observed emission:

$$M_w(M_\odot) = 1.6 \times 10^7 \times \left[\frac{10^{-5}}{X(\text{OH})} \right] \times \left[\frac{5 \times 10^5 \text{ cm}^{-3}}{n(\text{H}_2)} \right] \times \left[\frac{4.3 \times 10^{-11} \text{ cm}^3 \text{ s}^{-1}}{\langle c_{lu} \rangle} \right], \quad (1)$$

where $X(\text{OH})$ is the OH abundance relative to H_2 , and $\langle c_{lu} \rangle$ is the collisional rate for excitation from the ground $\Pi_{3/2} 3/2$ level to the $\Pi_{3/2} 5/2$ one. Equation 1 assumes that, although the line could be optically thick, it is effectively optically thin, and makes use of the observed flux of $1.2 \times 10^{-12} \text{ erg s}^{-1} \text{ cm}^{-2}$. The reference value for the collisional rate, $\langle c_{lu} \rangle = 4.3 \times 10^{-11} \text{ cm}^3 \text{ s}^{-1}$, corresponds to gas at 80 K (Offer et al. 1994); it decreases by a factor of ≈ 2.7 for gas at 50 K and increases by a factor of 3 for gas at 200 K.

The reference OH abundance we use in this estimate, 10^{-5} , is the result of two separate studies: first, calculations of molecular abundances by Lepp & Dalgarno (1996) have shown that the OH abundance in XDRs is expected to be about two orders of magnitude higher than the abundance of HCN and HCO^+ . The authors in fact suggested the possibility that the high HCN/CO ratio observed in the nuclear region of NGC 1068 could be a consequence of enhanced X-ray ionization. Second, the possibility of a chemistry dominated by X-rays has found support from observations by Usero et al. (2004), who derive abundance ratios of HCN, HCO^+ , and CN in general agreement with predictions for XDRs. Since the HCN abundance derived by Usero et al. (2004) is $\sim 10^{-7}$, $X(\text{OH})$ in XDRs could attain values as high as 10^{-5} . On the other hand, the density of $5 \times 10^5 \text{ cm}^{-3}$ derived by Usero et al. (2004) has been adopted as the reference value in eq. 1. Finally, from the continuum models discussed in §3, the mass of gas we derive for the nuclear region is $\sim 2 \times 10^7 M_\odot$, similar to the value required in eq. 1. From these estimates we conclude that, if the OH abundance is as high as $\sim 10^{-5}$ (i.e. if the predictions for XDRs are applicable to the nuclear region of NGC 1068), the bulk of the OH 119 μm line could arise there. This possibility would naturally explain why NGC 1068 is unique in its 119 μm line emission among galaxies with full LWS spectra.

Finally we ask whether the OH 119 μm line could arise from an even more compact region, i.e., from a torus with a spatial scale of 1 pc surrounding the central AGN. According to typical parameters given by Krolik & Lepp (1989), a torus is expected to be hot ($\sim 10^3$ K), could have densities of 10^7 cm^{-3} , and therefore a mass of $\sim 10^5 M_\odot$. Also, the OH abundance is expected to be very high, $5 \times 10^{-5} - 10^{-4}$. Eq. 1 shows that the relatively low mass of the torus (about 2 orders of magnitude lower than the entire nucleus) could be compensated by the higher density, OH abundance, and temperature expected there, so that this possibility cannot be neglected.

The reference values for the nuclear abundance and density adopted in eq. 1 are rather uncertain (and possibly extreme). The continuum models of §3 indicate that the mass associated with the 32 K dust component, which is identified with the starburst ring, is $1.6 \times 10^9 M_\odot$. If $\sim 5\%$ of this mass corresponds to warm molecular gas rich in OH, the amount of extended warm gas is $\sim 8 \times 10^7 M_\odot$. According to eq. 1, the OH emission at 119 μm can then also be explained as arising in the ring if the associated PDRs, with assumed OH abundance of 2×10^{-6} (Sternberg & Dalgarno 1995; Goicoechea & Cernicharo 2002; González-Alfonso et al. 2004), have densities of a few $\times 10^5 \text{ cm}^{-3}$. Since Papadopoulos & Seaquist (1999b) found that most of the extended molecular gas resides in dense, compact clouds, this scenario seems also possible. However, the continuum from the starburst at 119 μm is strong, so that one expects that eq. 1 is in this case underestimating M_w , and the quoted physical parameters, $X(\text{OH})$ and $n(\text{H}_2)$, are lower limits. The effect of dust emission is discussed in detail below.

In conclusion, a definitive answer to the issue of the spatial origin of the OH 119 μm emission cannot be inferred from only the flux observed in the 119 μm line. Nevertheless, useful constraints on this subject are given: the line could be either explained as arising from the nucleus, with a required OH abundance $\sim 10^{-5}$, or from the extended ring, with OH abundance $> 2 \times 10^{-6}$ and density $>$ a few $\times 10^5 \text{ cm}^{-3}$. Nevertheless, the radiative transfer models described below, which take into account the effect of the continuum emission and the excitation of the 79 and 163 μm lines, point towards a nuclear origin of the OH emission.

5.4. Outline of the models

Analysis of the OH 79 and 163 μm lines requires the use of detailed radiative transfer calculations since, as pointed out above, the emission in these lines is expected to be strongly influenced by absorption of far-infrared continuum photons. We therefore proceeded to model the OH lines with two different codes, and confirmed that the results were in good agreement with each other. One of them, described in González-Alfonso & Cernicharo (1997, 1999),

has been recently used to model the far-infrared spectrum of Arp 220 (González-Alfonso et al. 2004), and the other is a Monte Carlo radiative transfer code used as part of a detailed study of all the OH lines observed by ISO in galaxies (Smith 2004; Smith et al. 2004). The latter was developed by the Submillimeter Wave Astronomy Satellite (SWAS) mission (Ashby et al. 2000), and is a modification of the original Bernes code. Both methods are non-local, non-LTE, assume spherical symmetry, and include a treatment of continuum photons from dust mixed in with the gas. Also, both codes take input as a series of concentric shells, each of which is assigned a size, gas and dust temperature, H₂ density, velocity and turbulent velocity width, and molecular abundance relative to H₂. The statistical equilibrium populations of OH in each spherical shell are computed by including the excitation by dust emission, excitation through collisions, and effects of line trapping. We ran two models to simulate the nucleus of the galaxy and the starburst extended ring, described in §5.4.1 and 5.4.2.

5.4.1. *Models for the nuclear emission: constraints on the spatial origin of the 79 and 163 μm OH lines*

We present models for the nuclear OH emission that *implicitly assume that the 119 μm emission line arises from the nuclear region*: $X(\text{OH}) = 10^{-5}$ is adopted, as well as densities $\sim 5 \times 10^5 \text{ cm}^{-3}$ for the bulk of the emitting gas. By assuming a pure nuclear origin for the 119 μm line, we check whether the other two OH lines could, in such a case, arise from the same nuclear region or require a more extended spatial origin.

The models use dust parameters derived from the nuclear dust model described in §3. The gas temperature is assumed to be equal to the dust temperature (Fig. 1b). In order to avoid overestimation of the continuum flux at the important wavelengths of 35 and 53 μm (see section 3), we have decreased the dust abundance by a factor of 2, so that the predicted flux in the 35–53 μm range is 40–50 Jy.

The H₂ densities derived from the dust model (i.e. a peak density of $\langle n_I(\text{H}_2) \rangle = 1.7 \times 10^3 \text{ cm}^{-3}$ at the inner radius) are not compatible with the densities inferred from different molecular tracers. This indicates that the medium is extremely clumped, as has been also argued elsewhere (e.g. Cameron et al. 1993; Tacconi et al. 1994). In order to account approximately for this clumpiness in our models, the following strategy is adopted: we use the “real” $n(\text{H}_2) \sim 5 \times 10^5 \text{ cm}^{-3}$ values for the bulk of the gas, and compute the volume filling factor $f_v = \langle n(\text{H}_2) \rangle / n(\text{H}_2)$, where the average value is that inferred from the dust model. The expected abundances of OH and the dust relative to H₂, $X(\text{OH})$ and $X(\text{dust})$, are then multiplied by f_v , so that the right OH and dust column densities are used

in the calculations together with the right density values. The same density profile r^{-1} that was used in the dust model is adopted, so that f_v is uniform throughout the nuclear region.

The modeled fluxes are convolved with the ISO-LWS grating resolution and are compared with the data in Fig. 6. Solid black lines show the results for the nuclear model that assumes $X(\text{OH})=10^{-5}$ and $f_v = 2.3 \times 10^{-5}$, the later value implying a density in the outer regions (where the bulk of the emission is generated) of $5 \times 10^5 \text{ cm}^{-3}$. The OH column density is $N(\text{OH}) = 2.7 \times 10^{17} \text{ cm}^{-2}$. Besides the 119 μm line, the model reproduces the emission in the 79 and 163 μm lines and is consistent with the upper limits given in Table 5.

We also checked the excitation mechanism of the other OH lines by generating an additional model with the same parameters as above except for the continuum emission, which is now turned off. In this model, therefore, the lines are excited exclusively through collisions with H_2 . The resulting flux of the 119 μm line remains unchanged when the dust emission is ignored, confirming that the line is collisionally excited. On the other hand, the flux densities of the 79 and 163 μm lines decrease in the “pure-collisional” model by factors of 2 and 5, respectively, showing that the emission in these lines is much more affected by radiative pumping. We conclude that, if the OH abundance in the nucleus were high enough to account for the collisionally excited 119 μm line, the observed fluxes in the 79 and 163 μm lines can also be explained as arising in the same nuclear region.

5.4.2. Models for the starburst emission

Two simple different approaches have been used to model the OH emission from the starburst. First, we have roughly modeled the whole starburst region as a spherical shell with external radius of 1.5 kpc, thickness of 0.3 kpc, and average H_2 density $\langle n_I(\text{H}_2) \rangle = 4.8 \text{ cm}^{-3}$, so that the corresponding continuum emission is reproduced with $T_d = 32 \text{ K}$ (section 3). As shown in section 5.3, the OH 119 μm emission requires densities of a few $\times 10^5 \text{ cm}^{-3}$, so that we have assumed a volume filling factor $f_v = 10^{-5}$ and therefore a “real” density $n(\text{H}_2) = 4.8 \times 10^5 \text{ cm}^{-3}$. The kinetic temperature is assumed to be $T_k = 100 \text{ K}$, and the OH abundance is $X(\text{OH}) = 2 \times 10^{-6} \times f_h$, where $f_h = 0.05$ is the assumed fraction of warm gas. The result of this model is shown in Fig. 6 (upper dotted lines). The 119 μm line is reproduced, but the flux densities of both the 79 μm and 163 μm lines are strongly underestimated. The reason is that the model implicitly assumes that the continuum emission, responsible for the excitation of those lines, arises from a very large volume, so that the *radiation density* is weak and has negligible effect on the line excitation.

Since the OH emission should arise from compact, discrete PDRs in the vicinity of O or

early B stars, where the continuum infrared radiation density is expected to be stronger than assumed above, we have also tried an alternative approach, which consists of modelling an individual “typical” cloud of the starburst. We first model the continuum from an individual cloud by assuming a central heating source and computing the dust equilibrium temperatures at each radial position that result from the balance of heating and cooling. The continuum model is adopted if (i) leaving aside a scaling factor (N_c , the number of clouds in the ensemble), the resulting SED is similar to that of the far-infrared emission of the starburst (i.e. the 32 K component found in section 3); the value of N_c is determined by requiring that the absolute continuum flux from the ensemble of clouds is equal to that observed for the 32 K component; and (ii) we require that the total mass of the ensemble does not exceed the mass inferred from the non-nuclear region ($< 4 \times 10^9 M_\odot$). Once the continuum is fitted, calculations for OH are performed by assuming $T_k = T_d$, and $X(\text{OH}) = 2 \times 10^{-6}$.

Several models with various density profiles were found to match the above two requirements. The common characteristic of all of them is the relatively high column density of the individual clouds, $N(\text{H}_2) > 10^{23} \text{ cm}^{-2}$, which is a consequence of the low effective dust temperature (32 K) of the SED. The results of the simplest model, characterized by a flat density profile, $n(\text{H}_2) = 5 \times 10^5 \text{ cm}^{-3}$, are given here for reference. With a radius of $5 \times 10^{17} \text{ cm}$, a stellar luminosity of $2 \times 10^4 L_\odot$, and $N_c = 4 \times 10^6$, the resulting SED is similar to that of the 32 K component (§3). For these clouds we obtain a total mass of $1.8 \times 10^9 M_\odot$. The predicted OH emission/absorption is shown in Fig. 6 (lower dashed lines). In spite of the relatively high density and temperatures (28-250 K) throughout the cloud, the 119 μm line is predicted to be too weak, and the 79 μm line is predicted in absorption. We have found this result quite general: in models where the OH abundance is high enough and the radiation density becomes strong enough to pump the 163 μm emission, the continuum at 79 and 119 μm is absorbed by OH and the predicted emission in the corresponding lines is reduced. Models that assume a density profile of r^{-1} generally predict the 119 μm line in absorption. In some models where the OH abundance was allowed to vary with radial position, the 79 μm line was predicted in emission but by far too weak to account for the observed flux density.

In conclusion, no starburst model is found to reproduce satisfactorily the emission observed in the three OH lines. If the local infrared radiation density is strong enough to pump the 163 μm line, the other two OH lines are expected to be weak or in absorption. Furthermore, the high density assumed for the starburst region would produce a relatively high HCN/CO intensity ratio, which is on the contrary ~ 0.01 in the spiral arms (Helfer & Blitz 1995). Finally, the PDR models described in 4.2 indicate a density of $1-1.5 \times 10^3 \text{ cm}^{-3}$, i.e. a density much lower than that required to account for the flux density of the OH 119 μm line. Therefore, and despite the simplicity of our models, taken together the analysis of

the OH lines and the derived PDR parameters indicate that the bulk of the OH emission arises from X-ray dominated nuclear regions.

6. CONCLUSIONS

The main results of this article can be summarized as follows:

- The complete far-infrared (50-200 μ m) spectrum of NGC 1068 has been observed for the first time. The 50-200 μ m continuum can be interpreted as thermal dust emission due to a nuclear component with a luminosity of $1.5 \times 10^{11} L_{\odot}$ illuminating a spherically symmetric dust envelope with inner and outer radii of 1 and 200 pc, respectively, and two additional components at temperatures of 20 and 32K, assuming a steep ($\beta=2$) dust emissivity law.
- The far-infrared ISO-LWS spectrum has been complemented with the mid-infrared data of ISO-SWS and with shorter wavelength (UV, optical and near-IR) data from the literature to assemble a composite atomic spectrum as complete as possible with the aim of modeling the different line emission components at work. This approach has been necessary especially because of the poor spatial resolution of the ISO spectrometers, which were not able to spatially separate the emission components. The lines have been interpreted as arising from two physically distinct components: the AGN component and a starburst component, the first one nuclear and the second one located in the ring at a radius of 15-16 " from the nucleus. The density and ionization parameter of the $\sim 5 \times 10^6$ year old starburst are found to be $n_H \sim 100 \text{ cm}^{-3}$ and $\log U = -3.5$, respectively. Three composite models have been computed with different AGN components: the first one has the ionizing continuum as derived from Alexander et al. (2000), showing a deep trough at energies of a few Rydberg; the second has the monotonically decreasing ionizing continuum given by Pier et al. (1994) and the third has a "big blue bump". Two values of the visual extinction ($E_{B-V} = 0.2$ and 0.4) have been adopted to correct the optical and ultraviolet line fluxes for the reddening. The agreement between the composite model with an AGN ionizing continuum characterized by the deep trough suggested by Alexander et al. (2000) is very satisfactory, taking into account both the simplicity of the photoionization models chosen to avoid dealing with too many free parameters and the large number of lines which originate in different physical regimes. The agreement between the observed spectrum and what is predicted using the canonical ionizing continuum is poorer, while the presence of a big blue bump is ruled out.

- The unique OH emission in the 119 μm line cannot be explained in terms of OH excitation through absorption of 35 and 53 μm photons emitted by dust, but rather it is collisionally excited. This indicates the presence of a warm and dense region with high OH abundance. A simple excitation analysis yields two main alternatives for the *spatial origin* of the observed 119 μm line emission: (i) the nuclear region, with $2 \times 10^7 M_{\odot}$ of warm gas (80 K), an average density of $n(\text{H}_2) = 5 \times 10^5 \text{ cm}^{-3}$, and an OH abundance of $\sim 10^{-5}$; (ii) the starburst region, if $\sim 5\%$ of the associated mass ($\sim 8 \times 10^7 M_{\odot}$) is warm (~ 100 K), dense (a few $\times 10^5 \text{ cm}^{-3}$), and rich in OH ($X(\text{OH}) \sim 2 \times 10^{-6}$).
- Radiative transfer models that simulate the emission/absorption in all the OH lines have been performed for both the nuclear and the starburst region. The models for the nucleus quantitatively account for the emission in the three OH lines if the nuclear physical conditions pointed out above are assumed. On the other hand, no starburst model is found to match the three OH lines simultaneously, because the strong far-infrared continuum tends to produce absorption, or to weaken the emission, in the OH 119 and 79 μm lines (as observed in other galaxies). Therefore, although some contribution from the extended starburst cannot be ruled out, our models indicate that the bulk of the OH emission arises in the nuclear region. The high nuclear OH abundance required to explain the emission strongly suggest a chemistry deeply influenced by X-rays, i.e., an *X-ray dominated region*.

The authors acknowledge the LWS Consortium, lead by Prof. Peter Clegg, for having built and operated the LWS instrument and solved many instrumental and data reduction problems. We also acknowledge discussions with Dr. Chris Dudley and thank him for reduction and analysis of the ISOCAM 6.2 μm image that we used in this work. The ESA staff at VILSPA (Villafranca, Spain) is also acknowledged for the ISO mission operational support. HAS acknowledges support from NASA Grant NAG5-10659; E.G-A would like to thank the Harvard-Smithsonian Center for Astrophysics for its hospitality while he was in residence during this research. JF acknowledges support from the NASA LTSA program and the Office of Naval Research.

REFERENCES

- Alexander, T., Lutz, D., Sturm, E., Genzel, R. et al. 2000, ApJ, 536, 710.
Alloin, D. et al. 2001, A&A, 369, L33.

- Ashby, M., et al. 2000, ApJ, 539, L119
- Bland-Hawthorn, J., et al., 1997, ApSS, 248, 9.
- Blietz, M., Cameron, M., Drapatz, S., Genzel, R. et al. 1994, ApJ, 421, 92.
- Bradford, C.M., et al., 1999, Proc.of the Conference "The Universe as seen by ISO", Paris, France, 20-23 October 1998 (ESA SP-427),p.861.
- Cameron, M., Storey, J.W.V., Rotaciuc, V., Genzel, R. et al. 1993, ApJ, 419, 136
- Clegg, P.E., et al. 1996, A&A, 315, L28.
- Colbert, J., et al., 1999, ApJ, 511, 721.
- Davies, R.I., Sugai,H., and Ward, M.J., 1998, MNRAS, 300, 388
- Draine, B. T. 1985, ApJSS, 57, 587.
- Ferland, G.J., 2000, RevMexAA,(Serie de Conferencias), Vol.9, 153
- Fischer, J., et al. 1999, Ap&SS, 266, 91.
- Goicoechea, J. R., Cernicharo, J. 2002, ApJ, 576, 77.
- González-Alfonso, E., & Cernicharo, J. 1997, A&A, 322, 938
- González-Alfonso, E., & Cernicharo, J. 1999, ApJ, 525, 845
- González-Alfonso, E., Smith, H.A., Fischer, J., Cernicharo, J. 2004, ApJ, 613, 247.
- Harvey, V.I., et al., 1999, Proc.of the Conference "The Universe as seen by ISO", Paris, France, 20-23 October 1998 (ESA SP-427), p.889.
- Helfer, T.T., Blitz, L., 1995, ApJ, 450, 90.
- Huchra, J.P., Vogeley, M.S. & Geller, M.J. 1999, ApJS, 121, 287.
- Kaufman, M.J., Wolfire, M.G., Hollenbach, D.J., Luhman, M.L. 1999, ApJ, 527, 795.
- Kessler, M.F. et al.,1996, A&A, 315, L27
- Kriss, G.A. et al. 1992, ApJ, 394, L37
- Krolik, J.H., & Lepp, S. 1989, ApJ, 347, 179
- Ivezic, Z., & Elitzur, M. 1997, MNRAS, 287, 799

- Le Floc'h, E., Mirabel, I.F., Laurent, O., Charmandaris, V. et al. 2001, *A&A*, 367, 487.
- Leitherer, C., et al. 1999, *ApJS*, 125, 489.
- Lepp, S., Dalgarno, A. 1996, *A&A*, 306, 21.
- Luhman, M.L. et al. 2003, *ApJ*, 594, 758.
- Lutz, D. et al., 2000, *ApJ*, 536, 697.
- Malhotra, S. et al. 2001, *ApJ*, 561, 766.
- Marconi, A., et al. 1996, *A&A*, 315, 335.
- Malkan, M. A. & Oke, J. B. 1983, *ApJ*, 265, 92.
- Offer, A.R., van Hemert, M.C., & van Dishoeck, E.F. 1994, *J. Chem. Phys.*, 100, 362.
- Papadopoulos, P.P. & Seaquist, E.R. 1999, *ApJ*, 514, L95.
- Papadopoulos, P.P. & Seaquist, E.R. 1999, *ApJ*, 516, 114.
- Pier, E.A., et al. 1994, *ApJ*, 428, 124.
- Planesas, P., Scoville, N., & Myers, S.T. 1991, *ApJ*, 369, 364.
- Preibisch, T., Ossenkopf, V., Yorke, H.W., Henning, T. 1993, *A&A*, 279, 577.
- Schinnerer, E., et al. 2000, *ApJ*, 533, 850.
- Smith, H.A. 2004, in "Second Workshop on New Concepts for Far Infrared and Submillimeter Space Astronomy", 7-8 March 2002, Univ. Maryland, College Park, Maryland, eds. D. Benford & D. Leisawitz, NASA/CP-2003-212233, p. 98.
- Smith, H. A., et al., 2004, in prep.
- Spinoglio, L., Andreani, P. & Malkan, M.A., 2002, *ApJ*, 572, 105.
- Spinoglio, L. & Malkan, M.A., 1992, *ApJ*, 399, 504.
- Scoville, N.Z., Matthews, K., Carico, D.P., Sanders, D.B. 1988, *ApJ*, 327, L61.
- Sternberg, A., Dalgarno, A. 1995, *ApJSS*, 99, 565.
- Sternberg, A., Genzel, R., Tacconi, L. 1994, *ApJ*, 436, 131.
- Swinyard, B.M., et al. 1996, *A&A*, 315, L43.

- Swinyard, B.M., et al. 1998, Proc. SPIE, A.M. Fowler (Ed.), Vol.3354, P.888.
- Tacconi, L. J., Genzel, R., Blietz, M., Cameron, M. et al. 1994, ApJ, 426, 77.
- Telesco, C.M., et al., 1984, ApJ, 282, 427.
- Thatte, N., et al. 1997, ApJ, 490, 238.
- Thompson, R.I., 1996, ApJ, 459, L61.
- Thronson, H.A. et al. 1989, ApJ, 343, 158.
- Usero, A., García-Burillo, S., Fuente, A., Martín-Pintado, J., Rodríguez-Fernández, N.J.
2004, A&A, 419, 897

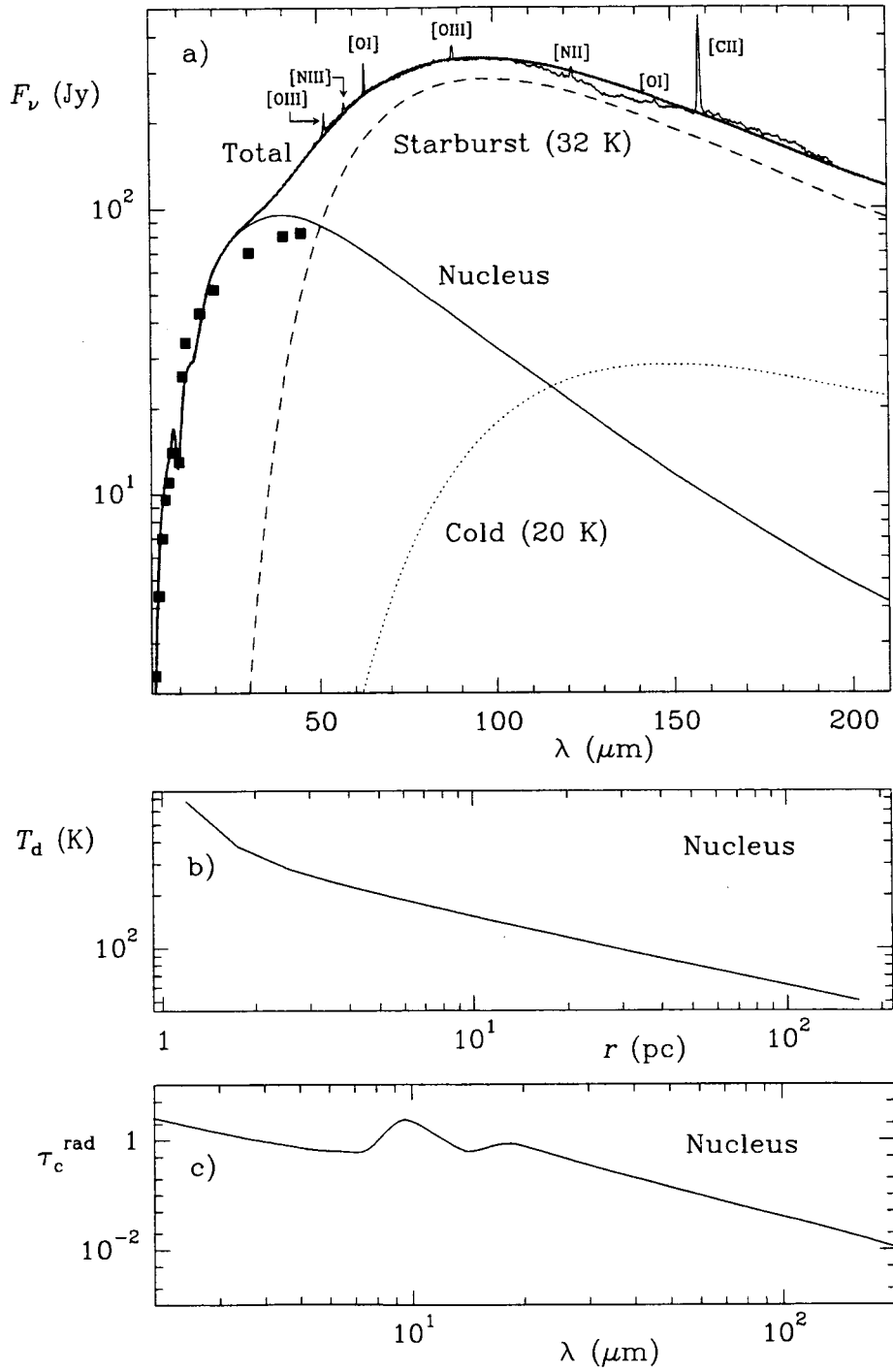


Fig. 1.— a) Spectral energy distribution of NGC 1068 and model fit. Three components, the nucleus, the starburst, and a cold component are used. b) and c) Dust temperature versus the radial position and radial continuum opacity versus wavelength for the nuclear region.

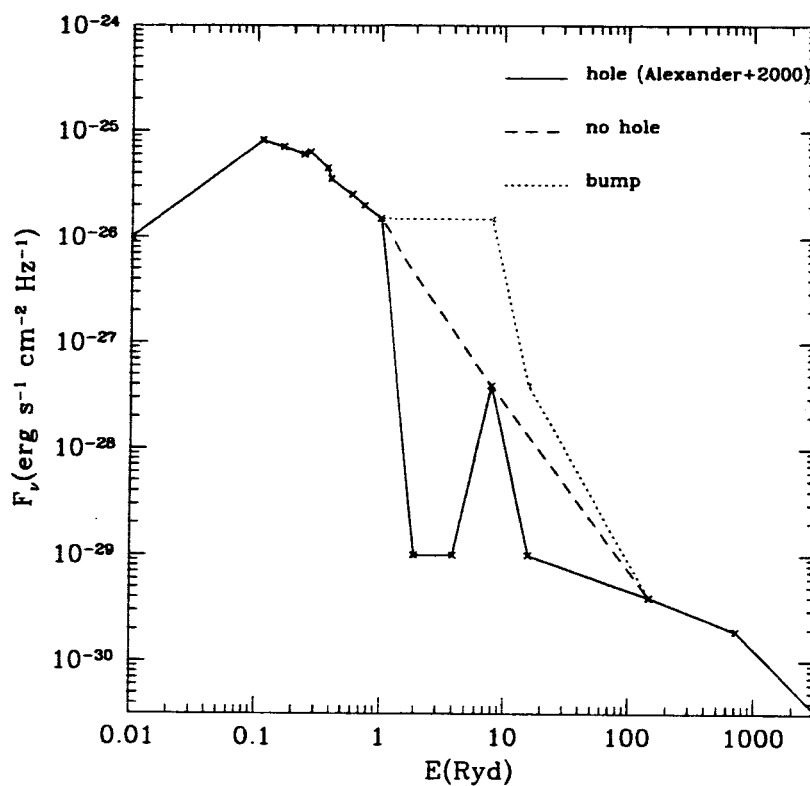


Fig. 2.— The AGN ionizing continua used as input for the photoionization models of NGC 1068. The three continua differ in the frequency region between $1 > E_{\text{Ryd}} > 100$, while outside this region the Pier et al. (1994) spectrum was adopted. The solid line shows the continuum derived from Alexander et al. (2000); the dashed line shows a simple power law interpolation; the dotted line shows the presence of the predicted "big blue bump".

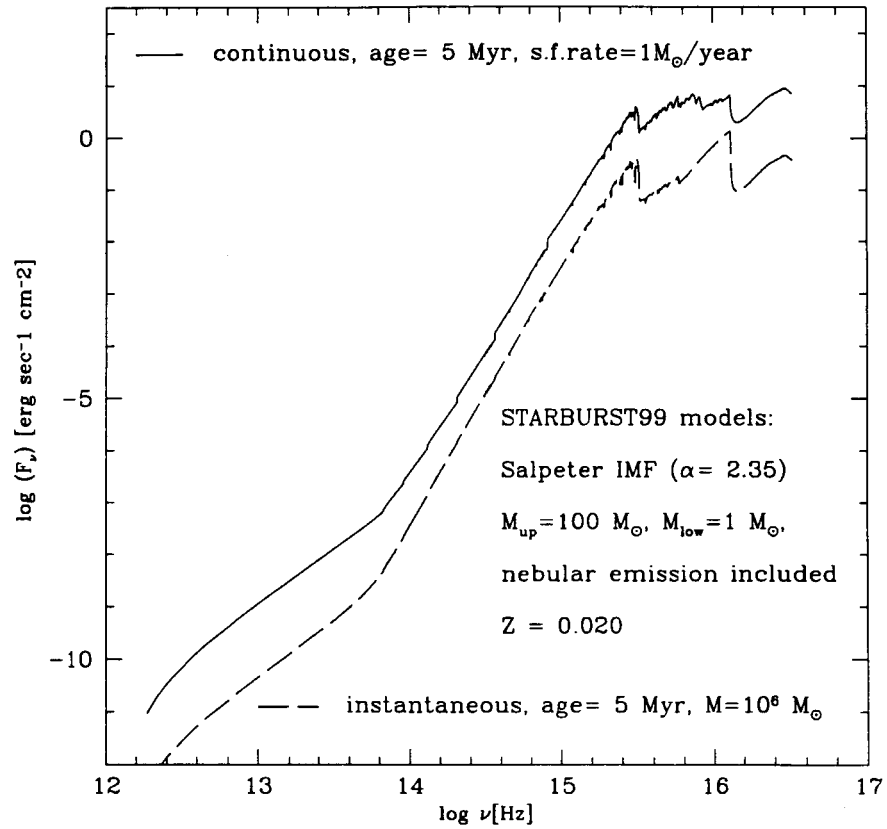


Fig. 3.— The starburst ring ionizing continua used as input for the photoionization models of NGC 1068. The two continua are taken from Leitherer et al. (1999) and represent a continuous starburst model (solid line) and an instantaneous model (broken line), both with 5 Myr of age.

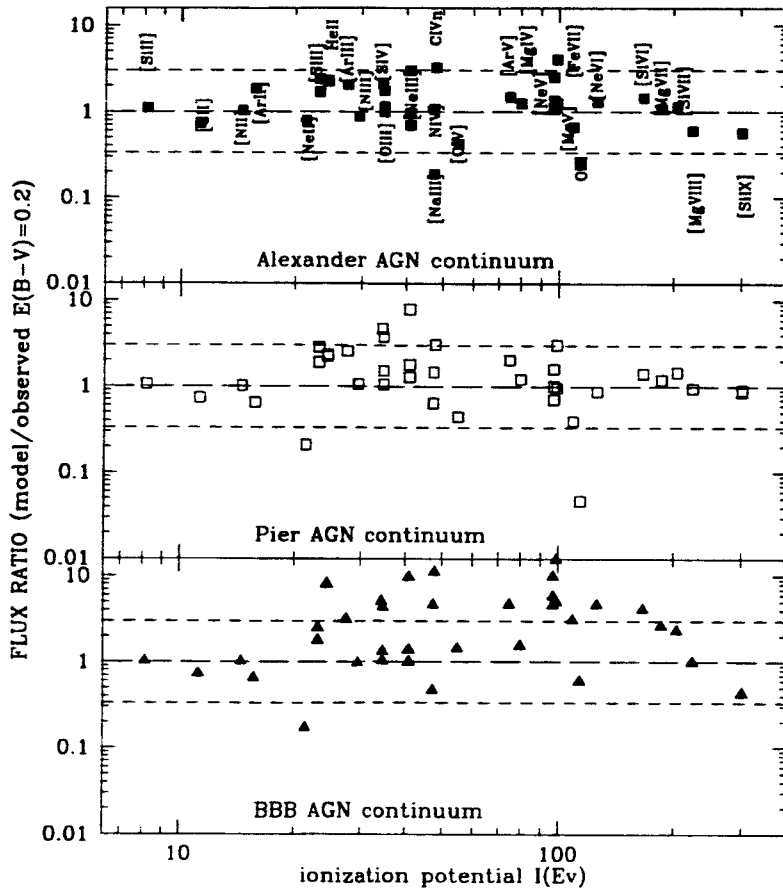


Fig. 4.— The comparison of the composite models with the observations is shown as the ratio of modeled to observed flux ratio for each line, with the ionization potential in the x-axis. The assumed reddening is $E(B-V)=0.2$. Panels from top to bottom: model CM1, CM2 and CM3. The short dashed lines represent flux ratios within a factor 3 either ways.

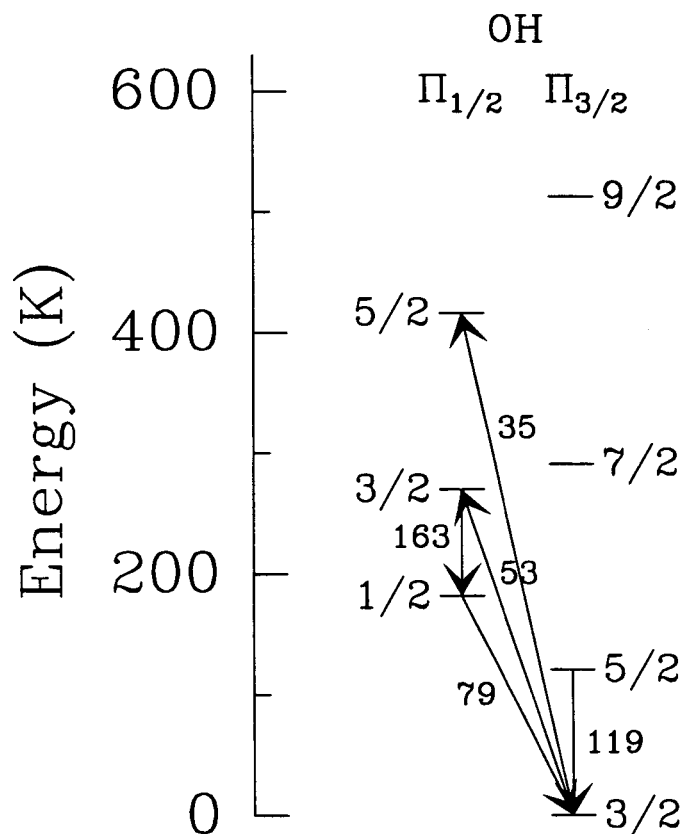


Fig. 5.— Energy level diagram of OH. Rotational levels with energies up to 600 K are shown; the three lines detected in NGC 1068 are indicated with arrows, as well as the 35 and 53 μm lines that could play an important role in the radiative excitation. The wavelengths are indicated in μm . Λ -doubling is ignored because the Λ -doublets are not resolved with the ISO grating resolution.

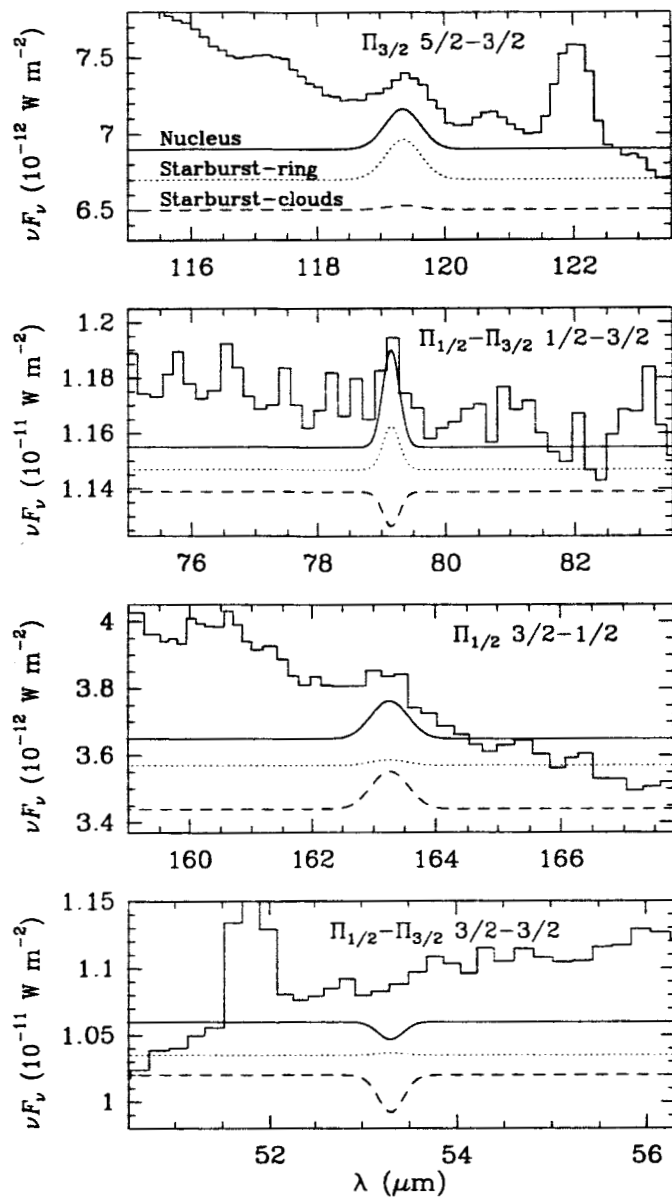


Fig. 6.— Comparison between the observed OH lines and model results. As indicated in the upper panel, the upper modeled spectrum (solid lines) corresponds to the model for the nucleus, the middle one (dotted lines) corresponds to the starburst modelled as a whole, and the lower one (dashed lines) corresponds to the starburst modelled as an ensemble of individual clouds (see text for details).

Table 1. Measured line fluxes from the LWS and SWS grating spectra, with 1σ uncertainties.

Line	λ (μm)	Flux ($10^{-13} \text{ erg s}^{-1} \text{ cm}^{-2}$)	Aperture ($''^2$)	reference
[Si IX] $^3P_2 \rightarrow ^3P_1$	2.584	3.0	14×20	1
[Mg VIII] $^2P_{3/2} \rightarrow ^2P_{1/2}$	3.028	$11. \pm 1.1$	14×20	1
[Si IX] $^3P_1 \rightarrow ^3P_0$	3.936	5.0 ± 0.6	14×20	1
[Mg IV] $^2P_{1/2} \rightarrow ^2P_{3/2}$	4.487	7.6 ± 1.5	14×20	1
[Ar VI] $^2P_{3/2} \rightarrow ^2P_{1/2}$	4.529	$15. \pm 3.$	14×20	1
[Fe II] $^4F_{9/2} \rightarrow ^6D_{9/2}$	5.340	5.0	14×20	1
[Mg VII] $^3P_2 \rightarrow ^3P_1$	5.503	13.	14×20	1
[Mg V] $^3P_1 \rightarrow ^3P_2$	5.610	$18. \pm 2.$	14×20	1
[Ar II] $^2P_{1/2} \rightarrow ^2P_{3/2}$	6.985	13.	14×20	1
[Na III] $^2P_{1/2} \rightarrow ^2P_{3/2}$	7.318	5.8	14×20	1
[Ne VI] $^2P_{3/2} \rightarrow ^2P_{1/2}$	7.652	$110. \pm 11.$	14×20	1
[Fe VII] $^3F_4 \rightarrow ^3F_3$	7.815	3.0	14×20	1
[Ar V] $^3P_2 \rightarrow ^3P_1$	7.902	$< 12.$	14×20	1
[Na VI] $^3P_2 \rightarrow ^3P_1$	8.611	$< 16.$	14×20	1
[Ar III] $^3P_1 \rightarrow ^3P_2$	8.991	23.0 ± 3.3	14×20	1
[Fe VII] $^3F_3 \rightarrow ^3F_2$	9.527	4.0	14×20	1
[S IV] $^2P_{3/2} \rightarrow ^2P_{1/2}$	10.510	$58. \pm 6.$	14×20	1
[Ne II] $^2P_{3/2} \rightarrow ^2P_{1/2}$	12.813	70.	14×27	1
[Ar V] $^3P_1 \rightarrow ^3P_0$	13.102	$< 16.$	14×27	1
[Ne V] $^3P_2 \rightarrow ^3P_1$	14.322	$97. \pm 9.7$	14×27	1
[Ne III] $^3P_1 \rightarrow ^3P_2$	15.555	$160. \pm 32.$	14×27	1
[Fe II] $^4F_{7/2} \rightarrow ^4F_{9/2}$	17.936	$< 10.$	14×27	1
[S III] $^3P_2 \rightarrow ^3P_1$	18.713	40.	14×27	1
[Ne V] $^3P_1 \rightarrow ^3P_0$	24.317	$70. \pm 7.$	14×27	1
[O IV] $^2P_{3/2} \rightarrow ^2P_{1/2}$	25.890	$190. \pm 20.$	14×27	1
[Fe II] $^6D_{7/2} \rightarrow ^6D_{9/2}$	25.988	8.	14×27	1
[S III] $^3P_1 \rightarrow ^3P_0$	33.481	55.	20×33	1
[Si II] $^2P_{3/2} \rightarrow ^2P_{1/2}$	34.814	91.	20×33	1
[Ne III] $^3P_0 \rightarrow ^3P_1$	36.013	18.	20×33	1
[O III] $^3P_2 \rightarrow ^3P_1$	51.814	$114. \pm 3.$	80	2
[N III] $^2P_{3/2} \rightarrow ^2P_{1/2}$	57.317	51.4 ± 2.5	80	2
[O I] $^3P_1 \rightarrow ^3P_2$	63.184	$156. \pm 1.$	80	2
[O III] $^3P_1 \rightarrow ^3P_0$	88.356	$111. \pm 1.$	80	2
[N II] $^3P_2 \rightarrow ^3P_1$	121.897	30.5 ± 1.1	80	2
[O I] $^3P_0 \rightarrow ^3P_1$	145.525	11.9 ± 0.4	80	2
[C II] $^2P_{3/2} \rightarrow ^2P_{1/2}$	157.741	$216. \pm 1.$	80	2
OH $^2\Pi_{1/2}5/2-^2\Pi_{3/2}3/2$	34.60/34.63	$< 3.$	20×33	2
OH $^2\Pi_{1/2}1/2-^2\Pi_{1/2}3/2$	79.11/79.18	14.4 ± 1.5	80	2
OH $^2\Pi_{3/2}5/2-^2\Pi_{3/2}3/2$	119.23/119.44	11.9 ± 1.2	80	2
OH $^2\Pi_{1/2}3/2-^2\Pi_{1/2}1/2$	163.12/163.40	7.42 ± 0.65	80	2

Note. — (1): from Lutz et al. (2000) and, where errors are available, Alexander et al. (2000); (2): this work

Table 2. Comparison of observed line fluxes with AGN model predictions

Line id. λ (μm)	Observed/ D^1 / D^2	Flux (10^{-13} erg s $^{-1}$ cm $^{-2}$)					
		AGN A model ³		AGN B model ⁴		AGN C model ⁵	
		Comp. 1	Comp. 2	Comp. 1	Comp. 2	Comp. 1	Comp. 2
O VI λ .1032+.1037	37.4/4334./402.	62.5+33.2	1.5+1.4	12.1+6.4	0.24+0.20	155.+80.	3.2+1.7
(Ly α) _n λ .1215	101.8/3562./602	2806.	1737.	2951.	1828.	3388.	2182.
N IV] λ .1487	5.1/103./22.9	20.0	4.6	28.6	5.0	67.7	38.5
(CIV) _n λ .1549	39.7/790./177.	488.	78.5	462.	83.2	1345.	620.
HeII λ .1640	21.4/426./95.5	96.6	66.5	96.4	67.3	422.	290.
[Ne V] λ .3426	15.7/95./38.7	79.6	17.0	56.2	5.9	288.	94.
[Ne III] λ .3869+.3968	19.2/97./43.2	38.0+11.4	29.8+9.0	145.8+43.9	88.7+26.7	162.+49.	130.+39.
HeII λ .4686	6.1/27.6/13.	13.1	9.6	13.4	9.8	57.8	41.3
[O III] λ .4959+.5007	256./964./496	115.6+334.1	81.3+235	290.+837.	169.+486.	300.+867.	229.+661.
[Si VI] λ 1.96	8.0/9.2/8.6	10.41	2.0	9.7	2.5	30.4	4.8
[Si VII] λ 2.48	8.3	9.38	0.2	11.8	.36	19.0	0.4
[Si IX] λ 2.584	3.0	1.70	...	2.6	...	1.3	—
[Mg VIII] λ 3.028	11.	6.64	...	10.5	...	11.	—
[Si IX] λ 3.936	5.4	3.10	...	4.9	...	2.3	—
[Mg IV] λ 4.487	7.6	3.21	6.2	3.5	5.8	11.2	0.5
[Ar VI] λ 4.529	15.	14.9	7.3	24.1	6.6	39.2	31.
[Mg VII] λ 5.503	13.	13.9	0.23	15.6	.14	33.2	0.8
[Mg V] λ 5.610	18.	5.62	6.31	4.0	3.1	31.6	23.9
[Ar II] λ 6.985	13.	6.87	13.4	1.3	3.1	1.4	3.1
[Na III] λ 7.318	5.8	0.66	0.45	2.2	1.4	1.5	1.1
[Ne VI] λ 7.652	110.	134.	8.8	93.7	2.6	455.	54.
[Fe VII] λ 7.815	3.0	1.92	1.90	1.9	1.0	8.6	6.4
[Ar V] λ 7.902	< 12.	2.90	1.91	3.3	2.5	4.5	7.0
[Na VI] λ 8.611	< 16.	1.10	0.18	0.8	.08	3.8	0.8
[Ar III] + [Mg VII] λ 8.991	25.	17.8+17.	9.0+0.36	18.2+19.4	19.+19	16.+40.	15.3+1.0
[Fe VII] λ 9.527	4.0	7.96	8.2	7.7	4.5	35.3	26.8
[S IV] λ 10.510	58.	76.5	43.6	155.	117.	133.	161.
[Ne II] λ 12.813	70.	24.8	23.9	2.9	6.0	1.9	4.3
[Ar V] λ 13.102	< 16.	2.94	2.86	3.4	3.7	4.7	10.3
[Ne V] λ 14.322	97.	79.2	50.7	74.6	23.7	332.	232.
[Ne III] λ 15.555	160.	68.1	37.6	136.7	104.	91.4	79.6
[S III] λ 18.713	40.	33.7	41.5	31.5	61.9	28.2	51.3
[Ne V] λ 24.317	70.	34.8	39.8	31.2	18.2	139.	182.
[O IV] λ 25.890	190.	22.2	55.4	25.6	57.5	69.6	200.
[S III] λ 33.481	55.	8.59	26.3	7.7	38.1	6.7	33.1
[Si II] λ 34.814	91.	11.2	39.5	8.6	38.5	5.9	37.1
[Ne III] λ 36.013	18.	4.97	3.2	10.2	8.8	6.9	6.8
[O III] λ 51.814	110.	19.2	27.3	28.2	59.5	19.8	44.7
[N III] λ 57.317	51.	4.64	8.7	4.9	17.4	3.7	14.4
[O I] λ 63.184	156.	2.50	3.6	1.5	3.7	0.9	3.8
[O III] λ 88.356	110.	2.53	6.5	3.8	14.2	2.6	11.3
[N II] λ 121.897	30.	0.13	0.86	.06	.40	.08	0.5
[O I] λ 145.525	12.	0.16	0.28	.09	.29	.05	0.3
[C II] λ 157.741	220.	0.46	3.1	.29	2.2	.11	1.8

Table 2—Continued

Line id. λ (μm)	Observed/ D^1 / D^2	Flux (10^{-13} erg s $^{-1}$ cm $^{-2}$)				AGN C model ⁵	
		AGN A model ³		AGN B model ⁴		Comp. 1	Comp. 2
		Comp. 1	Comp. 2	Comp. 1	Comp. 2	Comp. 1	Comp. 2

¹Dereddened line flux, assuming $E_{B-V} = 0.4$

²Dereddened line flux, assuming $E_{B-V} = 0.2$

³AGN A parameters: component 1: Log U=-1., Log n=4, internal radius $\simeq 21$ pc, external radius $\simeq 109$ pc, ionizing spectrum from Alexander et al. (2000); component 2: Log U=-2., Log n=3.3, internal radius $\simeq 153$ pc, external radius $\simeq 362$ pc, ionizing spectrum from Alexander et al. (2000).

⁴AGN B parameters: same as AGN A models, but with the ionizing spectrum from Pier et al. (1994)

⁵AGN C parameters: same as AGN A models, but with the ionizing spectrum that includes a big blue bump (see text)

Table 3. Comparison of observed line fluxes with the Ring Starburst model predictions

Line id.λ (μm)	Observed	Flux (10^{-13} erg s $^{-1}$ cm $^{-2}$)					
		SBR A ¹	SBR B ²	SBR C ³	SBRD ⁴	SBR E ⁵	SBR F ⁶
O VI λ .1032+.1037	37.4/4334./402.	—	—	—	—	—	—
(Lyα) _n λ .1215	101.8/3562./602	221.	36.3	284.	400.	1135.	1424.
N IV] λ .1487	5.1/103./22.9	22.8	0.02	41.8	0.02	177.	0.08
(CIV) _n λ .1549	39.7/790./177.	162.	0.39	277.	.75	1154.	1.80
HeII λ .1640	21.4/426./95.5	235.	38.9	373.	47.8	1466.	161.
[Ne V] λ .3426	15.7/95./38.7	16.2	—	30.9	—	125.	—
[Ne III] λ .3869+.3968	19.2/97./43.2	106.+32.	24.6+7.4	165+49.7	30.4+9.2	659+199	105+31.6
HeII λ .4686	6.1/27.6/13.	33.5	5.8	53.1	7.1	207.	23.8
[O III] λ .4959+.5007	256./964./496	439+1269	19.8+57.	720+2077	24.6+71.2	2882+8307	85.8+247.
[Si VI] λ 1.96	8.0/9.2/8.6	—	—	—	—	—	—
[Si VII] λ 2.48	8.3	—	—	—	—	—	—
[Si IX] λ 2.584	3.0	—	—	—	—	—	—
[Mg VIII] λ 3.028	11.	—	—	—	—	—	—
[Si IX] λ 3.936	5.4	—	—	—	—	—	—
[Mg IV] λ 4.487	7.6	1.0	—	1.7	—	6.6	—
[Ar VI] λ 4.529	15.	1.7	—	3.3	—	13.3	—
[Mg VII] λ 5.503	13.	—	—	—	—	—	—
[Mg V] λ 5.610	18.	0.84	—	1.6	—	6.2	—
[Ar II] λ 6.985	13.	2.6	3.3	3.1	4.0	11.7	13.6
[Na III] λ 7.318	5.8	0.2	0.09	0.3	0.1	1.2	0.4
[Ne VI] λ 7.652	110.	4.5	—	8.0	—	35.	—
[Fe VII] λ 7.815	3.0	0.13	—	0.3	—	1.2	—
[Ar V] λ 7.902	< 12.	1.9	—	4.0	—	15.6	—
[Na VI] λ 8.611	< 16.	—	—	—	—	—	—
[Ar III] + [Mg VII] λ 8.991	25.	16.	5.6	23.	6.9	89.7	23.1
[Fe VII] λ 9.527	4.0	0.6	—	1.1	—	4.3	—
[S IV] λ 10.510	58.	91.	0.6	157.	0.8	589.	2.4
[Ne II] λ 12.813	70.	3.3	4.9	3.9	5.8	15.2	20.4
[Ar V] λ 13.102	< 16.	5.7	—	10.6	—	41.4	—
[Ne V] λ 14.322	97.	74.4	—	134.	—	524.	—
[Ne III] λ 15.555	160.	97.3	40.3	143.	48.7	552.	163.
[S III] λ 18.713	40.	65.3	1.6	99.	20.3	386.	69.
[Ne V] λ 24.317	70.	83.6	—	148.	—	490.	—
[O IV] λ 25.890	190.	496.	1.4	828.	1.7	2615	4.7
[S III] λ 33.481	55.	199.	51.	279.	58.4	649.	125.
[Si II] λ 34.814	91.	45.8	45.	53.	49.3	105.	100.
[Ne III] λ 36.013	18.	17.4	6.9	26.	4.3	97.	28.
[O III] λ 51.814	110.	921.	62.	1559.	80.4	4800.	222.
[N III] λ 57.317	51.	349.	30.	468.	31.8	750.	44.4
[O I] λ 63.184	156.	65.	99.	77.	120.	300.	383.
[O III] λ 88.356	110.	1539.	105.	1812.	99.5	1830.	90.
[N II] λ 121.897	30.	30.*	30*	30.*	30.*	30.*	30.*
[O I] λ 145.525	12.	6.5	10.	7.7	12.	27.	36.
[C II] λ 157.741	220.	294.	377.	130.	158.	1440.	145.

Note. — *: this line was used for normalization

¹SBR A parameters: Log U=-2.5, Log n=1.0, ionizing spectrum from Starburst99 with instantaneous star-formation law, $M = 10^6 M_{\odot}$, IMF: $=2.35 M_{up} = 100 M_{\odot}$, $M_{low} = 1 M_{\odot}$, nebular emission included, $Z=0.020$, age of 5 Myr. The integration was stopped at a temperature of 50K, the adopted abundances are those relative to HII regions and grain emission is included.

²SBR B parameters: Log U=-3.5, Log n=1.0, all other parameters as for SBR A.

³SBR C parameters: Log U=-2.5, Log n=2.0, all other parameters as for SBR A.

⁴SBR D parameters: Log U=-3.5, Log n=2.0, all other parameters as for SBR A.

⁵SBR E parameters: Log U=-2.5, Log n=3.0, all other parameters as for SBR A.

⁶SBR F parameters: Log U=-3.5, Log n=3.0, all other parameters as for SBR A.

Table 4. Comparison of observed line fluxes with composite model predictions

Line id.λ (μm)	Flux (10^{-13} erg s $^{-1}$ cm $^{-2}$)				
	Observed/D ¹	/D ²	CM1 ³	CM2 ⁴	CM3 ⁵
O VI λ .1032+.1037	37.4/4334.	/402.	98.6	18.9	240.
(Lyα) _n λ .1215	101.8/3562.	/602	4943.	5179	5970.
N IV] λ .1487	5.1/103./	/22.9	24.6	33.8	106.2
(CIV) _n λ .1549	39.7/790./	/177.	567.	546	1967.
HeII λ .1640	21.4/426./	/95.5	211.	211.5	761.
[Ne V] λ .3426	15.7/95./	/38.7	96.6	62.1	382.
[Ne III] λ .3869+.3968	19.2/97./	/43.2	127.8	344.7	420.
HeII λ .4686	6.1/27.6/	/13.	29.8	30.3	106.2
[O III] λ .4959+.5007	256./964./	/496	861.8	1879	2153.
[Si VI] λ 1.96	8.0/9.2/	/8.6	12.4	12.2	35.2
[Si VII] λ 2.48	8.3		9.6	12.2	19.4
[Si IX] λ 2.584	3.0		1.7	2.6	1.3
[Mg VIII] λ 3.028	11.		6.6	10.5	11.
[Si IX] λ 3.936	5.4		3.1	4.9	2.3
[Mg IV] λ 4.487	7.6		9.4	9.3	11.7
[Ar VI] λ 4.529	15.		22.	30.7	70.2
[Mg VII] λ 5.503	13.		14.	15.7	34.
[Mg V] λ 5.610	18.		12.	7.1	55.5
[Ar II] λ 6.985	13.		24.	8.4	8.5
[Na III] λ 7.318	5.8		1.1	3.7	2.7
[Ne VI] λ 7.652	110.		143	96.3	509.
[Fe VII] λ 7.815	3.0		3.8	2.9	15.
[Ar V] λ 7.902	< 12.		4.8	5.8	11.5
[Na VI] λ 8.611	< 16.		1.3	0.9	4.6
[Ar III] + [Mg VII] λ 8.991	25.		51.	64.1	79.2
[Fe VII] λ 9.527	4.0		16.	12.2	62.1
[S IV] λ 10.510	58.		121	273.	295.
[Ne II] λ 12.813	70.		55.	14.7	12.
[Ar V] λ 13.102	< 16.		5.8	7.1	15.
[Ne V] λ 14.322	97.		130.	98.3	564.
[Ne III] λ 15.555	160.		155.	289.4	220.
[S III] λ 18.713	40.		95.	113.7	99.8
[Ne V] λ 24.317	70.		75.	49.4	321.
[O IV] λ 25.890	190.		80.	84.8	272.
[S III] λ 33.481	55.		93.	104.2	98.2
[Si II] λ 34.814	91.		100.	96.4	92.3
[Ne III] λ 36.013	18.		12.5	23.3	18.
[O III] λ 51.814	110.		127	168.1	145.
[N III] λ 57.317	51.		45.	54.1	50.
[O I] λ 63.184	156.		126.	125.2	125.
[O III] λ 88.356	110.		109.	117.5	113.
[N II] λ 121.897	30.		31.	30.5	30.6
[O I] λ 145.525	12.		12.4	12.4	12.3
[C II] λ 157.741	220.		161	160.4	160.

¹Dereddened line flux, assuming $E_{B-V} = 0.4$

²Dereddened line flux, assuming $E_{B-V} = 0.2$

³CM1 = AGN A + SBR D

⁴CM2 = AGN B + SBR D

⁵CM3 = AGN C + SBR D

Table 5. Comparison of observed line fluxes with model predictions for the nuclear region

Line id. λ	Flux (10^{-12} <i>erg s</i> ⁻¹ <i>cm</i> ⁻²)		Notes
	Observed	Modeled	
34 μ m	< 0.1	-0.70	(absorption)
53 μ m	< 1.2	-0.84	(absorption)
79 μ m	1.44	1.46	
84 μ m	< 1.2	0.16	
98 μ m	< 1.2	0.31	
119 μ m	1.19	1.52	
163 μ m	0.74	0.51	

The far-infrared spectrum of Arp 220¹

Eduardo González-Alfonso^{1,2}

*Universidad de Alcalá de Henares, Departamento de Física, Campus Universitario,
E-28871 Alcalá de Henares, Madrid, Spain*

eduardo.gonzalez@uah.es

Howard A. Smith

Harvard-Smithsonian Center for Astrophysics, 60 Garden Street, Cambridge, MA 02138

hsmith@cfa.harvard.edu

Jacqueline Fischer

Naval Research Laboratory, Remote Sensing Division, Code 7213, Washington, DC 20375

jackie.fischer@nrl.navy.mil

and

José Cernicharo

CSIC, IEM, Dpto. Astrofísica Molecular e Infrarroja, Serrano 123, E-28006 Madrid, Spain

cerni@damir.iem.csic.es

ABSTRACT

ISO/LWS grating observations of the ultraluminous infrared galaxy Arp 220 shows absorption in molecular lines of OH, H₂O, CH, NH, and NH₃, as well as in the [O I] 63 μ m line and emission in the [C II] 158 μ m line. We have modeled the continuum and the emission/absorption of all observed features by means of a non-local radiative transfer code. The continuum from 25 to 1300 μ m is modeled as a warm (106 K) nuclear region that is optically thick in the

¹Visiting Astronomer, Harvard-Smithsonian Center for Astrophysics, 60 Garden Street, Cambridge, MA 02138.

²CSIC, IEM, Dpto. Astrofísica Molecular e Infrarroja, Serrano 123, E-28006 Madrid, Spain.

far-infrared, attenuated by an extended region (size $2''$) that is heated mainly through absorption of nuclear infrared radiation. The molecular absorption in the nuclear region is characterized by high excitation due to the high infrared radiation density. The OH column densities are high toward the nucleus ($2 - 6 \times 10^{17} \text{ cm}^{-2}$) and the extended region ($\sim 2 \times 10^{17} \text{ cm}^{-2}$). The H_2O column density is also high toward the nucleus ($2 - 10 \times 10^{17} \text{ cm}^{-2}$) and lower in the extended region. The column densities in a halo that accounts for the absorption by the lowest lying levels are similar to what are found in the diffuse clouds toward the star forming regions in the Sgr B2 molecular cloud complex near the Galactic Center. Most notable are the high column densities found for NH and NH_3 toward the nucleus, with values of $\sim 1.5 \times 10^{16} \text{ cm}^{-2}$ and $\sim 3 \times 10^{16} \text{ cm}^{-2}$, respectively, whereas the NH_2 column density is lower than $\sim 2 \times 10^{15} \text{ cm}^{-2}$. A combination of PDRs in the extended region and hot cores with enhanced H_2O photodissociation and a possible shock contribution in the nuclei may explain the relative column densities of OH and H_2O , whereas the nitrogen chemistry may be strongly affected by cosmic ray ionization. The [C II] $158 \mu\text{m}$ line is well reproduced by our models and its "deficit" relative to the CII/FIR ratio in normal and starburst galaxies is suggested to be mainly a consequence of the dominant non-PDR component of far-infrared radiation, although our models alone cannot rule out extinction effects in the nuclei.

Subject headings: galaxies: abundances — galaxies: individual (Arp 220) — galaxies: ISM — galaxies: starburst — infrared: galaxies — radiative transfer

1. Introduction

With a redshift of $z = 0.018$, Arp 220 (IC 4553/4) is the nearest and one of the best studied ultraluminous infrared galaxies (ULIRGs). The tails observed in the optical, together with the double highly-obscured and compact ($0''.3$) nuclei observed in the near and mid-infrared, as well as in the millimeter, strongly suggest that the enormous luminosity of Arp 220, $\sim 10^{12} L_\odot$, is the result of galactic merging. Nevertheless, the concrete physical process responsible is still a matter of debate: the proposed sources are hidden active nuclei and/or bursts of star formation.

¹Based on observations with the Infrared Space Observatory, an ESA project with instruments funded by ESA Member States (especially the principal investigator countries: France, Germany, Netherlands, and the United Kingdom) and with the participation of ISAS and NASA.

Molecular observations of Arp 220 provide unique clues to the physical and chemical processes occurring in the nuclei and their surroundings. In the millimeter region, CO observations have been carried out with increasingly high angular resolution (Radford, Solomon, & Downes 1991; Scoville et al. 1991; Okumura et al. 1994; Scoville, Yun, & Bryant 1997; Sakamoto et al. 1999). In particular they have shown that, on the one hand, CO emission arises from a region significantly more extended than the nuclei ($\sim 3 - 4''$), and on the other hand that the CO(2-1) to CO(1-0) intensity ratio is lower than 1, thus suggesting that CO mainly traces low density regions ($< 10^3 \text{ cm}^{-3}$). Observations of molecules with high dipole moment, like CS and HCN, have revealed that the fraction of molecular gas contained in dense clouds ($n(\text{H}_2) \geq 10^4 \text{ cm}^{-3}$) is much larger than in normal galaxies, yielding $\sim 10^{10} M_\odot$ of dense gas (Solomon, Radford, & Downes 1990; Solomon, Downes, & Radford 1992). Radford et al. (1991b) found that HCN(1-0) and $\text{HCO}^+(1-0)$ peak strongly toward the nuclei, but also show low-level extended emission. More recently, Aalto et al. (2002) have detected emission from the high density tracers HNC and CN, and the relatively low HCN/CN and HCN/HNC intensity ratios were attributed to widespread PDR chemistry.

The launch of the Infrared Space Observatory (ISO) opened a new window for the study of the physical and chemical properties of ultraluminous infrared galaxies. Despite the lack of angular and spectral resolution, the observations of Arp 220's far-infrared spectrum from 40 to 200 μm (Fischer et al. 1997, 1999) and of a number of individual lines in the SWS range (Sturm et al. 1996) provided new insights in our understanding of the ionic, atomic and molecular content of the galaxy. These wavelength regions are of great interest, because the bulk of the enormous luminosity is emitted in the far-infrared, and also because they contain lines of interesting **molecular, ionic, and atomic** species. Skinner et al. (1997) reported the detection of the 35 μm OH line in Arp 220. Fischer et al. (1997, 1999) found that the far-infrared molecular absorption lines of OH, H_2O , CH, and NH_3 are significantly stronger in Arp 220 than in less luminous infrared-bright galaxies while the fine structure lines from ionic species are, to the contrary, extremely weak. Luhman et al. (1998, 2003) found that, relative to the far-infrared luminosity, the [C II] in ULIRGs is typically nearly an order of magnitude weaker than in lower luminosity infrared-bright galaxies. Sturm et al. (1996) reported the detection of two ortho- H_2 pure rotational lines, indicating that high masses of gas are subject to PDR conditions and/or shock activity.

The physical and chemical processes that account for the rich molecular far-infrared spectrum of Arp 220 can be better understood if quantitative values of the column densities of the above species, as well as their excitation conditions, are estimated. The presence of OH and, to some extent, of H_2O , may be indicative of PDR and/or diffuse interstellar cloud chemistry, and their column densities potentially give an estimate of the UV field in the source. On the other hand, large amounts of H_2O are produced in non-dissociative shocks

(e.g. Cernicharo et al. 1999), where the OH abundance is also enhanced (Watson et al. 1985). The OH abundance is expected to be generally higher than that of H₂O in fast dissociative shocks (Neufeld & Dalgarno 1989). H₂O ice in grain mantles may also efficiently return to the gas phase through sublimation of mantles in “hot core” regions. But whatever the characteristics of the regions producing the observed molecular features, the lines under study lie at wavelengths where the enormous infrared continuum flux approaches its maximum, and the molecular excitation of high-dipole species should be strongly affected by absorption of continuum radiation. Hence any reliable estimation of molecular column densities require accurate models for the dust emission. Unfortunately ISO’s lack of angular resolution forces us to rely on plausibility arguments in our assumptions about the regions where the different lines are formed; some of these are based on general requirements of excitation, and others on conclusions from observations of galactic sources. The main goal of this work is thus to shed light on the physical and chemical processes in Arp 220, based on detailed model fits of its continuum and far-infrared molecular/atomic line absorption and emission spectrum. We adopt a distance to Arp 220 of 72 Mpc (projected linear scale of 350 pc/arcsec, Graham et al. 1990). In section 2 we present the ISO/LWS observations; in section 3 we discuss the line identifications; section 4 is a discussion of the models for the continuum emission; section 5 presents the models for the molecular and atomic species; in section 6 we discuss the implications of the radiative transfer models, and section 7 summarizes our main results.

2. Observations

The full 43-197 μm spectrum of Arp 220, obtained with the LWS spectrometer (Clegg et al. 1996) on board ISO (Kessler et al. 1996) (TDT²=27800202), was presented by Fischer et al. (1997, 1999). The grating spectral resolution is $\approx 0.3 \mu\text{m}$ in the 43-93 μm interval (detectors SW1-SW5), and of ≈ 0.6 in the 80-197 μm interval (detectors LW1-LW5), corresponding to $\Delta v \geq 10^3 \text{ km s}^{-1}$. The lines are thus not resolved in velocity. The beam size of $\approx 80''$ ensures that all the continuum and line emission/absorption from Arp 220 (CO size $< 4''$, Scoville et al. 1997, hereafter SYB97) lie within the ISO aperture.

The data we present here was reduced using version 9.1 of the Off Line Processing (OLP) Pipeline system which we found to produce a higher signal-to-noise spectrum than OLP 10.1. However, we adopted the continuum correction given by OLP version 10.1, which typically gives absolute responsivity corrections with uncertainty factors ~ 3 times lower than are produced by version 9 (Tim Grundy, private communication). In order to obtain

²Target Dedicated Time

a smooth spectrum throughout the whole LWS range, the density fluxes given by each detector were corrected by multiplicative scale factors. Corrections were lower than 10% except for detector SW1 (43–64 μm), for which the correction was of 15%. Thus we attribute a conservative uncertainty of 15% to the overall continuum level.

The LWS spectrum of Arp 220 is presented in Figure 1 together with identifications of the most prominent lines. Owing to transient effects, the fluxes of weak lines as observed in the forward and reverse scans were found to differ significantly in some wavelength ranges. In these cases, if a line appeared close to the upper or lower end of a detector, the reverse or forward scan was selected for that line, respectively, to minimize the transient effects (Tim Grundy, private communication). Nevertheless, the average of both scans was used throughout most of the infrared spectrum. In wavelength regions where two detectors' responses overlap, line fluxes were generally found to be consistent. The only exception was the H_2O $3_{22} - 2_{11}$ line at 90 μm , which showed in LW1 a flux 60% weaker than in SW5. We adopted here the SW5 spectrum, but the flux of the above H_2O line should be considered highly uncertain. The subtraction of a baseline (see Fig. 1) added additional uncertainty to the line fluxes, particularly in cases of broad features presumably composed of several lines. With the exception of the H_2O $3_{22} - 2_{11}$ line, we estimate a line flux uncertainty generally lower than 35%.

3. General results

OH and H_2O : The FIR spectrum of Arp 220 is dominated by unresolved OH doublets (that will be simply referred as lines) and H_2O lines in absorption, with the exception of the OH $\Pi_{1/2} 3/2 - 1/2$ emission line at 163.3 μm . Figure 2 shows the level diagram of OH, ortho- H_2O and para- H_2O , and indicates the lines detected in Arp 220. Lines with very different excitation requirements are observed throughout the spectrum. The OH lines $\Pi_{3/2} J = 9/2 - 7/2$ at 65 μm and $\Pi_{1/2} J = 7/2 - 5/2$ at 71 μm have lower levels at 290 K and 415 K above the ground state, respectively, whereas the H_2O lines $4_{32} - 3_{21}$ (59 μm) and $4_{22} - 3_{13}$ (58 μm) have lower levels at 305 K and 205 K. Strong absorption is also observed in the OH ground state lines at 53, 79, and 119 μm , as well as in the H_2O lowest-lying line at 179 μm . This wide range of excitation suggests that several regions with different physical conditions are contributing to the observed features (Fischer et al. 1999), and one of the goals of this work is to provide a reasonable estimate of the nature of these regions and their relative contributions to the spectrum. On the other hand, several of the lines have complex shapes, with evidence of shoulders suggestive of weaker secondary lines. In particular, the ground state OH 119 μm line shows a redshifted "shoulder", which is detected in

both the forward and reverse scans, although with somewhat different strengths. It could be attributed to the $^{18}\text{OH } \Pi_{3/2} 5/2 - 3/2$ line at $120.1 \mu\text{m}$, although contamination by other species such as CH^+ cannot be ruled out. Also, the redshifted “wing” of the $\text{H}_2\text{O } 2_{12} - 1_{01}$ line at $179 \mu\text{m}$, attributed in Fig. 1 to the $\text{H}_2\text{O } 2_{21} - 2_{12}$ line, could also be contaminated by H_2^{18}O , CH (see Fig. 7), and H_3O^+ .

CH and NH: The spectrum contains lines from other molecular species: like CH at $149 \mu\text{m}$, NH_3 at 125 , 166 and $170 \mu\text{m}$ and, very interestingly, strong absorptions at 102 and $153.2 \mu\text{m}$ that have been identified as NH in Fig 1. Evidence for the latter identifications is strengthened because of the presence of weak line-like features at $155.74 \mu\text{m}$, and marginally at $151.53 \mu\text{m}$, which would correspond to the $\text{NH } 2_1 - 1_1$ and $2_1 - 1_0$ lines, respectively (see also Fig. 3). Conceivably, the line absorptions at 102 and $153.2 \mu\text{m}$ could be severely contaminated by other species, like C_3 , H_2^{18}O , NH_3 , and even OH^+ . C_3 has a strong transition at $153.3 \mu\text{m}$, but its contribution is expected to be minimal due to the lack of detection of other adjacent C_3 lines (in particular at $154.86 \mu\text{m}$). The absorption at $102 \mu\text{m}$ may be contaminated by the $\text{H}_2^{18}\text{O } 2_{20} - 1_{11}$ line (just at $102.0 \mu\text{m}$), but since the H_2^{18}O should not be as strong as the corresponding adjacent line of the main isotope H_2^{16}O , we regard this identification as also unlikely. Some contribution of NH_3 lines to the $102 \mu\text{m}$ feature might be expected, but they are somewhat shifted in wavelength (they lie between 101.5 and $101.7 \mu\text{m}$). Both features could be contaminated to some extent by OH^+ , with strong lines at 101.70 and $101.92 \mu\text{m}$ ($N_J = 3_3 - 2_2$ and $3_4 - 2_3$) and at $153.0 \mu\text{m}$ ($2_3 - 1_2$), but the strong absorption at $153.2 \mu\text{m}$ absorption could never be explained by OH^+ alone. Therefore, despite the possible contamination from other molecules, NH is probably responsible for most, if not all, of the observed $153.2 \mu\text{m}$ absorption (see also Fig. 7). Thus, although the definitive assignment to NH should await confirmation with higher spectral resolution observations of the lowest-lying NH transitions at $\sim 10^3$ GHz, we conclude that ISO observations strongly support its detection in Arp 220, and advance a model of the observed absorption (section 5) that can be useful to direct future observational and theoretical studies. If confirmed, this detection is the first extragalactic detection of NH , which has been previously detected only in galactic diffuse clouds through electronic transitions (Meyer & Roth 1991; Crawford & Williams 1997) and, interestingly, toward Sgr B2 in the Galactic Center via the same transitions detected in Arp 220 (Cernicharo, Goicoechea, & Caux 2000; Goicoechea, Rodríguez-Fernández, & Cernicharo 2004, hereafter GRC04).

NH₃: The spectrum of Arp 220 around 125 and $170 \mu\text{m}$, shown in Figure 4, strongly supports the identification of NH_3 . The shape of the $165.7 \mu\text{m}$ feature indicates transient effects, but the line is detected in both the forward and reverse scans. Some H_2O lines may contribute to the observed 125 and $127 \mu\text{m}$ features, but they are shifted in wavelength relative to the strongest absorption. This is the first extragalactic detection of infrared NH_3

lines. With the detection of NH and NH₃ we might expect to detect NH₂, but there is no evidence for its strongest expected lines at 159.5, 117.8 and 104.9 μm .

CO?: An apparent emission line, detected in both the forward and reverse scans, is present at 173.7 μm in Fig. 1. It coincides rather well with the expected position of the CO $J = 15 - 14$ line at 173.63 μm . This identification cannot be confirmed by the detection of other expected CO lines because the CO $J = 14 - 13$ line at 186.0 μm lies at the noisy edge of the LW5 detector and the CO $J = 16 - 15$ line at 162.8 μm is blended with the OH 163.3 μm line. The higher J lines are expected to be too weak to be detectable, given the observed strength of the 173.7 μm feature.

[O I] and [C II]: The ISO spectrum also shows the [O I] 63.2 μm line in absorption and the [C II] 157.7 μm line in emission. The [O I] 145.5 μm line is not detected. These lines, as observed in Arp 220 and other ULIRGs, have been discussed elsewhere (Fischer et al. 1997, 1999; Luhman et al. 1998, 2003). In section 5 we present a simple model of the Arp 220 spectrum that may shed some light on the peculiar behavior of these lines in Arp 220.

In summary, the far-infrared spectrum of Arp 220 shows molecular lines of OH, H₂O, CH, NH, and NH₃. The atomic lines of [O I] at 63 μm and [C II] at 158 μm are also detected. Lines of other species, like CO, H₃O⁺, CH⁺, and OH⁺, could also contaminate the observed features, but our limited spectral resolution prevents the possibility of unambiguous detection. Only the [C II] 158 μm and the OH $\Pi_{1/2} 3/2 - 1/2$ 163 μm lines are clearly observed in emission. Lines from ions that would trace H II regions and/or an AGN are absent.

4. Models for the continuum

Figure 1 shows that the continuum peaks around $\sim 40 - 50 \mu\text{m}$. The bulk of the continuum from Arp 220 is emitted by heated dust grains. At 1.3 millimeter wavelengths, Sakamoto et al. (1999) showed that the continuum arises almost exclusively from the nuclei, with an equivalent size of $\sim 0''.4$. **The non-thermal contribution at 1.3 mm is expected to be < 15% (cf. Fig. 6 of Anantharamaiah et al. 2000).** On the other hand, Soifer et al. (1999, hereafter S99) have shown that the two nuclei also account for essentially all the continuum at 25 μm . Combining both observations, S99 proposed two alternative scenarios to explain the continuum emission of Arp 220 from far-infrared to millimeter wavelengths. Our models of the continuum emission are entirely based on these scenarios, which we have examined and refined quantitatively on the basis of our ISO 45-200 μm spectrum.

Model S₁: In the first scenario (hereafter S₁), it is assumed that the emission from the nuclei is not significantly attenuated at 25 μm by foreground material. We have simulated

the emission from the nuclei as arising from a single nucleus with effective size of $0''.41$. With an effective dust temperature of 85 K, and optically thick emission in the submillimeter, the requirement that the fluxes at 25 and 1300 μm arise from the nuclei is fulfilled. However, the emission at 60-100 μm , as well as the total luminosity from the galaxy, are then underestimated and a more extended region (hereafter ER) must be invoked to account for the remaining flux. We identify this surrounding environment with the extended emission observed in CO, HCN, and HCO⁺. In this first scenario, then, most of the Arp 220 luminosity is produced in the ER, which has been modeled as a thin disk by SYB97, and as a warped disk by Eckart & Downes (2001). Significantly, if this model is correct, a spatially extended starburst, responsible for the bulk of the far-infrared luminosity is inferred.

Our best fit to the continuum using model S₁ assumptions is presented in Fig. 5a, with derived physical parameters listed in Table 1. In all models, uniform densities throughout the different components are assumed for simplicity. In Table 1, λ_t is the wavelength for which the nucleus becomes optically thin ($\tau = 1$); owing to the high opacities involved, the inferred emission is rather insensitive to the spectral index β . Thus we have given values of the physical parameters for $\beta = 1.5$ and $\beta = 2$. The dust mass has been derived by assuming a mass-opacity coefficient of 12 cm²/gr at 200 μm (Hildebrand 1983). The parameters that have been allowed to vary in our models of the ER are the dust temperature T_d , the diameter d (within the range 500–800 pc), and the dust opacity; β is fixed to 2 to ensure negligible emission at millimeter wavelengths (see S99).

Model S₂: In the second scenario (hereafter S₂), the emission from the nuclei at 25 μm is assumed to be attenuated by **foreground dust** with $\tau_{\text{abs}}(24.5 \mu\text{m}) = 1.2$, a value which was chosen to be compatible with the silicate absorption observed in S99. The nuclei account for the required flux at 24.5 and 1300 μm with $T_d \approx 106$ K, significantly warmer than the ~ 85 K temperature in S₁ and, as before, the emission in the submillimeter is optically thick (see Table 1). In this scenario as well, however, the flux at 60–100 μm is again underestimated, and an emitting ER must also be involved to account for it. Nevertheless, the luminosity from the warm nuclei in S₂ is enough to account for the observed total luminosity from Arp 220, so that the ER merely re-radiates the emission from the nuclei and no extended starburst is then needed to provide the bulk of the luminosity.

Figure 5b shows our best fit for S₂. The unique parameters that have been allowed to vary in our models of the ER are the diameter d and the dust opacity; β is again fixed to 2, and the dust temperature T_d (shown in the insert panel of Figure 5b) has been computed from the requirement that the heating balance the cooling throughout the source. **The calculation of T_d is carried on by assuming spherical symmetry, with the nucleus, the primary heating source, located at the center of the ER. The ER is divided**

into a set of spherical shells to account for the variation of T_d with the distance to the nucleus. **Once the T_d profile is calculated, the flux contributions of the attenuated nucleus and the ER are computed separately, and added up to give the total flux.** Despite the good fit to the continuum in Fig. 5b, S_2 implicitly supposes a lack of spherical symmetry (e.g. **the nuclear disk by SYB97**) or some clumpiness, because the derived radial opacity of the ER at $24.5 \mu\text{m}$ is 11.3, whereas the adopted opacity of the absorbing shell in front of the nuclei is $\tau_{\text{abs}}(24.5 \mu\text{m}) = 1.2$. **Furthermore, we do not rule out the possibility that the ER is only partially responsible for the foreground dust absorption of the nuclear emission.** If the ER were concentrated in a thin disk as proposed by SYB97, little dust in the ER would be expected to lie in front of the nuclei and significant dust absorption would be attributed to another component, “the halo” (see section 5.1). Therefore our results for S_2 , which assume spherical shapes for the nucleus and the ER, should be considered only approximate, but suggestive. The intrinsic geometry that underlies S_2 **departs from spherical symmetry and implies that the total luminosity, which coincides with the luminosity of the nuclei, is lower than the value inferred in S_1 , where spherical symmetry and uniformity is assumed for each component (Table 1).**

Table 1 shows that $\beta = 2$ yields a dust mass of $\sim 10^8 M_\odot$ for the nucleus, and that S_1 gives a mass 1.4 times higher than S_2 . Since SYB97 infer a dynamical mass of $6 - 8 \times 10^9 M_\odot$ enclosed in the inner 250 pc radius, and this region contains the nuclei and most of the inner disk (the ER), S_2 with $\beta = 1.5$ is favoured in our models provided that the gas-to-dust mass ratio is not lower than the standard value of ≈ 100 . **The consistency between the dynamical mass and the mass derived from the dust emission indicates that the ISM dominates the dynamics in these inner regions of Arp 220.**

It is worth noting that these models may be applied to the source as a whole, as implicitly assumed above, or alternatively to each one of an ensemble of N_c smaller clouds of radius R_c that do not spatially overlap along the line of sight. The value of $N_c \times R_c^2$ determines the absolute scale, and the radial opacity and temperature distribution of each cloud as a function of the normalized radial coordinate, R_c , determine the continuum shape. Identical results are found as long as the above parameters remain constant. Furthermore, both alternatives give identical total masses, but differ in the inferred mean density, which scales as $\sqrt{N_c}$. $N_c = 1$ gives the lowest mean density $\langle n(\text{H}_2) \rangle$, which is listed in Table 1. Typical values of a few $\times 10^4 \text{ cm}^{-3}$ are derived for the nuclei, accounting for the emission from molecules with high dipole moment such as HCN, HCO^+ , HC_3N and CN (see also SYB97). For the ER we obtain $n(\text{H}_2) < 10^3 \text{ cm}^{-3}$; since HCN and HCO^+ appear to show extended low-level emission (Radford et al. 1991b), it is suggested that the actual density is higher than this lower limit or that the gas is clumpy. **The low density derived for the ER may also**

be a consequence of the spherical shape attributed to the ER: if the mass we derive for the ER were concentrated in a thin disk with full thickness of 32 pc (SYB97), the mean H_2 density would be $7 \times 10^3 \text{ cm}^{-3}$. We will adopt the density given in Table 1, $n(\text{H}_2) = 5.3 \times 10^2 \text{ cm}^{-3}$, in the models for molecules and atoms, but will also explore the results obtained with a density one order of magnitude higher than the quoted value.

Although both scenarios S_1 and S_2 reproduce the continuum emission from Arp 220 over the 25-1300 μm interval and support the constraints on the nuclear sizes derived from the available high angular resolution continuum measurements, the dynamical masses inferred from CO millimeter line observations favour S_2 with $\beta = 1.5$ for the nuclei. Moreover, as we discuss in sections 5.3 and 6.1, the observed line absorption/emission also favours model S_2 . We thus adopt scenario S_2 for the detailed modeling and analysis of the line emission and absorption.

4.1. Extinction

In both scenarios, the high brightness and compactness of the nuclei imply extreme continuum optical depth, corresponding to $A_V \sim 10^4 \text{ mag}$. This conclusion is in strong contrast with the much more moderate values derived from infrared and radio hydrogen recombination lines (Genzel et al. 1998; Anantharamaiah et al. 2000). The high extinction derived here is the direct result of the measured 1.3 mm continuum flux from the nuclei, 210 mJy (Carico et al. 1992; Sakamoto et al. 1999), and the observed upper limit of the corresponding source size, $\sim 0''.4$ (Sakamoto et al. 1999). These values imply $\tau_d^{1.3\text{mm}} \times T_d(\text{K}) \sim 40$, which shows that even assuming unexpectedly high average dust temperatures (e.g. $T_d = 200 \text{ K}$) and $\beta = 1$ the dust emission is still optically thick even at 200 μm . On the other hand, the radio recombination lines observed by Anantharamaiah et al. (2000) are not affected by dust obscuration, although their predicted fluxes and the derived extinction may be somewhat model dependent. These very different extinction values may be understood if we assume that the observed H recombination lines, tracing primarily star formation, are formed in the outermost regions of the nuclei, while a buried central energy source, responsible for the heating of dust in the innermost regions of the nuclei and a significant fraction of the galactic luminosity, is weak in recombination lines. If weak in recombination lines, the buried energy source is presumably weak in PAH features and PDR lines as well, consistent with the strong [C II] deficit in Arp 220 (see also section 5). Dust-bounded ionized regions, in which most of the Lyman continuum from nuclear starbursts or AGN is absorbed by dust rather than by gas, may explain these properties of Arp 220, as was proposed by

Luhman et al. (2003). We further argue that the Lyman continuum luminosities derived from recombination lines do not empirically rule out the possibility that an AGN accounts for more than $\sim 50\%$ of the bolometric luminosity of Arp 220, because of the high dispersion of $L_{\text{bol}}/L_{\text{Ly}\alpha}$ values shown by both starburst galaxies and AGN, the range of $L_{\text{Ly}\alpha}$ values derived from different tracers in Arp 220, and the uncertainties in the assumed extinction law and the derived extinction (Genzel et al. 1998). Our derived $N(\text{H}_2) \sim 10^{25} \text{ cm}^{-2}$ is high enough to obscure a source of high 5–10 keV luminosity from one or both nuclei in Arp 220, so that a hidden AGN is allowed despite the relatively weak X-ray luminosity observed in Arp 220 (Clements et al. 2002). Haas et al. (2001) have also argued that a hidden AGN powers much of the luminosity of Arp 220 on the basis of the observed submillimeter continuum excess relative to the $7.7 \mu\text{m}$ PAH flux.

5. Models for molecules and atoms

5.1. Comparison with Sgr B2

The comparison of the spectrum of Arp 220 with that of some well-studied galactic sources provides important clues about the regions where the observed lines are formed, while emphasizing the unique features that characterize the extragalactic source. In this sense, Sgr B2 (component M) is an ideal comparison source, just because it shares common **observational** properties with Arp 220 despite the obvious differences in spatial scale (and indeed possibly in nature). Figure 6 shows the continuum-normalized spectra of Sgr B2 (M) (kindly provided by J.R. Goicoechea) and Arp 220. Sgr B2 harbors newly born OB stars, ultracompact H II regions, and hot cores, enshrined in a dusty envelope which is heated by shocks and by radiation, and which radiates a high IR luminosity (see GRC04 and references therein). The envelope has the highest extinction in the direction of the N- and M-condensations, with optically thick emission in the far-infrared up to $\sim 200 \mu\text{m}$, and with foreground absorption lines of OH, H₂O, CH, and [O I] observed with the ISO/LWS grating (GRC04, Fig. 6). Fabry-Perot observations of Sgr B2 have also allowed the detection of other molecular species like NH, NH₃, NH₂, HD, H₃O⁺, and C₃, as well as high excitation lines of OH and H₂O (GRC04 and references therein). As shown above (section 4), the extinction toward the nuclei of Arp 220 is also very high, although the dust is significantly warmer than in the Sgr B2 envelope. The comparison between both sources is meaningful (at least as a first approximation, and from the point of view of the radiative transfer) as long as the nuclear region of Arp 220 can be considered an ensemble of continuum-thick molecular-rich clouds such as Sgr B2. For an ensemble of Sgr B2-like **clouds**, since both the continuum and the line absorption scale with the number of clouds, the *continuum-normalized* spectrum is

the same as that of one individual cloud. This result applies even if the lines in the ensemble are broadened relative to the one-cloud emission due to cloud-to-cloud velocity dispersion and rotation, provided that the lines remain unresolved with the grating resolution. Thus the differences between the two spectra in Fig. 6 reveal real differences in excitation and/or column densities.

The high-excitation lines of OH and H₂O are much stronger in Arp 220 than in Sgr B2 (M) (see Fig. 6). In particular, the OH $\Pi_{3/2} J = 9/2 - 7/2$ 65 μm line, with strong absorption in Arp 220, is not detected in the grating spectrum of Sgr B2, and the OH $\Pi_{3/2} J = 7/2 - 5/2$ 84 μm line is also much weaker in Sgr B2 (M). This strongly indicates the presence in Arp 220 of a high excitation region with relatively high OH column densities. Fabry-Perot spectral resolution ($\Delta v \sim 35 \text{ km s}^{-1}$) allowed Goicoechea & Cernicharo (2002) to detect high excitation OH lines in Sgr B2, and showed that they are pumped through absorption of far-infrared photons. In Arp 220 also, these lines appear to be pumped by the strong infrared radiation flux in the neighbourhood of the nuclei (section 5.2). Toward Sgr B2 (M), Goicoechea & Cernicharo (2002) derived $N(\text{OH}) \approx 2 \times 10^{16} \text{ cm}^{-2}$, and we may expect significantly higher column densities toward the nuclei of Arp 220. The peculiarity of Arp 220 is also revealed by the relatively strong absorptions in the NH₃ and NH lines. These species have also been detected toward Sgr B2 (M) with Fabry-Perot spectral resolution (Ceccarelli et al. 2002, GRC04), but Fig. 6 indicates much higher column densities in Arp 220, at least toward the nuclei.

GRC04 found that the OH $\Pi_{1/2} J = 3/2 - 1/2$ 163 μm line, pumped through absorption of photons in the OH $\Pi_{1/2} - \Pi_{3/2} J = 3/2 - 3/2$ 53.3 μm line, shows emission over a large region associated with Sgr B2. In Arp 220 the line is strong, suggesting significant widespread emission, i.e. from the ER. It is also worth noting that, although the [C II] line is not detected in the grating spectrum of Sgr B2 (M), Fabry-Perot observations allowed its detection (Vastel et al. 2002, GRC04), with a flux of $\approx 1.5 \times 10^{-17} \text{ W cm}^{-2}$ for the component observed in emission. This value is, within a factor of 2, similar to strengths in the surrounding region where the continuum is however much weaker (GRC04). Therefore, in addition to effects of self-absorption and absorption of the continuum by C⁺ in foreground excitation clouds (Vastel et al. 2002, GRC04), the low [C II]/FIR ratio at Sgr B2 (M) is due to a strong increase in the FIR emission that is not accompanied by a corresponding rise of PDR line emission. Dust-bounded ionized regions (Luhman et al. 2003), together with extinction effects in the far-infrared, might account for the lack of PDR line emission associated with this additional infrared component. This is similar to our hypothesis for Arp 220's nuclei (section 5.6). The [C II] emission in Arp 220 is expected to arise from PDRs in the ER, where the bulk of the PAH emission is found (Soifer et al. 2002). As shown in Fig. 5, the ER dominates the observed far-infrared emission, but since the main heating sources are, according to model

S_2 , the nuclei, the ER is mainly heated via absorption of infrared rather than UV photons, its *intrinsic* luminosity is relatively low, and hence the [C II] line remains weak (section 5.6).

Finally, we stress that Arp 220 and Sgr B2 (M) show similar absorptions in the ground-state lines of OH and H₂O, as well as in the CH line at 149 μm . Fabry-Perot observations of the low-lying OH and H₂O lines toward Sgr B2 (M) (Cernicharo et al. 1997, GRC04), indicate that most of these absorptions are produced in diffuse low-excitation clouds located along the line of sight to Sgr B2 but not physically associated with it. The similar absorptions found in Arp 220 strongly suggest that a diffuse medium is also present there. In fact we have found that the combination model of the nuclei and the ER that reproduces reasonably the high excitation OH and H₂O lines, fails to explain the strong absorptions in the lowest-lying OH and H₂O lines. The presence of an absorbing diffuse component in Arp 220 is supported by (i) the detection of CH at 149 μm , because most of the corresponding absorption toward Sgr B2, with strikingly similar strength, is associated with translucent clouds (Stacey, Lugten, & Genzel 1987, GRC04) and is therefore expected to trace primarily gas in diffuse clouds; (ii) the observed absorption in the [O I] 63 μm line, which could suggest foreground absorption since most of the comparable [O I] absorption observed toward Sgr B2 is also produced by foreground gas in diffuse clouds (Baluteau et al. 1997); (iii) the low ratio of the CO (2-1) to the 1.3mm continuum emission toward the nuclei of Arp 220 and, most important, the low brightness of both the CO (1-0) and CO (2-1) lines (SYB97), which suggest line-of-sight blocking of the nuclear CO emission by low-excitation gas (Sakamoto et al. 1999). The above points strongly suggest the presence of an absorbing component in front of the nuclear region in which *both* the particle density and the infrared radiation density are relatively low. This component could also account for significant absorption of the nuclear continuum emission in scenario S_2 if the ER were a thin disk (section 4). We will refer to this diffuse component of Arp 220 as “the halo”.

5.2. Outline of the models

The dust models described in section 4 set up the basis for the molecular calculations. These are carried out with the method described in González-Alfonso & Cernicharo (1997, 1999), which computes the statistical equilibrium populations of a given molecule by assuming spherical symmetry and line broadening caused by microturbulence and/or radial velocity gradients. In the present calculations we have assumed, for simplicity, pure microturbulent line broadening, but some tests showed that the inclusion of a radial velocity gradient hardly

modified the results. Rotational motion, which is present around the nuclear region of Arp 220 (e.g. SYB97, Sakamoto et al. 1999; Downes & Solomon 1998), is not included. Nevertheless, the assumption of spherical symmetry and our neglect of steep velocity gradients that may result from cloud-to-cloud velocity dispersion may be considered more critical.

Our non-local code accounts for radiative trapping in the molecular lines, collisional excitation, and excitation through absorption of photons emitted by dust. The dust parameters derived above for S_1 and S_2 are used in the calculations for molecules. As in the case of the continuum models, we have modeled the nucleus and the ER separately. This is required, in S_2 , by the relatively low dust opacities of the ER toward the nucleus as compared with the radial opacity of the ER (see section 4), and involves inevitably an additional uncertainty.

Since the dust in the nucleus is very optically thick throughout the ISO wavelength range, model results are only sensitive to the molecular column densities in the **externalmost** parts of the nucleus. It is therefore assumed that only in the externalmost regions of the nucleus, where the infrared lines are formed, the molecular abundances are different from zero (see Goicoechea & Cernicharo 2002, for the case of Sgr B2). Since dust and molecules are assumed to be coexistent, extinction effects within the nucleus are implicitly taken into account; they place important constraints on the molecular abundances. We have adopted a molecular shell thickness of 2×10^{18} cm, which for a mean $n(\text{H}_2) = 4.6 \times 10^4 \text{ cm}^{-3}$ (in S_2) corresponds to $A_V \sim 50$ mag and $\tau(50 \mu\text{m}) \approx 0.3$. For lines around $50 \mu\text{m}$, the contribution to the absorption by molecules located deeper into the nucleus was checked in some tests to be relatively weak, due to both dust and molecular line optical depth effects. Foreground extinction in S_2 was also taken into account. In the models for the ERs, which have much lower continuum opacities, we have assumed that dust and molecules have uniform abundance ratio throughout the whole region. The presence of the central nucleus is included in the calculation of the statistical equilibrium populations, but ignored in the calculation of the emergent fluxes to avoid accounting for it twice.

Toward the nucleus, absorption of continuum radiation determines the excitation of OH and H_2O ; the radiative rates are much higher than the collisional ones even for **very high pressure molecular gas, such as is found in molecular shocks** ($n(\text{H}_2) = 5 \times 10^6 \text{ cm}^{-3}$ and $T_k = 300 \text{ K}$; we will refer to these values as “**shock conditions**”). The rate coefficients of Offer, van Hemert, & van Dishoeck (1994) and Green, Maluendes, & McLean (1993) were used to check the collisional excitation of OH and H_2O , respectively. If **widespread shock conditions** were present, only the absorption of the lowest-lying lines would be significantly affected. Since we use a halo to match these lines, we cannot distinguish between shock and non-shock conditions (i.e., the line ratios are not sensitive to $n(\text{H}_2)$ and T_k within plausible values). For simplicity, physical parameters for the halo are

derived by assuming non-shock conditions for the nucleus. Concerning the ER, widespread shock conditions are not applicable because they would involve strong emission in the H₂O 2₁₂ - 1₀₁ and 3₀₃ - 2₁₂ lines and in most OH lines (hard to cancel by any halo). Our molecular data are therefore only sensitive to the radial molecular column density N and the microturbulent velocity dispersion σ_v , so that only these two computational parameters are required to define a model of a given component.

Similar to the dust models, models for molecules may be applied to the source as a whole, or alternatively to each one of an ensemble of smaller clouds that do not spatially overlap along the line of sight. Besides the scaling relationships pointed out above, the molecular column density must remain the same to obtain identical results when varying N_c . On the other hand, once the number of continuum sources N_c is fixed (e.g., $N_c = 1$), the same line fluxes are obtained if both N and σ_v are divided by the same factor f_c , and the resulting fluxes are then multiplied by f_c . The latter reflects the approximate equivalence between one absorbing cloud with column density N and velocity dispersion σ_v , and f_c clouds, with parameters N/f_c and σ_v/f_c , which overlap on the sky but not in the line-of-sight velocity space³.

Variations in N and σ_v have different effects on the line absorptions. If σ_v decreases the absorptions are weaker for optically thick lines, but due to the increase of line opacities, the high-energy levels become more populated and the above weakness is more pronounced for the low-lying lines. On the other hand, the increase of N has little effect on very optically thick lines (most of them low-lying lines), but a larger effect on those with moderate opacities.

We have generated a grid of models for the nucleus and the ER of both S₁ and S₂, by varying the above free parameters N and σ_v . In each model, the molecular shell is divided into a set of sub-shells in order to account for the spatial variation of the excitation temperatures of the lines. First we searched for the nucleus+ER combination model that best matches the OH and H₂O non-ground-state lines, with the same value of σ_v for both species. As pointed out above, the relatively deep absorptions of the OH and H₂O ground-state lines could not be fitted satisfactorily by any model, and a halo component was added to match these lines. The halo was assumed to be a purely absorbing shell; although the equilibrium populations were computed in spherical symmetry assuming a size of three times that of the ER, limb emission (i.e. emission for impact parameters that do not cross the continuum source) was ignored in the calculation of the fluxes emergent from the halo.

Once the model for OH and H₂O is determined, models for the other detected species

³In fact the models could be defined in terms of the two independent variables N/σ_v and $N \times f_c$; nevertheless we will use the variables N and σ_v with $f_c=1$.

are performed, also keeping fixed the value of σ_v derived above for each component. Figure 7 compares the derived model spectrum and the observed one, and Table 2 lists the inferred parameters. The next sections are devoted to explaining the details of these calculations and results.

5.3. OH and H₂O

Our best model fits for the high excitation lines of OH and H₂O come from model S₂, and the results presented here will focus on this scenario. The main difference between S₁ and S₂ consists in the higher column densities and/or broader line widths required by S₁ to reproduce the lines, owing to the fact that T_d is significantly lower in S₁. Models for the nucleus with broad line widths ($\sigma_v > 60 \text{ km s}^{-1}$, see below), however, predict strong absorptions in some OH and H₂O lines, such as the OH $\Pi_{1/2} J = 5/2 - 3/2$ 98 μm and the H₂O 3₁₃ - 2₀₂ 138 μm lines, which are not observed. Therefore S₂, which still requires high column densities, **is a better fit to the data.**

Our best model fits for the high excitation lines involve column densities of $2 - 6 \times 10^{17} \text{ cm}^{-2}$ for both OH and H₂O, and $\sigma_v = 50 - 30 \text{ km s}^{-1}$, towards the nucleus. The model for the nucleus reproduces nearly the whole absorption in the OH $\Pi_{1/2} 7/2 - 5/2$ and $\Pi_{1/2} - \Pi_{3/2} 5/2 - 5/2$ lines, most of the OH $\Pi_{3/2} 9/2 - 7/2$, and significant absorption in the other lines but by far too weak in the ground-state lines. It also reproduces the full absorptions in the H₂O 4₂₂ - 3₁₃, 4₃₂ - 3₂₁, 3₃₀ - 2₂₁, 3₃₁ - 2₂₀, and 4₂₃ - 3₁₂ lines, and significant absorption in the 3₂₁ - 2₁₂ and others. The somewhat low value derived for σ_v is required to keep the absorptions weak in some low excitation lines which are marginally or not detected. Since low σ_v implies low velocity coverage for absorption of the continuum, the column densities that are needed to explain the absolute values of the absorptions in high excitation lines are relatively high. We stress that this value of σ_v must be interpreted as a strong lower limit on the linewidths that would be observed with high enough spectral resolution, because rotation and cloud-to-cloud velocity dispersion would broaden the observed lines. The CO kinematic models of Arp 220 by SYB97 found a generic value of $\sigma_v = 90 \text{ km s}^{-1}$; as the authors discuss this value should be considered the joint effect of the local linewidth and the cloud-to-cloud velocity dispersion over a scale of $\sim 100 \text{ pc}$. Our σ_v is the local linewidth involved in the calculation of opacities and directly related to the molecular excitation, and thus the kinematic value of SYB97 must be considered here an upper limit.

It is worth noting that the above column densities are derived by forcing the OH and H₂O high excitation lines to arise in the same region. A slight improvement to the fit of the H₂O lines is obtained with even lower σ_v , 25 km s^{-1} , and $N(\text{H}_2\text{O}) \sim 10^{18} \text{ cm}^{-2}$. This

may indicate that H₂O and OH toward the nucleus do not arise in the same regions. We will adopt in the following the nucleus model with $\sigma_v = 50 \text{ km s}^{-1}$, corresponding to the spectrum shown in Fig. 7 and the parameters given in Table 2, and estimate an uncertainty of a factor of ~ 3 on the derived column densities.

Once the model for the nucleus is matched, **the combination nucleus+ER** that better accounts for the remaining flux in non ground-state lines is searched for. **For densities in the ER $n(\text{H}_2) < 10^4 \text{ cm}^{-3}$ (section 4) and $T_k = T_d$, the OH and H₂O collisional excitation is found to be negligible in comparison with the radiative excitation. We have also explored the plausible situation that the OH lines are formed within the C⁺ region of PDRs (see section 5.6): assuming $T_k = 300 \text{ K}$ (the maximum allowed by the collisional rates of Offer et al. 1994) and $n(\text{H}_2) < 10^4 \text{ cm}^{-3}$, radiative rates still dominate over collisional rates, and results are found indistinguishable from those obtained with lower T_k values. Only densities above 10^5 cm^{-3} with $T_k = 300 \text{ K}$ would give results significantly different for the ground-state transitions of OH.**

The ER mainly accounts for the OH $\Pi_{1/2} 3/2 - 1/2 163 \mu\text{m}$ line, which is uniquely observed in emission (but predicted in absorption in the nuclei), for more than half of the absorption observed in the OH $\Pi_{3/2} 7/2 - 5/2$ line, for reemission in the $\Pi_{1/2} 5/2 - 3/2$, and for significant absorption in the three ground-state OH lines. We estimate for the ER $N(\text{OH}) \sim 2 \times 10^{17} \text{ cm}^{-2}$, with $\sigma_v = 50 \text{ km s}^{-1}$ throughout most of the ER and $\sigma_v = 90 \text{ km s}^{-1}$ just around the nucleus. This higher value of σ_v was required to obtain significant reemission in the **non-detected OH $\Pi_{1/2} 5/2 - 3/2$ line**; since here geometrical effects may be important, this result should be considered with caution. For H₂O we obtain a significantly lower $N(\text{H}_2\text{O}) \sim 3 \times 10^{16} \text{ cm}^{-2}$, giving significant absorption in the $3_{21} - 3_{12}$, $2_{20} - 1_{11}$, and $2_{21} - 1_{10}$ lines. and some reemission in the $3_{03} - 2_{12}$ line. Since the halo also yields some absorption in these H₂O lines but much deeper absorption in the ground-state $2_{12} - 1_{01}$ one (see below), the relative H₂O column density in these components is not well determined.

In the halo, the values of $N(\text{OH})$ and σ_v were determined by fitting the missing absorption in the three OH ground-state lines. A value of σ_v relatively low, $15\text{--}20 \text{ km s}^{-1}$, and $N(\text{OH}) \sim 2 \times 10^{16} \text{ cm}^{-2}$, were found to reasonably fit the fluxes of the 79 and 119 μm lines, though the flux of the 53 μm line is somewhat underestimated (Fig. 7). Higher values of σ_v would predict too much absorption in the already saturated 119 μm line. For H₂O we find $N(\text{H}_2\text{O}) \sim 1.5 \times 10^{16} \text{ cm}^{-2}$. Owing to the strong radiation field from the nucleus and ER, H₂O in the halo is still significantly excited, thus yielding also some absorption in the $2_{20} - 1_{11}$, $2_{21} - 1_{10}$ and $3_{03} - 2_{12}$ lines.

Despite the generally satisfactory fit obtained for the OH and H₂O lines, the shoulder of the OH 119 μm line, presumably produced by the ¹⁸OH $\Pi_{3/2}$ 5/2 – 3/2 line, is not reproduced. The models assume ¹⁶OH/¹⁸OH=500; however, the isotopic abundance ratio in Arp 220 required to reasonably fit the 120 μm shoulder is as low as ¹⁶OH/¹⁸OH~50. This value cannot be ruled out if ¹⁴N is efficiently converted into ¹⁸O in nuclear processing of high mass stars, and then efficiently ejected to the interstellar medium through stellar winds and/or supernovae (Henkel & Mauersberger 1993). Also, there is compelling evidence for isotopic ratios of 150–200 in starburst regions of nearby galaxies (Henkel & Mauersberger 1993). Due to the low spectral resolution of the spectrum, and the possibility that the feature is contaminated by other species, we do not attempt to place useful constraints on this ratio. Nevertheless, we conclude that a very low ¹⁶OH/¹⁸OH abundance ratio likely applies to Arp 220, perhaps indicating an advanced stage starburst (Henkel & Mauersberger 1993).

The model of Fig. 7 predicts an absorbing flux of 1.8×10^{-12} erg s⁻¹ cm⁻² for the $\Pi_{1/2}$ – $\Pi_{3/2}$ 5/2–3/2 line at 34.6 μm , in reasonable agreement with the observed flux of 2.1×10^{-12} erg s⁻¹ cm⁻² reported by Skinner et al. (1997). Concerning the OH-megamaser emission in the 1.667 GHz line, our models predict inversion in the line, but with low gain and by far too weak to account for the observed emission. Proper models for the maser emission require a much finer spatial grid than that used in the present calculations, and we have not attempted to account for it. Even so, some remarks can be given on this score. It is suspected that the OH-megamaser emission is radiatively pumped through absorption of photons in the 34.6 μm and 53.3 μm lines, followed by radiative cascade to lower levels. Since the lower level of the 34.6 μm transition is the ground-state $\Pi_{3/2}$ $J = 3/2$ level, we have found that about 65% of the modeled absorption is predicted to occur in the foreground halo, rather than in the nuclei. As a consequence, the pump efficiency that would be required in our model to explain the 1.667 GHz OH-megamaser line via the 34.6 μm line alone is relatively high, ~ 2%. Nevertheless, given the uncertainty we have in the derived nuclear OH column density, the possibility that some of the maser emission arises in more inner regions, and the expected additional contribution to the pumping by the 53.3 μm line, we conclude that our models are roughly consistent with the OH-megamaser excitation scheme discussed by Skinner et al. (1997).

5.4. CH

Since CH is close to the Hund's coupling case (b) limit in its ² Π ground

state (e.g. Brown & Evenson 1983), we denote its levels through (N, J) , where N is the case (b) rotational quantum number and $J = N \pm \frac{1}{2}$. We assume that the $(2,3/2)-(1,1/2)$ CH line we observe at $149.2 \mu\text{m}$ arises in the halo, based on the results obtained toward the Galactic Center (see GRC04). We derive $N(\text{CH}) \approx 2 \times 10^{15} \text{ cm}^{-2}$ by fitting the feature. Unlike the case of Sgr B2, however, the **submillimeter** emission from the nuclear region of Arp 220 is **strong enough to populate significantly the $(1,3/2)$ level via absorption of photons in the $(1,3/2)-(1,1/2)$ line at $560 \mu\text{m}$, so that our models for the halo predict some contribution by CH $(2,5/2)-(1,3/2)$ to the absorption feature at $181 \mu\text{m}$ (Fig. 7). The latter is uncertain, however, because the feature at $181 \mu\text{m}$ could be contaminated by H_3O^+ (GRC04) and/or by stronger absorption of H_2^{18}O , whose abundance relative to H_2^{16}O could be enhanced relative to the assumed value of $1/500$. On the other hand, there is a wing-like feature at $118.5 \mu\text{m}$, observed in both the forward and reverse scans, which could be caused by the doublet CH $(3,7/2)-(2,5/2)$. If so, and since the excitation of this line requires a relatively strong radiation field, there would be CH in the nuclei that would account for about $1/3$ of the absorption at $149.2 \mu\text{m}$, and the CH column density in the halo would be $2/3$ of the quoted value.**

5.5. NH and NH_3

In contrast with OH and CH, most of the column density of NH and NH_3 we model is contained within the nuclei. Assuming that the $153.2 \mu\text{m}$ absorption feature is caused entirely by NH, we have obtained $N(\text{NH}) \sim 10^{16} \text{ cm}^{-2}$ toward the nucleus. The model reproduces the marginal absorption feature at $76.8 \mu\text{m}$, attributable to the $N_J = 4_J - 3_J$ lines. For the above column density, the $2_2 - 1_1$ and $2_3 - 1_2$ lines at $153.2 \mu\text{m}$ become saturated and the associated feature is not completely reproduced, so that we have added an additional halo component with $N(\text{NH}) \approx 2 \times 10^{15} \text{ cm}^{-2}$ (Table 2). Nevertheless, this model still underestimates the absorption at $102 \mu\text{m}$, strongly suggesting the contribution from other species (section 3).

Within a given K -ladder, the excitation of the NH_3 non-metastable levels is determined by absorption of far-infrared continuum photons, while the metastable levels in $K = 2, 3, \dots$ are **populated** through collisions (see e.g. Ceccarelli et al. 2002, for the case of Sgr B2). In the model of Fig. 7 we have assumed an average density of $n(\text{H}_2) = 4.6 \times 10^4 \text{ cm}^{-3}$ and $T_k = 100 \text{ K}$, but we have checked that the model results are insensitive to the adopted T_k because of the blending of lines from different K -ladders to each spectral feature in our spectrum (Fig. 1). We obtain $N(\text{NH}_3) \sim 3 \times 10^{16} \text{ cm}^{-2}$ toward the nucleus to fit the absorptions at 125 and $127 \mu\text{m}$ (Fig. 7). Besides the absorption in the lines showed in

Fig. 4, the model predicts significant absorption at $\approx 100 \mu\text{m}$ and $\approx 101.6 \mu\text{m}$, caused by $(J, K) = (5, K) - (4, K)$ lines, **which is still insufficient to account for the observed absorption around $101.6 \mu\text{m}$. The model also fails to explain the strong absorption at $166 \mu\text{m}$, and therefore an halo component with $N(\text{NH}_3) \sim 4 \times 10^{15} \text{ cm}^{-2}$ has been added to the global model of Fig. 7. Nevertheless, the halo components of NH and NH_3 should be considered uncertain, because variations in the background continuum associated with each component could in principle account for the missing flux in the lines.**

Finally, we have explored the possibility that the NH_2 radical contributes to the spectrum at some wavelengths. The expected strongest absorption from NH_2 is found at $\approx 159.5 \mu\text{m}$, caused by the strongest components of the $3_{13} - 2_{02}$ ortho line (the hyperfine structure was neglected in these calculations, but the split of the levels due to the unpaired electronic spin of $1/2$ was taken into account). At this wavelength, a marginal absorption feature may be attributed to NH_2 , and is approximately fit with a model for the nucleus where $N(\text{NH}_2) \sim 10^{15} \text{ cm}^{-2}$. We have included this model of NH_2 in Fig. 7 to show that the expected absorption in other lines, like the $3_{22} - 2_{11}$ one at $105 \mu\text{m}$, do not conflict with the observations, and we conclude that $N(\text{NH}_2) \leq 2 \times 10^{15} \text{ cm}^{-2}$.

5.6. C II and O I

A crucial test of our model is whether it can reproduce the [C II] $157.7 \mu\text{m}$ emission and [O I] $63.3 \mu\text{m}$ absorption lines. Among ULIRGs, Arp 220 shows one of the most extreme [C II] deficits ($F_{\text{CII}}/F_{\text{FIR}} \approx 2 \times 10^{-4}$, Luhman et al. 2003). The [C II] line is formed within $A_V \leq 2$ mag from the surfaces of PDRs (e.g. Wolfire, Tielens, & Hollenbach 1990), where the UV field from nearby high mass stars, or from the average galactic field has not been significantly attenuated. In this region, photodissociation maintains most of the gas in atomic or singly ionized form, but some radicals, like OH and NH, find their maximum abundances there (Sternberg & Dalgarno 1995). In particular, OH is expected to be an excellent molecular tracer of PDRs' surfaces, given that its abundance is rather low in UV-shielded quiescent molecular clouds. Its abundance relative to H nuclei within the C^+ region of dense PDRs is expected to approach the value of $\sim 3 \times 10^{-6}$ (Sternberg & Dalgarno 1995). In fact, Goicoechea & Cernicharo (2002) have found an abundance of $\approx 2 \times 10^{-6}$ in Sgr B2, and it could be as high as 5×10^{-6} around the galactic center (Genzel et al. 1985). We have estimated $X(\text{OH}) \sim 1 - 3 \times 10^{-6}$ toward the nucleus of Arp 220.

On the above grounds, and adopting a gas phase carbon abundance of 1.4×10^{-4} (Savage & Sembach 1996), we assumed $N(\text{C}^+)/N(\text{OH})=100$ in Arp 220 (Table 2), and we computed the expected [C II] line emission by assuming excitation through collisions with **atomic**

H (Tielens & Hollenbach 1985). The collisional rates were taken from Launay & Roueff (1977a). **The H densities were assumed to be twice the H₂ densities derived from the continuum models, i.e. $n(\text{H}) = 9.2 \times 10^4 \text{ cm}^{-3}$ in the nucleus and $n(\text{H}) = 1.06 \times 10^3 \text{ cm}^{-3}$ in the ER.** Since the critical density is $3 \times 10^3 \text{ cm}^{-3}$ (Kaufman et al. 1999), results for the nucleus are not critically dependent on the assumed density. They are also insensitive to the assumed temperature as long as it is higher than $\sim 100 \text{ K}$ (Wolfire et al. 1990). Thus our results are only sensitive to the assumed density in the ER, and to the assumed C⁺ abundance.

The result of this calculation has also been added to the overall model of Fig. 7 ($T_k = 500 \text{ K}$ has been assumed). **The model overestimates the observed [C II] emission in only 24%.** The contribution from the nucleus is **only 13%** of that from the ER because of the low volume of the nuclear emitting region. The expected line flux from the nucleus could be lower if absorption of the underlying continuum by low-excitation C⁺ in the halo, ignored in this model, occurs as observed in Sgr B2 (M) (GRC04). The bulk of the line emission arises from the ER. **If the density of the ER were one order of magnitude higher than assumed (section 4), the modeled [C II] emission would be a factor of ≈ 2 stronger than in Fig. 7.** The situation toward Arp 220 resembles what is found in Sgr B2 (GRC04), where the line is emitted mainly from an extended region around condensations N and M, while the strong FIR source itself is not associated with corresponding observable [C II] line emission.

The [O I] 63.3 μm line has been modeled by assuming $N(\text{O I})/N(\text{OH})=250$ (Table 2); although the oxygen abundance is expected to be twice that of C⁺ in the atomic region, it is expected that further atomic oxygen exists deeper into the clouds (Sternberg & Dalgarno 1995). For this reason, a wide range of excitation temperatures is expected for the [O I] line. We have just fitted a single “effective” kinetic temperature and assumed also collisions with atomic H. The same densities as assumed above for C⁺ excitation are used for O I, and the collisional rates are taken from Launay & Roueff (1977b).

Our calculations show that absorption in the [O I] 63.3 μm line is obtained, both toward the nucleus and the ER, with an **effective $T_k = 160 \text{ K}$** , but the line is still too weak to account for the observed feature. Given the high O I abundances that are expected in diffuse clouds (Baluteau et al. 1997), we have added to the model a halo component with $N(\text{O I}) = 3 \times 10^{18} \text{ cm}^{-2}$ (Table 2). This model accounts for the observed absorption at 63.3 μm (Fig. 7).

On the basis of the low extinction derived from infrared and radio H recombination lines and the high optical depth derived from our dust models (section 4.1), and the assumption that [C II] emission is expected to suffer extinction similar to that of the recombination

line emission, we favor the explanation proposed by Luhman et al. (2003, see also section 5.1) that non-PDR far-infrared emission is responsible for the [C II] deficit in Arp 220. Nevertheless, our continuum models by themselves (section 4) cannot rule out the possible role of far-infrared extinction on the measured line fluxes: the derived high nuclear far-infrared opacities indicate that only the **externalmost** regions of the nuclei, where the OH and H₂O lines are formed, and the ER, are able to contribute to the [C II] line emission. Our model fits cannot discern whether the *intrinsic* nuclear [C II] emission is negligible or rather is obscured by dust. In either case, we have shown that the [C II] line is well reproduced by assuming that C⁺ and OH are coexistent.

6. Discussion

6.1. The Extended Region (“ER”)

Our models support the widespread presence of PDRs in the ER. Both the high OH and C II column densities indicate that the UV field from newly formed stars have a profound effect on the chemistry in the ER. Significant contributions from shocks can be neglected, as was pointed out in section 5.2. The H₂O-to-OH abundance ratio is significantly lower than 1, probably indicating enhanced H₂O photodissociation. **As pointed out in section 4, the density is uncertain, in the range $n(\text{H}_2) = 5 \times 10^2 - 7 \times 10^3 \text{ cm}^{-3}$.**

Our models also indicate that the bulk of the [C II] line emission arises in the ER. It is therefore likely that star formation is responsible for this emission. This result is strongly supported by the observations of Soifer et al. (2002), who found that the PAH emission is also spatially extended. Assuming a “normal” [C II]/FIR ratio, i.e. $F_{[\text{C II}]} / F_{\text{FIR}} = 5 \times 10^{-3}$ (Stacey et al. 1991), the expected *intrinsic* FIR emission from the ER is $\sim 3 \times 10^{10} L_{\odot}$, i.e. $\sim 3\%$ of the total galactic luminosity. This estimate supports the scenario S₂ that has been used to model the line emission. According to our models, the total FIR luminosity (due to absorption and re-emission of nuclear infrared radiation) from the ER is much higher than the intrinsic (PDR) emission. Our estimate of the intrinsic ER luminosity is somewhat lower than that derived by Soifer et al. (2002) and Spoon et al. (2004), who found a lower limit of $\sim 7 \times 10^{10} L_{\odot}$, but confirms qualitatively their results. The starburst luminosity in the ER seems to be similar to that of moderately bright infrared galaxies, like NGC 253 (Radovich, Kahanpää, & Lemke 2001).

The warm mass in the ER derived from our OH models is $\sim 10^9 M_{\odot}$, assuming $X(\text{OH})=10^{-6}$ relative to H nuclei and the warm H₂ arising from the same volume as the OH. This estimate of mass may be considered an upper limit. From the H₂ rotational lines

detected by ISO, Sturm et al. (1996) estimated $\sim 3 \times 10^9 M_{\odot}$ of warm gas. Given the uncertain correction by extinction, it is likely that an important fraction of the H_2 emission arises in the ER.

6.2. The halo

The models also indicate the presence of a halo. Despite the uncertainties in the column densities of this component, they are typical of those found toward our galactic nucleus: $N(H_2O, OH) \sim 2 \times 10^{16} \text{ cm}^{-2}$ have been also derived in the diffuse medium toward Sgr B2 (Cernicharo et al. 1997; Neufeld et al. 2003; Goicoechea & Cernicharo 2002), and the derived $N(CH) \approx 2 \times 10^{15} \text{ cm}^{-2}$ is also similar to that found toward Sgr B2 by GRC04 and Stacey et al. (1987). The column densities in the halo derived for NH and NH_3 are uncertain because they are based on single lines, but they could also exist in a population of molecular clouds located far away from the nuclear region. **Assuming $X(H_2O) = 10^{-6} \text{ cm}^{-2}$ (Neufeld et al. 2003) in the halo, $N(H_2) \sim 2 \times 10^{22} \text{ cm}^{-2}$ is obtained and the associated continuum opacity is $\tau_{200\mu m} \sim 8 \times 10^{-3}$. If we further assume an spectral index $\beta = 2$, the derived dust opacity at $25 \mu m$ is ~ 0.5 , comparable to the value of 1.2 in scenario S_2 (section 4). Therefore, significant absorption of the nuclear continuum emission is attributable to the halo.**

6.3. The nuclei

The similarity of the OH column densities in the ER and the nucleus may suggest that, at least to some extent, we are observing the same widespread OH component, and that OH is more excited toward the nucleus because of the underlying stronger infrared continuum in that direction. On this ground a PDR origin of the observed OH would be favoured. However, the inferred high H_2O column density would be difficult to explain in this context. Although H_2O is expected to form efficiently in UV-shielded regions of dense PDRs (Sternberg & Dalgarno 1995), with total column densities similar to those of OH, there seems to be no clear correlation between $N(OH)$ and $N(H_2O)$. In fact, the H_2O column density in the ER is significantly lower than that of OH. Also, detection of NH_3 and, above all, of NH, seem to indicate an additional nuclear component.

OH could also arise in C-shocks (Watson et al. 1985), but it is unlikely that they dominate the OH absorptions because $N(H_2O)$ would then be at least one order of magnitude higher than $N(OH)$. However, an interesting possibility is that those C-shocks, or alterna-

tively hot core regions, are combined with PDRs, i.e., H₂O produced there is subject to a strong UV field and thus to photodissociation. This process may be enhanced if there is hot gas emitting X-rays, like in supernova remnants where the OH abundance is expected to be $\geq 10^{-6}$ (Wardle 1999), or from a nuclear AGN. In the nuclei of Arp 220, several compact 18 cm continuum sources indicate the presence of high luminous supernovae (Smith et al. 1998); however, the extended and external OH required to explain the infrared data suggests a more widespread component. The diffuse OH megamaser emission found in Arp 220 should be related to it (Lonsdale et al. 1998). Soft-extended and hard-compact X-ray emission, detected around and from the nuclei (Clements et al. 2002), could be responsible for photodissociation of H₂O produced in shocks and hot cores, thus enhancing the OH abundance. In particular, hot cores are expected to exist widely in the nuclei, given the high dust temperatures and densities found there. The presence of J-shocks, where $N(\text{OH})$ is expected to be higher than $N(\text{H}_2\text{O})$ except for high enough preshock densities (Neufeld & Dalgarno 1989), cannot be disregarded.

The high column densities obtained for NH and NH₃ seem to indicate that standard gas-phase PDR chemistry alone is not able to explain the full molecular data in Arp 220. Sternberg & Dalgarno (1995) predicted for a PDR an NH column density more than two orders of magnitude lower than that of OH, whereas we estimate $N(\text{OH})/N(\text{NH}) \sim 20$ in Arp 220. The enhancement of NH relative to OH may be more than one order of magnitude. In Sgr B2, GRC04 also found a somewhat high $N(\text{NH})$ relative to OH, i.e. $N(\text{OH})/N(\text{NH}) \sim 30-100$. It is interesting that the high NH abundance in diffuse clouds is a factor of ~ 40 higher than predicted by gas-phase chemical models (Meyer & Roth 1991). The latter has been used by Wagenblast et al. (1993) and Crawford & Williams (1997) to argue for grain-surface production of NH. In principle, this process could also help to enhance the NH abundance in Arp 220, because the dust in the nuclei has been found to be warm so that grain mantles could efficiently evaporate, and also because in an environment with enhanced cosmic rays, as expected from a starburst and the consequent high rates of supernovae, or an AGN, the release of grain mantles to the gas phase by means of sputtering should be also enhanced. However, hydrogenation of NH should in principle continue until saturation, because indeed we observe NH₃ with a column density twice of NH. The issue that now arises is that, if hydrogenation generally completes, then a very low NH-to-NH₃ abundance ratio would be expected, and if it does not complete like in the models of Wagenblast et al. (1993), the scenario fails because of the low relative abundance found for NH₂. In Sgr B2, for example, $\text{NH}:\text{NH}_2:\text{NH}_3=1:10:100$ (GRC04), and NH₂ is found to be fairly abundant (van Dishoeck et al. 1993).

One possible solution for the low NH₂ abundance is that the already invoked enhancement of cosmic rays deeply affects the ion-molecule gas-phase chemistry. Federman, Weber,

& Lambert (1996) have shown that the high NH abundance found in some diffuse galactic environments could be explained through cosmic ray ionization of atomic nitrogen, followed by hydrogen abstraction reactions that form NH_n^+ and dissociative recombination that yields NH. The slight endothermicity of $\text{N}^+ + \text{H}_2 \rightarrow \text{NH}^+ + \text{H}$ (Millar, Farquhar, & Willacy 1997) is not a problem here, given the high dust temperatures in the nuclei. If in Arp 220 the cosmic-ray ionization of N is enhanced, the above scheme could give rise to high NH abundances. Furthermore, both NH_2 and NH_3 would be much less abundant if photodissociation is important in those regions. NH_3 would be formed primarily in grain mantles through nearly complete hydrogenation, thus again keeping the NH_2 abundance low, and released to the gas phase in widespread hot core regions relatively shielded from UV fields. H_2O could also follow this last process.

A chemistry deeply influenced by ion-neutral reactions have been also invoked by Aalto et al. (2002) to explain the high emission from HNC relative to HCN in Arp 220 and other luminous infrared galaxies. Furthermore, Aalto et al. (2002) also found strong subthermal CN emission, indicative of gas at moderate densities and irradiated by UV fields (Rodríguez-Franco, Martín-Pintado, & Fuente 1998). In the **simplest** scenario, the molecular content of Arp 220 may thus be interpreted in terms of hot cores submitted to strong UV and X-ray fields, where enhanced evaporation of grain mantles and ion-molecule chemistry induced by cosmic ray ionization are also deeply affecting the relative molecular abundances.

7. Summary

We have analyzed the ISO/LWS spectrum of Arp 220 using radiative transfer models applied to both the continuum and line emission. Our main results are:

1. The continuum emission from 25 to 1300 μm is well reproduced with a two-component model: (a) the nuclei, with effective size of $0''.4$ and dust temperature of 106 K, which accounts for essentially the whole flux at 25 μm and at millimeter and submillimeter wavelengths, and (b) an extended region (ER), whose effective size is $2''$ and which dominates the continuum emission from 60 to 250 μm .
2. The extinction toward the nuclei is very high ($A_V \sim 10^4$ mag); the dust in the ER is heated through absorption of radiation emanating from the nuclei.
3. The spectrum of Arp 220 shows molecular lines of OH, H_2O , CH, NH, and NH_3 , as well as the atomic [O I] 63 μm line in absorption and the [C II] 158 μm line in emission. The outermost regions of the nuclei, along with the ER, are traced by the lines observed in the far-infrared.
4. The high excitation lines of OH and H_2O are pumped through absorption of photons

emitted by dust. Column densities of $N(\text{OH}) = 2 - 6 \times 10^{17} \text{ cm}^{-2}$ and $N(\text{H}_2\text{O}) = 2 - 10 \times 10^{17} \text{ cm}^{-2}$ are derived toward the nuclei. In the ER, $N(\text{OH}) \sim 2 \times 10^{17} \text{ cm}^{-2}$ and $N(\text{H}_2\text{O}) \sim 3 \times 10^{16} \text{ cm}^{-2}$. We found it necessary to invoke a third component, or halo, to match the low-lying lines of OH and H₂O; this halo has column densities that are similar to those found toward the Galactic Center ($N(\text{OH}, \text{H}_2\text{O}) \sim 1.5 \times 10^{16} \text{ cm}^{-2}$).

5. The CH line detected in the far-infrared spectrum of Arp 220 is assumed to arise from the halo, and the inferred column density is $N(\text{CH}) \sim 2 \times 10^{15} \text{ cm}^{-2}$. This value is also similar to that found toward the Galactic Center.

6. Models for NH and NH₃ indicate high column densities toward the nuclei, $N(\text{NH}) \sim 1.5 \times 10^{16} \text{ cm}^{-2}$ and $N(\text{NH}_3) \sim 3 \times 10^{16} \text{ cm}^{-2}$. The upper limit found for the column density of NH₂ is much lower, $N(\text{NH}_2) \leq 2 \times 10^{15} \text{ cm}^{-2}$.

7. The [C II] 158 μm line strength is approximately reproduced by assuming that C⁺ is 100 times more abundant than OH. Our models predict that the line arises mainly from the ER, and that non-PDR far-infrared emission, with possible extinction effects, is mostly responsible for the observed [C II] deficit in Arp 220. The [O I] 63 μm line is also matched with an abundance of 250 relative to OH and absorption toward the nuclei, the ER, and the halo.

8. PDR molecular chemistry plays a key role in the ER and contributes to the elevated OH abundance at the expense of H₂O. Toward the nuclei, however, important contributions from hot cores, and possibly from shocks, is most plausible. The nitrogen chemistry, and in particular the high NH abundance, seems to be strongly influenced by ion-neutral reactions triggered by cosmic ray ionization.

We are grateful to J.R. Goicoechea for providing the ISO/LWS spectrum of Sgr B2 and for fruitful discussions. E. G-A thanks Spanish SEEU for funding support under project PR2003-0057, and the Harvard-Smithsonian Center for Astrophysics for its hospitality. This work has been partially supported by NASA Grant NAG5-10659, the NASA LTSA program and the Office of Naval Research.

REFERENCES

- Aalto, S., Polatidis, A.G., Hüttemeister, S., & Curran S.J. 2002, A&A, 381, 783
- Anantharamaiah, K.R., Viallefond, F., Mohan, N.R., Goss, W.M., & Zhao, J.H. 2000, ApJ, 537, 613
- Baluteau, J.-P. et al. 1997, A&A, 322, L33

- Brown, J.M., & Evenson, K.M. 1983, ApJ, 268, L51
- Carico, D.P., Keen, J., Soifer, B.T., & Neugebauer, G. 1992, PASP, 104, 1086
- Ceccarelli, C., et al. 2002, A&A, 383, 603
- Cernicharo, J., et al. 1997, A&A, 323, L25
- Cernicharo, J., Pardo, J.R., González-Alfonso, E., Serabyn, E., Phillips, T.G., Benford, D.J., Mehringer, D. 1999, ApJ, 520, L131
- Cernicharo J., Goicoechea J.R., & Caux, E. 2000, ApJ, 534, L199
- Clegg, P.E., et al. 1996, A&A, 315, L38
- Clements, D.L., McDowell, J.C., Shaked, S., Baker, A.C., Borne, K., Colina, L., Lamb, S.A., & Mundell, C. 2002, ApJ, 581, 974
- Crawford, I.A., & Williams, D.A. 1997, MNRAS, 291, L53
- Downes, D., & Solomon, P.M. 1998, ApJ, 507, 615
- Eales, S.A., Wynn-Williams, C.G., & Duncan, W.D. 1989, ApJ, 339, 859
- Eckart, A., & Downes, D. 2001, ApJ, 551, 730
- Federman, S.R., Weber, J., & Lambert, D., 1996, ApJ, 463, 181
- Fischer, J., et al. 1997, in "The first ISO workshop on analytical spectroscopy", eds. Heras, A., Leech, K., Trams, N., & Perry, M., Noordwijk: ESA Publication SP-419, p. 149
- Fischer, J., et al. 1999, Ap&SS, 266, 91
- Genzel, R., Watson, D.M., Crawford, M.K., & Townes, C.H. 1985, ApJ, 297, 766
- Genzel, R., et al. 1998, ApJ, 498, 579
- Goicoechea, J.R., & Cernicharo, J., 2002, ApJ, 576, L77
- Goicoechea, J.R., Rodríguez-Fernández, N.J., & Cernicharo, J. 2004, ApJ, 600, 214 (GRC04)
- González-Alfonso, E., & Cernicharo, J. 1997, A&A, 322, 938
- González-Alfonso, E., & Cernicharo, J. 1999, ApJ, 525, 845

- Graham, J.R., Carico, D.P., Matthews, K., Neugebauer, G., Soifer, B.T., & Wilson, T.D. 1990, *ApJ*, 354, L5
- Green, S., Maluendes, S., & McLean, A. D. 1993, *ApJS*, 85, 181
- Haas, M., Klaas, U., Müller, S.A.H., Chini, R., & Coulson, I. 2001, *A&A*, 367, L9
- Henkel, C., & Mauersberger, R. 1993, *A&A*, 274, 730
- Hildebrand, R.H. 1983, *QJRAS*, 24, 267
- Kaufman, M.J., Wolfire, M.G., Hollenbach, D.J., & Luhman, M.L. 1999, *ApJ*, 527, 795
- Kessler, M.F., et al. 1996, *A&A*, 315, L27
- Launay, J.-M., & Roueff, E. 1977, *J. Phys. B*, 10, 879
- Launay, J.-M., & Roueff, E. 1977, *A&A*, 56, 289
- Lonsdale, C.J., Diamond, P.J., Smith, H.E., & Lonsdale, C.J. 1998, *ApJ*, 493, L13
- Luhman, M.L., et al. 1998, *ApJ*, 504, L11
- Luhman, M.L., Satyapal, S., Fischer, J., Wolfire, M.G., Sturm, E., Dudley, C.C., Lutz, D., & Genzel, R. 2003, *ApJ*, 594, 758
- Malhotra, S., et al. 2001, *ApJ*, 561, 766
- Meyer, D.M., & Roth, K.C. 1991, *ApJ*, 376, L49
- Millar, T.J., Farquhar, P.R.A., & Willacy, K. 1997, *A&AS*, 121, 139
- Neufeld, D.A., & Dalgarno, A. 1989, *ApJ*, 340, 869
- Neufeld, D.A., Bergin, E.A., Melnick, G.J., & Goldsmith, P.F. 2003, *ApJ*, 590, 882
- Offer, A.R., van Hemert, M.C., & van Dishoeck, E.F. 1994, *J. Chem. Phys.*, 100, 362
- Okumura, S.K., Kawabe, R., Ishiguro, M., Ishizuki, S. 1994, in "Astronomy with Millimeter and Submillimeter Wave Interferometry", IAU Colloquium 140, ASP Conference Series, Eds. M. Ishiguro and J. Welch, 59, 376
- Radford, S.J.E., Solomon, P.M., & Downes, D. 1991, *ApJ*, 368, L15
- Radford, S.J.E., et al. 1991, in "Dynamics of Galaxies and Their Molecular Cloud Distributions", eds. F. Combes & F. Casoli, IAU, Netherlands

- Radovich, M., Kahanpää, J., & Lemke, D. 2001, *A&A*, 377, 73
- Rigopoulou, D., Lawrence, A., & Rowan-Robinson, M. 1996, *MNRAS*, 278, 1049
- Rodríguez-Franco, A., Martín-Pintado, J., & Fuente, A. 1998, *A&A*, 329, 1097
- Sakamoto, K., Scoville, N.Z., Yun, M.S., Crosas, M., Genzel, R., & Tacconi, L.J. 1999, *ApJ*, 514, 68
- Savage, B.D., & Sembach, K.R. 1996, *ARA&A*, 34, 279
- Scoville, N.Z., Sargent, A.I., Sanders, D.B., Soifer, B.T. 1991, *ApJ*, 366, L5
- Scoville, N.Z., Yun, M.S., & Bryant, P.M. 1997, *ApJ*, 484, 702 (SYB97)
- Skinner, C.J., Smith, H.A., Sturm, E., Barlow, M.J., Cohen, R.J., Stacey, G.J. 1997, *Nature*, 386, 472
- Smith, H.E., Lonsdale, C.J., Lonsdale, C.J., & Diamond, P.J. 1998, *ApJ*, 493, L17
- Soifer, B.T., Neugebauer, G., Matthews, K., Becklin, E.E., Ressler, M., Werner, M.W., Weinberger, A.J., & Egami, E. 1999, *ApJ*, 513, 207 (S99)
- Soifer, B.T., Neugebauer, G., Matthews, K., Egami, E., & Weinberger, A.J. 2002, *A.J.*, 124, 2980
- Solomon, P.M., Radford, S.J.E., & Downes, D. 1990, *ApJ*, 348, L53
- Solomon, P.M., Downes, D., & Radford, S.J.E. 1992, *ApJ*, 387, L55
- Spoon, H.W.W., Moorwood, A.F.M., Lutz, D., Tielens, A.G.G.M., Siebenmorgen, R., & Keane, J.V., 2004, *A&A*, 414, 873
- Stacey, G.J., Lugten, J.B., & Genzel, R. 1987, *ApJ*, 313, 859
- Stacey, G.J., Geis, N., Genzel, R., Lugten, J.B., Poglitsch, A., Sternberg, A., & Townes, C.H. 1991, *ApJ*, 373, 423
- Sternberg, A., & Dalgarno, A., 1995, *ApJS*, 99, 565
- Sturm, E., et al. 1996, *A&A*, 315, L133
- Tielens, A.G.G.M., & Hollenbach, D., *ApJ*, 291, 722
- van Dishoeck, E.F., Jansen, D.J., Schilke, P., & Phillips, T.G., 1993, *ApJ*, 416, L83

Vastel, C., Polehampton, E.T., Baluteau, J.-P., Swinyard, B.M., Caux, E., & Cox, P. 2002, ApJ, 581, 315

Wagenblast, R., Williams, D.A., Millar, T.J., & Nejad, L.A.M. 1993, MNRAS, 260, 420

Wardle, M. 1999, ApJ, 525, L101

Watson, D.M., Genzel, R., Townes, C.H., & Storey, J.W.V. 1985, ApJ, 298, 316

Wolfire, M.G., Tielens, A.G.G.M., & Hollenbach, D. 1991, ApJ, 358, 116

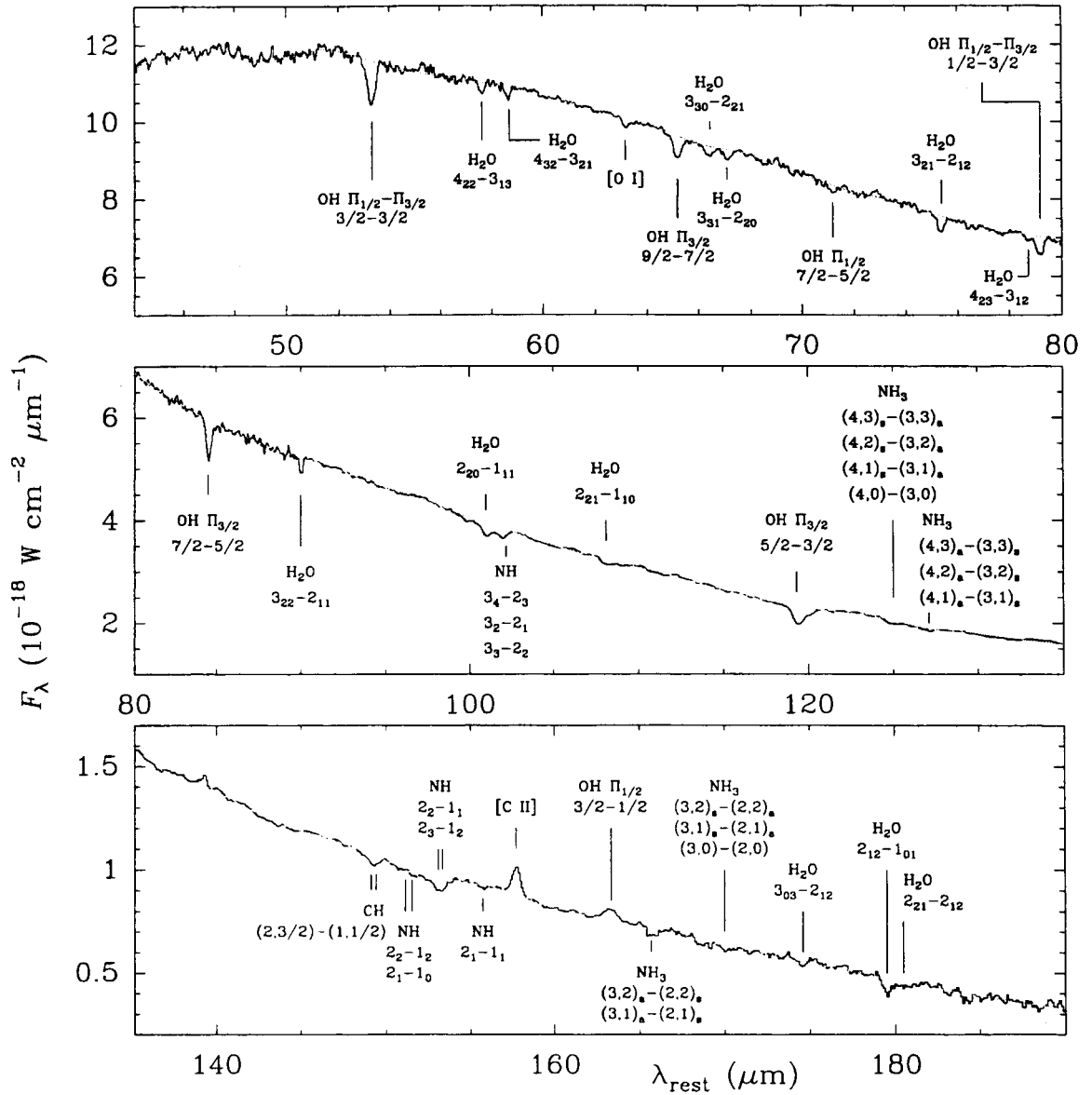


Fig. 1.— ISO/LWS spectrum of Arp 220, where the most prominent line features are identified (see text). The grey line shows the adopted baseline (continuum level). **Wavelengths in this and next figures are rest wavelengths.**

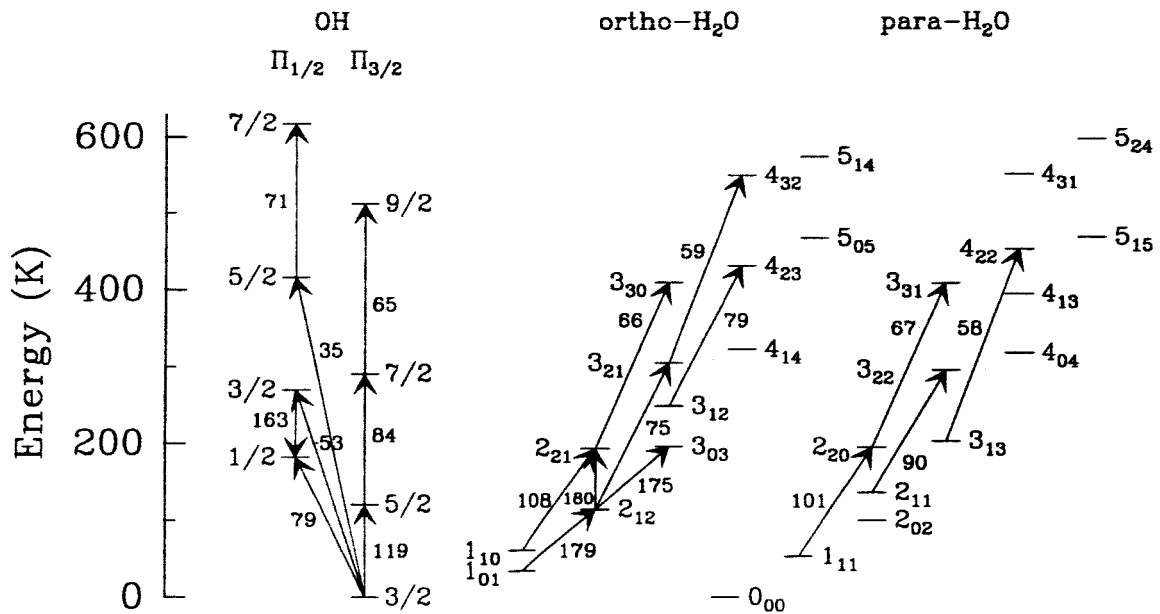


Fig. 2.— Energy level diagrams of OH and H₂O (ortho and para). Rotational levels with energies above the ground state up to 620 K are shown; the lines detected in Arp 220 are indicated with arrows and their wavelengths are in μm . OH Λ -doubling is ignored because the Λ -doublets are not resolved with the ISO grating resolution.

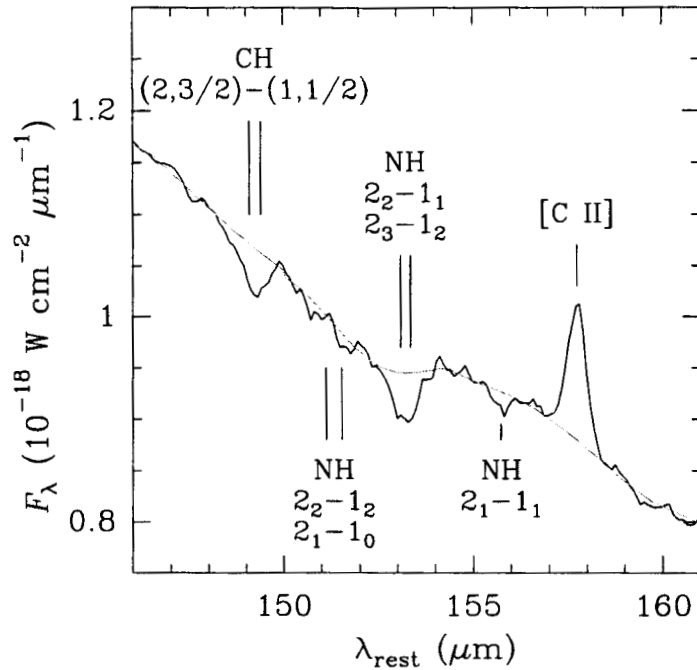


Fig. 3.— Line assignments in the vicinity of the 153.2 μm feature. The grey line shows the adopted continuum level.

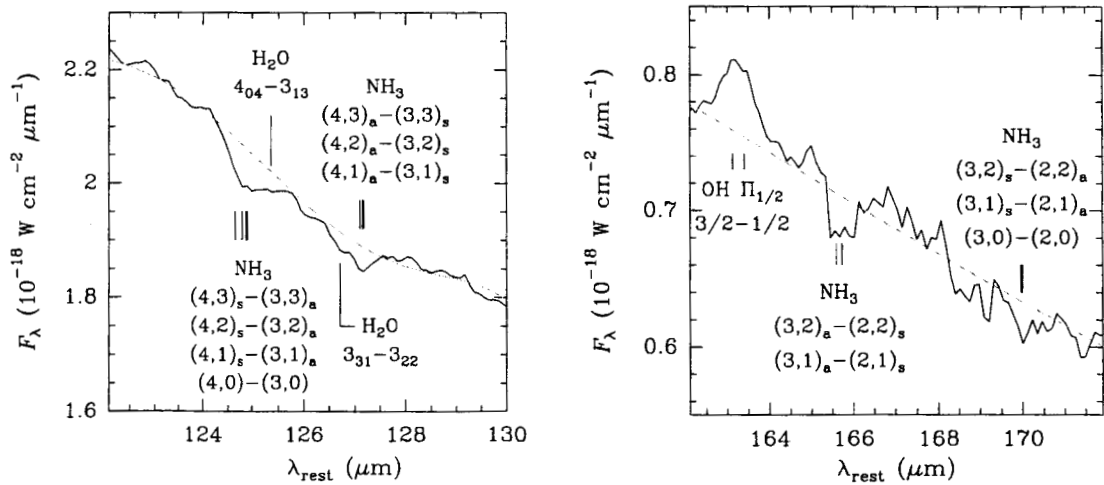


Fig. 4.— NH_3 lines around 125, 127, 166, and 170 μm . The grey line shows the adopted continuum level. The 125 and 127 μm features could be partially contaminated by the labelled H_2O lines.

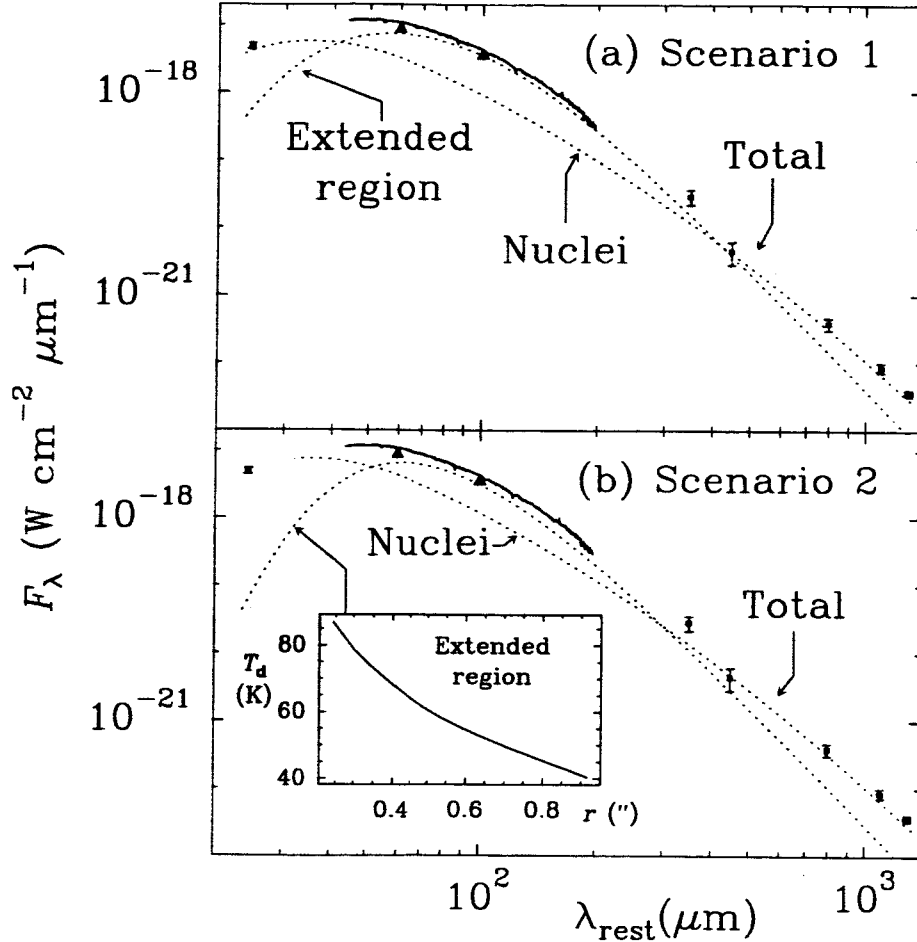


Fig. 5.— Fits of the continuum emission from Arp 220 in the 25-1300 μm range for scenarios (a) S_1 and (b) S_2 . Solid line shows ISO-LWS spectrum of Arp 220, and filled triangles show the 60 and 100 μm IRAS fluxes for comparison. Filled squares show the fluxes measured by Soifer et al. (1999, 24.5 μm); Eales, Wynn-Williams, & Duncan (1989, 450 μm); Rigopoulou, Lawrence, & Rowan-Robinson (1996, 350, 800, and 1100 μm); and Sakamoto et al. (1999, 1300 μm). Dotted lines indicate the computed contributions from the nuclei and the ER, whereas the solid grey line show the expected total flux. The insert panel shows the calculated dust temperatures in function of the radial angular distance for S_2 (see text).

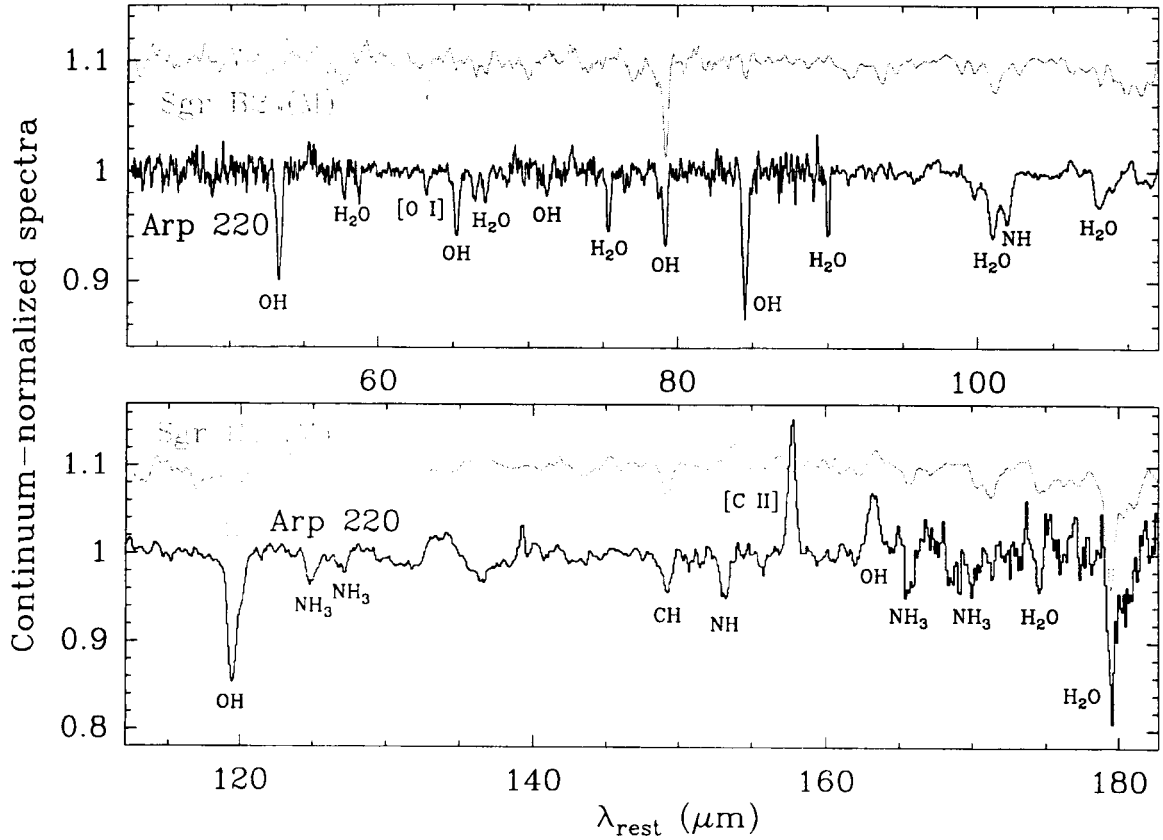


Fig. 6.— Continuum-normalized spectra of Sgr B2 (M) and Arp 220. The main carriers of some line features are indicated.

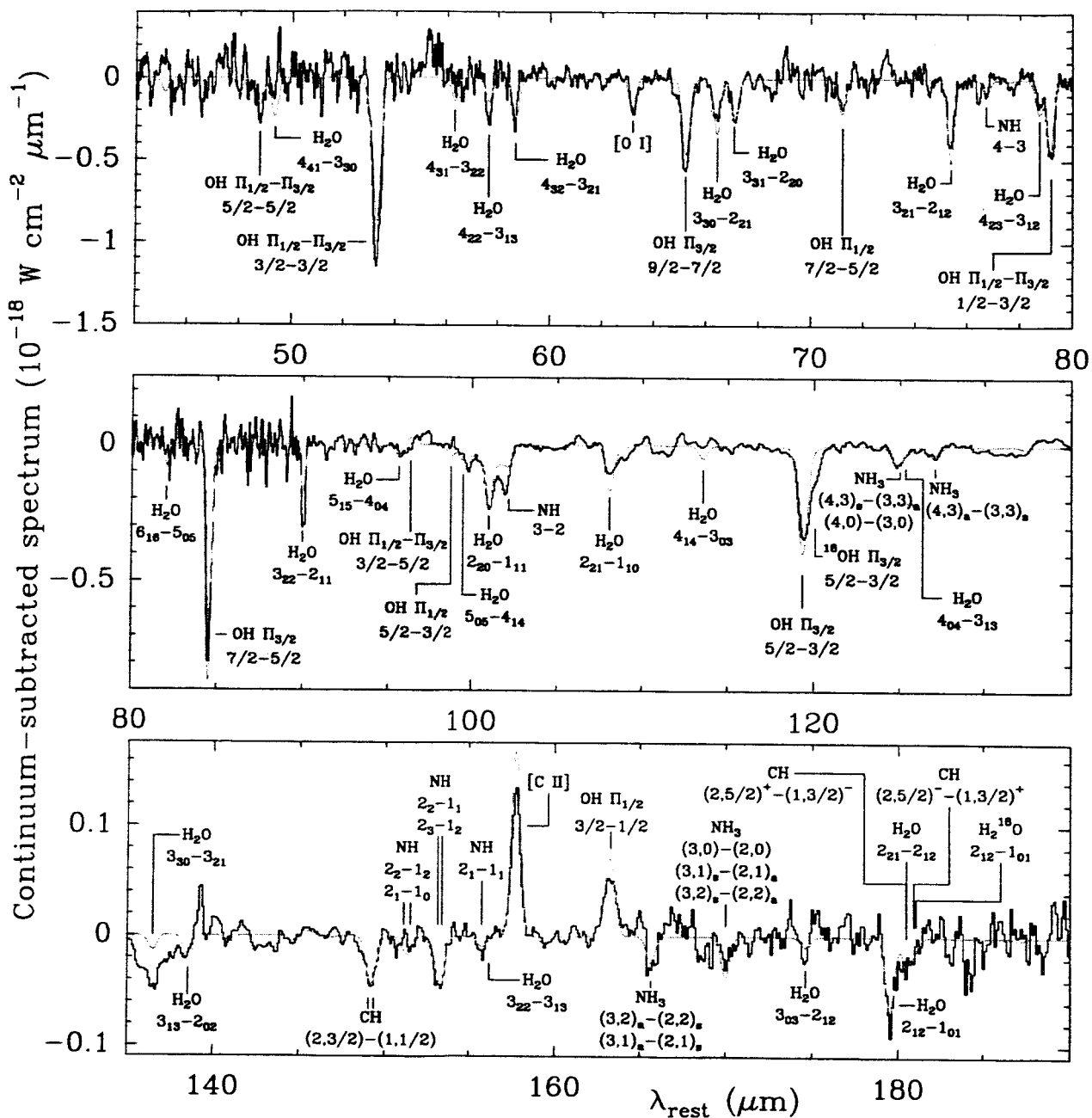


Fig. 7.— Continuum-subtracted spectrum of Arp 220, compared with the result of the model (in grey). The line features that contribute more to the model are identified (see text).

Table 1. Physical parameters derived from the continuum emission

Scenario	Component	τ_{abs} (24.5 μm)	d (pc)	β	T_d (K)	λ_t (μm)	M_d (M_\odot)	$< n(\text{H}_2) >^a$ (cm^{-3})	L (L_\odot)
S ₁	Nucleus	0	145	1.5	85	640	5.1×10^7	6.5×10^4	4.8×10^{11}
S ₁	ER	0	630	2.0	85	770	1.3×10^8	1.6×10^5	4.8×10^{11}
S ₂	Nucleus	1.2	145	1.5	106	520	3.6×10^7	4.6×10^4	9.8×10^{11}
S ₂	ER	0	660	2.0	106	650	9.3×10^7	1.2×10^5	9.8×10^{11}
				2.0	40-90 ^b	82	3.9×10^7	5.3×10^2	—

^a Assuming a single source instead of an ensemble of clouds

^b The temperature is calculated throughout the ER from the balance between heating and cooling with the nucleus as the primary heating source

Table 2. Column densities **derived** toward Arp 220^a

Species	Nucleus	ER	Halo
OH	2.0×10^{17}	2.0×10^{17}	1.8×10^{16}
H ₂ O	2.0×10^{17}	3.0×10^{16}	1.5×10^{16}
CH	-	-	2.0×10^{15}
NH	1.3×10^{16}	-	1.8×10^{15}
NH ₃	2.8×10^{16}	-	4.0×10^{15}
C ⁺	2.0×10^{19}	2.0×10^{19}	-
O	5.0×10^{19}	5.0×10^{19}	2.7×10^{18}

^aUnits are cm⁻²